THESIS FOR THE DEGREE OF LICENTIATE OF ENGINEERING

Electric machine control for energy efficient electric drive systems

ANDREAS ANDERSSON

Department of Energy and Environment
Division of Electric Power Engineering
CHALMERS UNIVERSITY OF TECHNOLOGY
Göteborg, Sweden 2015

Electric machine control for energy efficient electric drive systems
ANDREAS ANDERSSON

Licentiante Thesis at the Graduate School in Energy and Environment

Department of Energy and Environment
Division of Electric Power Engineering
Chalmers University of Technology
SE–412 96 Göteborg
Sweden
Telephone +46 (0)31–772 1000

Chalmers Bibliotek, Reproservice
Göteborg, Sweden 2015

Electric machine control for energy efficiency electric drive systems
ANDREAS ANDERSSON
Department of Energy and Environment
Chalmers University of Technology

Abstract

Pure electric vehicles and hybrid electric vehicles are of increasing interest in the automotive industry, much due to challenges such as emission level legislations and the environmental impact of the transportation sector. When continuously striving for better performing and more energy efficient electric powertrains, with high drivability and redundancy, there is an ever increasing need for further research and development in the areas of controls, design and system level optimization.

Over the past decade, noise and vibrations from electric drives has increasingly become an area of attention for both academia and industry. The absence of the broad band noise from the internal combustion engine brings new noise, vibration and harshness (NVH) challenges for electric propulsion applications. Magnetic noise from electrical machines is of particular interest in automotive applications. It is not only related to the physical design and mounting of the electrical machine but also to the choice of control approach and voltage modulation strategy.

This thesis is focused on energy efficiency enhancements in the electric drive system, primarily on the control of the three phase inverter. In addition to the energy efficiency perspective, also the appearance of electromagnetic forces and NVH-perspectives are considered. Alternative modulation techniques are investigated, where the so called discontinuous pulse width modulation is is proven to decrease the inverter losses, substantially.

The appearance of electromagnetic forces is investigated extensively, with focus on radial forces acting as attractive or repulsive forces between the rotor and the stator. Its influence on stator deformations, and consequently noise and vibrations, is investigated where also influence of machine design, modulation techniques and perceived annoyance of the radiated sound are included.

The scientific contribution can be summarized with two parts. Firstly, the interdisciplinary research where energy efficiency enhancements are coupled to NVH-performance. Secondly, the cause and effect of electromagnetic forces as the link between machine design, controls and NVH-perspectives.

It is proven that when using discontinuous PWM (DPWM) instead of synchronous

PWM (SPWM), the inverter losses can be decreased with up to -17 percent. While complementing the modulation with randomization of the switching frequency the increase in perceived annoyance, due to increased radiated noise when using DPWM, is significantly decreased. At rotational speeds above base speed, no difference in perceived annoyance between DPWM and SPWM could statistically be ensured when randomization is used. At a randomization level with a variance of $\sigma = 1000$ Hz the noise is comparable with the magnitude of the harmonics themselves, hence further randomization in terms of increased variance is without any gain.

Index Terms: Energy efficiency, modulation techniques, noise assessment, permanent magnet synchronous machine (PMSM).

Acknowledgements

First and foremost I would like to thank Professor Torbjörn Thiringer, my academic supervisor and examiner, for his continuous and consistent support during the work. I would also like to thank Dr. Stefan Lundberg, my academic co-supervisor, for his time and contributions, especially with the extensive support with the experimental work. A special thanks goes to Dr. Jonn Lantz at Volvo Car Group, my industrial supervisor, for his time and support as well as the industrial contributions. The work is founded by Volvo Car Group and the Swedish Energy Agency, both are gratefully acknowledged for the financial support.

Many people, both at Volvo Cars and at Chalmers, have been involved to varying degrees and by their support, knowledge and helpfulness influenced the work. I would like to thank them all, especially my colleagues at the Division of Electric Power Engineering at Chalmers and the Department of Electric Propulsion Systems at Volvo Cars.

Andreas Andersson
Göteborg, Sweden
Autumn, 2015

Contents

Chapter 1

Introduction

1.1 Problem background

Seemingly, electric propulsion is an area of focus for both academia and industry. Striving for better performing and more energy efficient electric powertrains, with high drivability and redundancy, there is an ever increasing need for research and development within the fields of controls, design and system level optimization. In the application of electrified vehicles, it is of most importance to maintain high energy efficiency by electrical losses minimization. Out of many advantages, loss minimization is beneficial from cooling, driving range and life cycle perspectives. Unsurprisingly, enhancements within one field seldom comes without drawbacks in another.

Over the past decade, noise and vibrations from electric drives has increasingly become an area of attention as well. The absence of the broad band noise from the internal combustion engine brings new noise, vibration and harshness (NVH) challenges for electric and electric hybrid vehicle applications. Electromagnetic noise is in literature pointed out as one of the main contributors to the noise in vehicles, usually perceived as very annoying due to its tonal appearance [1]. Electromagnetic noise is of particular interest in the automotive industry, its appearance is not only related to the physical design of the machine but also to the selection of control approach and voltage modulation, which is further elaborated and investigated in this work.

High frequency noise in permanent magnet machines (PMSM), originating from the inverter switching, has previously been researched. Some interesting works are presented in [2, 3, 4, 5, 6]. Different modulation techniques and switching frequency randomization are frequently researched areas as well. Although, usually evaluated from an electrical perspective [7, 8, 9, 10, 11]. In [7] and [8], focusing on harmonic spreading

and efficiency, different random PWM techniques are investigated, concluding a significant decrease in harmonic intensity and advocates benefits from an EMI perspective. Most often harmonic spread of inverter output current, power spectral density and energy efficiency are considered, while noise emissions often are disregarded. Additionally, application-based or interdisciplinary evaluations are seldom seen. In summary, missing in literature is more comprehensive analyses where additional adverse effects are incorporated, such as energy efficiency enhancements' influence on NVH. Moreover, understanding the cause of effect when it comes to NVH-related issues, force densities and electromagnetic behaviour is needed to completely understand the interlinked phenomena, which is a major part of this work.

1.2 Purpose of the thesis and contributions

The purpose of the work presented in this thesis is to enhance the research on the topic of electric machines, energy efficiency enhancements and NVH. Energy saving measures have been previously researched, both in the context of energy efficiency improvements for inverters as well as for electrical machines. However, as previously discussed, missing in literature are comprehensive analyses and investigations of adverse effects and relations which usually are of an interdisciplinary nature, such as inverter switching influence on vibrations and radiated sound. Summing up, the main contributions can be itemized as

- Methods for inverter energy efficiency enhancements are investigated. Primarily, different modulation techniques are investigated from an energy efficiency perspective with the purpose to quantify benefits and potential adverse effects.
- Analytical expressions for the spatial and temporal content of the airgap flux density and force density are derived and verified with finite element analysis (FEA). The purpose of this is to increase the understanding and the knowledge of how electromagnetic forces arise. Moreover, the knowledge is essential to grasp the impact of machine control and voltage modulation on generation of electromagnetic forces and NVH-issues related to electromagnetic noise.
- Energy efficiency enhancements are evaluated both from an energy efficiency perspective and from an NVH-perspective. Acoustic listening tests are used to evaluate how the acoustic noise from different solutions are perceived, with the purpose of quantifying differences and statistically ensure the findings validity.
- FEA and experimental testing have been conducted with the purposes of verifying theory, studying phenomena that are either too complex and too uncertain to inves-

tigate numerically and to increase the scientific value of the findings. Additionally, the experimental testing fulfills an educational purpose.

1.3 Thesis outline

Chapter 2 covers essential theory of electric drive system modelling. Modelling of the PMSM is covered and necessary analytical expressions are presented. The maximum torque per ampere technique is discussed as well as different modulation techniques such as the discontinuous PWM. Chapter 3 is assigned to electromagnetic forces in the machine. Spatial and temporal content of both airgap flux density and force density are explained and analytically expressed. Necessary theory to incorporate electromagnetic quantities with NVH-related issues is discussed.

In Chapter 4 the basis for the experimental testing is presented. The methodology used is presented along with technical descriptions of the equipment used. Chapter 5 covers the finite element modelling, which parts of the findings are based upon. The first part of the chapter presents the 2D model of the electrical machine, the second part of the chapter describes the methodology used to perform voltage excited FEM-simulations with a switched voltage source. The last part covers the use of multi-physics simulations where electromagnetic forces are coupled with mechanical models to study its impact of noise and vibrations.

Chapter 6 is a continuation on the third chapter and is based on finite element modelling. The influence of stator slots and inverter switching is investigated focusing on low vibrational orders. Primarily, the influence of stator slots and its influence on NVH-issues are discussed. In Chapter 7, different modulation techniques are investigated, primarily from an energy efficiency perspective. Lastly, in Chapter 8, the perceived annoyance for different modulation techniques is investigated. Listening tests are presented completing the chain from energy efficiency enhancements to perceived acoustic sensation for persons subjected to the emitted noise from the machine.

1.4 Publications

The following list of publications have been made during the course of the project. The publications are to a large extent reflected in the work presented in this thesis.

- Andersson, A. Thiringer, T. *An analysis of inverter switching loss minimization based on discontinuous PWM for a salient-pole PMSM*, Conference: 16^{th} European Power Electronics Conference, Lappeenranta 2014.

- Andersson, A. Thiringer, T. *Inverter losses minimization using variable switching frequency based on multi-objective optimization*, Conference: XX^{th} International Conference on Electrical Machines, Berlin 2014.
- Andersson, A. Lennström, D. Nykänen, A. *Influence of inverter modulation strategy on electric drive efficiency and perceived sound quality*, Journal: IEEE Transactions On Transportation Electrification, 2015 (in review, 2^{nd} round).

Chapter 2

Electric drive system

The selection of machine topology in electric and hybrid electric propulsion systems for automotive use is to a large extent unambiguous, the PMSM is very often used. Walker et al. [12] presents a comprehensive topology selection investigation of electrical machines based on requirements from the US Department of Energy *FreedomCar 2020* targets. *FreedomCar* targets for hybrid propulsion machines by the year 2020 includes, but are not limited, to performance indices such as rated and peak power, maximum rotational speed, minimum peak efficiency, unit weight and cost. The study includes more conventional topologies such as the PMSM, induction machine and the synchronous reluctance machine, but also topologies such as transverse flux machines.

The findings indicate that despite well known issues with the associated cost of permanent magnet (PM) machines and the relatively poor field weakening capabilities, the PMSM is the favourable choice, both for today and in the future. This is primarily due to significant benefits such as high efficiency and high power and torque density. In particularly, the interior PM synchronous machine (IPMSM) is favourable in front of the surface mounted PM machine (SPMSM), findings that are in line with the performance comparison between IPMSM and SPMSM presented by Pellegrino et al. [13]. In the comparison presented by Pellegrino et al. [13], the relatively poor overload capabilities and field weakening capabilities are drawbacks that are highlighted for the SPMSM.

Clearly, there is a wide range of machine topologies suitable for hybrid/electric propulsion. The IPMSM topology selected in this work is a reasonable choice for hybrid/electric vehicles. The work presented in this thesis is based upon a IPMSM currently in production, used in a mass produced hybrid vehicle. The same machine is used both in numerical simulations as well as the experimental testing.

In this Chapter, the modelling of the electric drive system is described. Modelling of the electrical machine, inverter and a suitable vehicle for electric propulsion is covered

as well as the machine controls and the basics of different modulation techniques.

2.1 Salient-pole PMSM modelling

The machine used in the thesis is, as previously mentioned, an IPMSM. The magnet placement is in a v-shaped configuration with the benefit of generating reluctance torque in addition to the Lorentz torque. The magnet configuration results in different reluctance in the direct and quadrature direction, hence different inductances (L_d and L_q), commonly known as a salient-pole rotor.

2.1.1 Equivalent circuit model

The mathematical model of a salient-pole PMSM in the synchronous reference frame can be presented with the circuit equivalent model shown in Fig. 2.1 where L_d and L_q are the inductances in the direct and quadrature direction, u_d and u_q are the dq-stator voltages, i_d and i_q are the dq-current, R_s is the stator resistance, ω_r is the electrical rotor speed, Ψ_m is the flux linkage originating from the magnets and Ψ_d and Ψ_q are the direct and quadrature flux linkages, respectively [14].

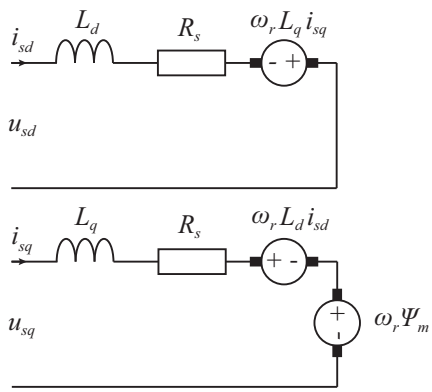

Figure 2.1 Equivalent circuit for the PMSM in the dq-reference frame

The stator equations, representing the relations between stator voltage and phase current can be expressed as

$$L_d \frac{di_d}{dt} = u_d - R_s i_d + \omega_r L_q i_q \tag{2.1}$$

$$L_q \frac{di_q}{dt} = u_q - R_s i_q - \omega_r (L_d i_d + \Psi_m) \tag{2.2}$$

based on the illustration in Fig. 2.1. The relation between flux linkage, inductance and current are expressed as

$$\Psi_d = L_d i_d + \Psi_m \tag{2.3}$$

$$\Psi_q = L_q i_q \tag{2.4}$$

$$|\Psi_s| = \sqrt{\Psi_d^2 + \Psi_q^2}. \tag{2.5}$$

The expression for the electromagnetic torque can be written as [14]

$$T_e = \frac{3n_p}{2}\left(\Psi_d i_q - \Psi_q i_d\right) \tag{2.6}$$

where n_p is the number of pole pairs.

In addition to the model previously presented, which includes only fundamental components without any secondary effects such as harmonics in the induced voltage, also variations in L_d, L_q and Ψ_m are considered. The variations are dependent on i_d and i_q and occur due to magnetic saturation in the iron material. Due to cross saturation, L_d is not only affected by i_d and L_q is not only affected by i_q. Since the path in the q-direction is more easily saturated, L_q usually varies more than L_d [15].

2.1.2 PMSM control

In the work presented, the machine is controlled using a field oriented control (FOC) method comprised of a speed controller cascade coupled with an inner current controller. The controllers are derived using the internal model control (IMC) strategy [14] and implemented using the synchronously rotating reference frame (dq-reference frame). For the dq-current, two parallel controllers are used where the d- and the q-component are controlled separately. This is enabled by decoupling the d and q axes from each other by feedforwarding of the coupling terms. These are the parts in the stator equation where i_d influences i_q and vice versa. For enhanced performance, features such as anti-wind up and active damping are implemented.

By feed forwarding the back-emf and the coupling term, the PMSM model stator current relation in the q-direction can be rewritten as

$$L_q \frac{di_q}{dt} = u_q - R_s i_q - \omega_r \left(L_d i_d + \Psi_m\right) + \omega_r \left(\hat{L}_d i_d + \hat{\Psi}_m\right) \tag{2.7}$$

where $\hat{L}_d$ and $\hat{\Psi}_m$ are estimated values of L_d and Ψ_m, respectively. Assuming perfect parameters, i.e. $\hat{L}_d = L_d$ and $\hat{L}_q = L_q$, the following transfer function is obtained

$$G(S) = \frac{u_q(S)}{i_q(S)} = \frac{1}{sL_q + R_s}. \tag{2.8}$$

By defining the closed-loop system for the current controller as a low-pass filter with the bandwidth α_c the closed-loop system is defined as

$$G_{cl}(S) = \frac{F(S)G(S)}{1 + F(S)G(S)} = \frac{\alpha_c}{s + \alpha_c}. \tag{2.9}$$

The q-controller, $F_q(S)$, then becomes

$$F_q(S) = K_{pc} + \frac{K_{ic}}{s} = \frac{\alpha_c}{s} G(S)^{-1} = \alpha_c L_q + \frac{\alpha_c R_s}{s}. \tag{2.10}$$

The same procedure is used to derive the parameters for the d-current controller and the speed controller. In Fig. 2.2 the control system is illustrated. As can be seen, it is a closed loop system where the phase current and the rotor position are measured. The rotational speed of the machine is estimated using an estimator based on the phase lock loop (PLL) principle.

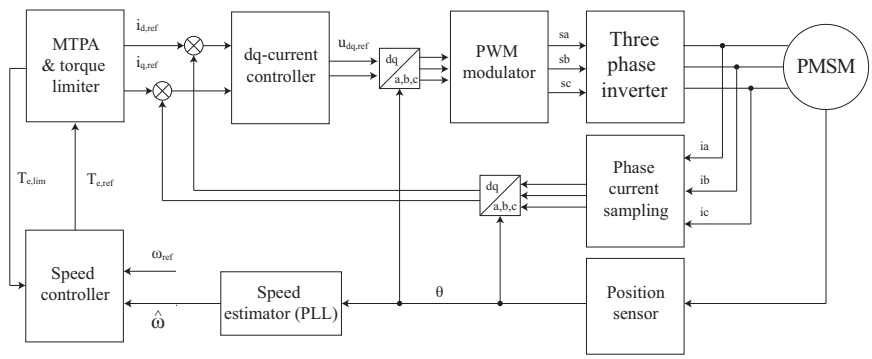

Figure 2.2 Illustration of the PMSM control system

2.1.3 Maximum torque per ampere with variable inductances

In (2.6) the electromagnetic torque equation is presented. As the equation describes, the torque is a function of both i_d and i_q. Consequently, different combinations of these can be used to obtain the same torque. In order to achieve a high energy efficient drive system the maximum torque per ampere (MTPA) approach is used for all simulations and all experimental testing. For a given torque reference, the selection of i_d and i_q references is based on minimization of the RMS current. Variations in L_d, L_q and Ψ_m are considered

as functions of both i_d and i_q, which adds additional complexity. The maximum torque per ampere is obtained by solving the following minimization problem

$$\begin{aligned} \textit{minimize} \quad & f_0(i_d, i_q) \\ s.t. \quad & f_i(i_d, i_q) \leq 0 \\ & h_i(i_d, i_q) = 0 \end{aligned} \tag{2.11}$$

where

$$\begin{aligned} f_0(i_d, i_q) &= \sqrt{i_d^2 + i_q^2} \\ f_i(i_d, i_q) &= \sqrt{u_d(i_d, i_q)^2 + u_q(i_d, i_q)^2} - \frac{V_{dc}}{\sqrt{3}} \\ h(i_d, i_q) &= 1.5 n_p i_q \left[\Psi_m(i_d, i_q) + (L_d(i_d, i_q) - L_q(i_d, i_q))\, i_d\right] - T_{e,ref} \end{aligned} \tag{2.12}$$

where $u_d(i_d, i_q)$ and $u_q(i_d, i_q)$ are calculated using the stator equations in steady state, described in (2.1) and (2.2) for the direct and quadrature axes, respectively. The objective function, f_0, equals the RMS phase current. The inequality constraint, $f_i(i_d, i_q)$, acts as voltage limitation. When this is active, field weakening is required. Lastly, the equality constraint, $h(i_d, i_q)$, defines the electromagnetic torque function which is also found in (2.6). The problem definition implies that for each combination of torque and speed, there is a combination of i_d and i_q that minimizes the phase current RMS value, which aims to minimize the resistive losses in the inverter and the machine. The trajectory obtained by this approach is not the optimum in a global sense, improvements can be made by extending the problem by including, for instance, iron losses in the machine in accordance with the research presented by Meifen et al. [16]. However, the selection of only minimizing the RMS value of the phase current is considered to be a reasonable trade-off between efficiency-enhancing measures and time invested in development of the optimization algorithm. Furthermore, during loading the copper losses is the most significant loss component in the drive system [17], motivating the solution approach proposed here.

The variation in L_d, L_q and Ψ_m adds an additional degree of complexity, since these are not constants in (2.11) and (2.12). Therefore, the solution for all combinations of torque and rotational speeds are calculated offline and further implemented in the control system by the use of look-up tables.

In Fig. 2.3 the electromagnetic torque is presented as function of i_d and i_q. As one can see, the rightmost edge of the colored part, which is indicated with the solid red line, gives maximum torque per ampere under the assumption that the rotational speed is below base speed, $\omega < \omega_b$. If the rotational speed exceeds the base speed, the inequality constraint $f_i(i_d, i_q)$ becomes active. As a consequence, the dq-current reference values

will deviate from the MTPA-line. At such instances, i_q is decreased and i_d is increased in the negative direction in order to maintain the reference torque.

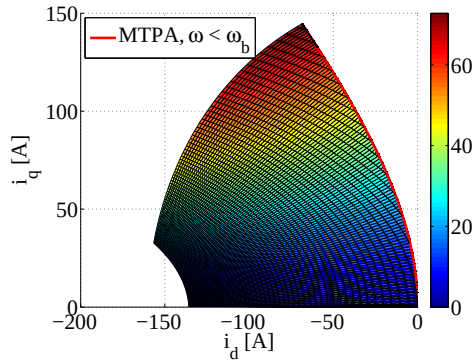

Figure 2.3 Illustration of electromagnetic torque as function of i_d and i_q

2.2 Three-phase voltage source inverter

To allow for variable speed operation, a voltage source inverter can be used to control voltage magnitude and frequency. A typical topology used in industrial applications is the two-level inverter, illustrated in Fig. 2.4. Besides the two-level inverter, there are additional topologies such as variations of multi-level inverters and the neutral point clamped inverter (NPC-inverter). Both have recently been of increasing interest targeting automotive use [18, 19, 20]. Although, it is not evident which inverter topology to favour. The research presented in [18, 19, 20] indicates that multi-level inverters are likely to operate with higher inverter efficiency than a two-level inverter. On the other hand, commonly highlighted drawbacks are the increased number of switches and gate drivers and more complex control and modulation strategies. Additionally, due to the different current harmonic content, losses in for example the battery might increase when using a multi-level inverter instead of a two-level inverter [18, 19].

A two-level inverter topology is used in this work. It is based on six switches arranged in three legs, each with two in series. All six switches, in this case IGBT-modules, are equipped with free-wheeling diodes to allow for current passing in the non-conductive direction of the IGBT, when needed.

Each of the three phases (v_a, v_b, v_c) can be connected to either $\pm V_{dc}/2$, independently of each other. Consequently, $2^3 = 8$ voltage vectors can be created where six of them are active and two are zero vectors, illustrated in Fig. 2.5. Note that voltage vector u_{111} and u_{000} are the so called zero vectors implying that all three phases simultaneously

are connected to either $\pm V_{dc}/2$. During operation the vectors are combined to achieve an average voltage corresponding to the references for each phase.

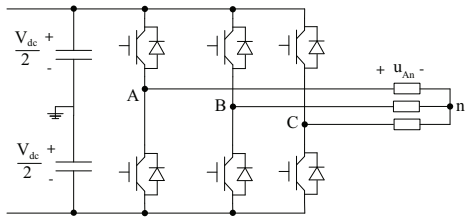

Figure 2.4 Illustration of a three-phase voltage source inverter

In the stationary reference frame ($\alpha\beta$-reference frame) the output vector $v_{\alpha\beta}$ are limited to [14]

$$v_\alpha = \left(0, \pm\frac{V_{dc}}{2}, \pm\frac{2V_{dc}}{3}\right) \tag{2.13}$$

$$v_\beta = \left(0, \pm\frac{2V_{dc}}{\sqrt{3}}\right), \tag{2.14}$$

which is a result of the amplitude invariant $\alpha\beta$-transformation according to

$$\begin{bmatrix} v_\alpha \\ v_\beta \end{bmatrix} = \begin{bmatrix} \frac{2}{3} & -\frac{1}{3} & -\frac{1}{3} \\ 0 & \frac{1}{\sqrt{3}} & -\frac{1}{\sqrt{3}} \end{bmatrix} \begin{bmatrix} v_a \\ v_b \\ v_c \end{bmatrix} = \frac{V_{dc}}{2} \begin{bmatrix} \frac{2}{3} & -\frac{1}{3} & -\frac{1}{3} \\ 0 & \frac{1}{\sqrt{3}} & -\frac{1}{\sqrt{3}} \end{bmatrix} \begin{bmatrix} s_a \\ s_b \\ s_c \end{bmatrix}.$$

The largest voltage magnitude that momentarily can be created is

$$|v_{\alpha\beta}|_{max} = \frac{2V_{dc}}{3}, \tag{2.15}$$

whereas the limit for linear modulation is

$$|v_{\alpha\beta}| = \frac{V_{dc}}{\sqrt{3}}. \tag{2.16}$$

In Fig. 2.5 this can be seen as the largest circle that can be created inside of the hexagon, illustrated by the dashed circle.

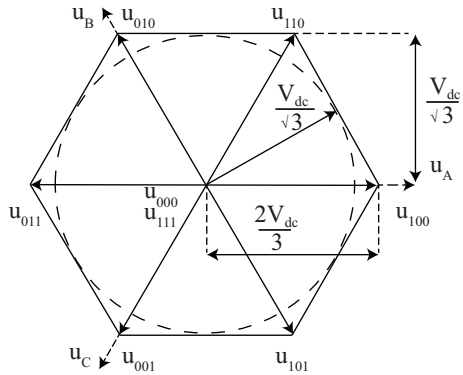

Figure 2.5 Illustration of voltage vectors for a two-level VSI

2.3 Pulse width modulation techniques

Pulse width modulation (PWM) is essential for operation of voltage source inverters. In principle, each of the three legs of the inverter is alternately connected to either $\pm V_{dc}/2$ to obtain a specific average voltage level. What differentiates different modulation techniques is the way in which the voltage vectors are combined, and especially how the zero vectors are used. Clearly, different selections of voltage vectors can be combined, in different orders, to create an average over one switching period corresponding to a given reference. However, the choice of voltage vectors and the combination will affect the performance of the drive system in terms of energy efficiency and phase current harmonics [14].

Different modulation techniques and switching frequency randomization are frequently researched and evaluated from an electrical perspective [21, 7, 8, 9, 10, 11]. In [21] different discontinuous PWM (DPWM) methods are investigated focusing on inverter energy efficiency. The authors conclude that DPWM is the modulation technique of choice due to a substantial decrease in losses as a result of the decreased number of switching events, i.e. number of commutations.

In [7] and [8], focusing on harmonic spreading and efficiency, different random PWM techniques are investigated. The authors conclude a significant decrease in harmonic intensity and advocates benefits from an EMI perspective. Most often harmonic spread of inverter output current, power spectral density and energy efficiency are considered while potential drawbacks such as noise emissions often are disregarded.

Although, modulation techniques' influence on magnetic noise have been investigated by several researchers as well [2, 3, 4, 5, 6, 22, 23, 24, 25, 26]. Specifically, [2, 3, 4, 5, 6] covers permanent magnet synchronous machines. Random switching fre-

quency PWM has been pointed out as the main technique, besides increasing the switching frequency, for improving the acoustic sensation [3, 6, 22, 23, 24, 25] thanks to the non-tonal spectrum around the switching frequency and its multiples. However, despite utilization of suggested sound quality metrics for quantification of the acoustic exposure as by Ma and Zuo [5], Sarrazin et al. [6] and Cho et al. [23], investigations on the perception due to modulation techniques have not been found in available literature.

For industrial applications, such as electrification of propulsion systems in the automotive industry, sideband harmonics around the switching frequency is normally in the hearable frequency range due to switching frequency in the region of 5-10 kHz. Obviously, the switching frequency can be increased and thereby potential issues related to noise and vibrations can easily be suppressed. With increased computational power and alternative switch topologies, such as silicon carbide based switches, it is a very realistic possibility. However, increasing the switching frequency in combination with switches with enhanced dV/dt capabilities might be problematic from an electrical interference perspective. It is likely that additional interference issues will arise in the electrical systems.

Consequently, the effects of randomization of the switching frequency is of interest to investigate, primarily from a noise perspective. The technique is simple and seems like a yet effective measure to decrease the switching noise from electric drive units. Simply by the smearing out the harmonic components and thereby decrease the tonality. However, it is not evident that this will have any positive effects on the experienced noise, which at first thought might seem contradictory. The reason for this is that tonality is not by any means the only sound quality metrics. Alongside tonality, measures such as overall sound pressure level might be more influential on the perceived annoyance. Although, the technique is simple and seems like a yet effective measure to decrease the switching noise from electric drive units. Another area of interest is the combination of for example DPWM and randomization of the switching frequency in order to harvest the benefits of DPWM while at the same time suppress its drawbacks.

The modulation techniques investigated in this work is based on carrier wave comparison. In Fig. 2.6 the carrier wave comparison is illustrated. The times located on the x-axis illustrates a total time equal to the switching period time. As can be seen, the switching period is divided into 7 sections marked with the times t_0, t_1, t_2 and t_7. Of these ones, t_0 and t_7 are zero vectors whereas t_1 and t_2 are active vectors. The voltage references are obtained from the control system and averaged over one switching period, hence the output average equals the reference value for each phase.

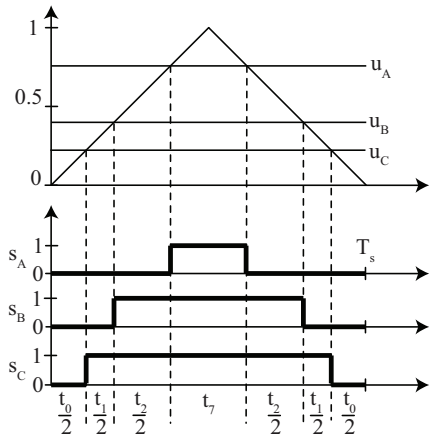

Figure 2.6 Carrier wave comparison example

2.3.1 SPWM with third harmonic injection

As previously discussed in Section 2.2, the theoretical limit for linear modulation is $|v_{\alpha\beta}|_{max} = V_{dc}/\sqrt{3}$. However, this limit can not be reached without any form of reference alterations. For example, if a voltage reference of $v_{\alpha\beta} = V_{dc}/\sqrt{3} + j0$ is to be realized, the average values of the switching states required during a switching period are $\left[2/\sqrt{3},\ -1/\sqrt{3},\ -1/\sqrt{3}\right]$ (according to the amplitude invariant transformation presented in (2.2)). Note that $s_a = 2/\sqrt{3} > 1$ which will cause overmodulation. Consequently, the maximum output voltage magnitude possible without any alterations of the three-phase voltage references is

$$|v_{\alpha\beta}|_{max} = \frac{\sqrt{3}}{2}\frac{V_{dc}}{\sqrt{3}} = \frac{V_{dc}}{2} \tag{2.17}$$

resulting in average switching states of $[1,\ -1/2,\ -1/2]$, which is achievable in the linear modulation region.

To overcome the previously explained issue with the limitation of not being able to utilize the entire hexagon, presented in Fig. 2.5, zero sequence injection is used. In accordance with three-phase theory of wye-connected machines, a zero sequence component of arbitrary magnitude can be added to all three phases without in any way affecting the resulting three-phase system. A prerequisite is that the load is symmetrical, which is a reasonable assumption for electrical machines. The technique used to maximize the utilization of the hexagon is the symmetrical suboscillation method. The zero sequence component, Δ, to be added to the three references is calculated based on the instantaneous

values of the three phases according to [14]

$$\Delta = \frac{max\,(u_a,\,u_b,\,u_c) + min\,(u_a,\,u_b,\,u_c)}{2}. \tag{2.18}$$

In practice, the method creates a continuous symmetry between the maximum and minimum values of the phase voltage references, and thereby enabling higher output voltage without overmodulation. In Fig. 2.7 and 2.8 the concept is illustrated. In Fig. 2.7 the zero sequence component can be seen. With the proposed method it has the shape of a triangular wave. In Fig. 2.8 the results of adding the zero sequence to the sinusoidal references are seen. Note that there is a symmetry where, at any time, the maximum value of the three phases has the same magnitude but opposite sign to the minimum value of the three phases.

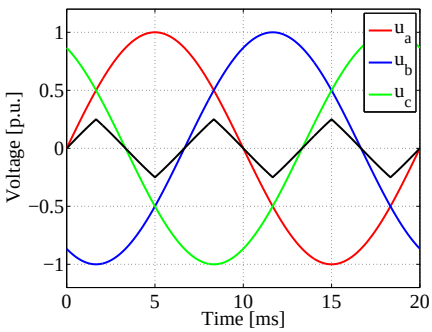

Figure 2.7 Sine phase potential references and the zero sequence component based on the symmetrical suboscillation method

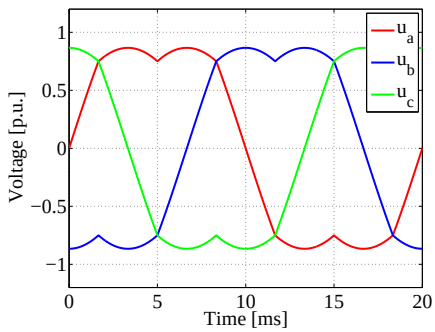

Figure 2.8 Resulting phase potential references obtained by addition the zero sequence component to all three phases

2.3.2 Discontinuous PWM

Discontinuous PWM (DPWM) is a category of modulation techniques where the common objective is to clamp phase voltages to either $\pm V_{dc}/2$ to reduce the number of commutations and thereby the inverter losses. Several approaches, with the aim to increase energy efficiency are presented in literature [27, 28]. In [27] space-vector based synchronized DPWM for applications with large ratios between the switching frequency and fundamental frequency is evaluated. The work focuses on switching losses and total harmonic distortion (THD) of both the voltage and the phase current, using a three-level inverter. Four DPWM strategies (DPWM I-IV) are investigated. The author differentiate among these based on when the clamping occurs and the angular spread of the clamping, i.e. the number of electrical degrees one phase is clamped. The paper concludes several

benefits using DPWM in general, such as decreased switching losses and unsurprisingly even a decrease in phase current THD for the given load case.

Hadj [28] investigates DPWM using a fixed clamping interval of 60 electrical degrees. The author conclude that the method reduces the inverter switching losses for the given load case. However, results for operational points other than the one covered as well as the impact on electromagnetic torque characteristics are not treated.

However, lacking in available literature are analyzes covering the effects on electromagnetic torque ripple, more comprehensive energy efficiency investigations and the results on machine losses and radiated noise and vibrations.

In this section a few DPWM methods are considered, closely related to what is described as DPWM II and III by Beig et al. [27]. Initially, the DPWMMIN and DPWMMAX are discussed, thereafter the DPWM30 and DPWM60 methods are covered.

DPWMMIN and DPWMMAX are two methods that are conceptually the same, but operates as the inverse to each other. When using DPWMMAX, the objective is to clamp the phase with the highest reference voltage to $+V_{dc}/2$ whereas the DPWMMIN method clamps the phase with the lowest reference voltage to $-V_{dc}/2$. The objective is to decrease the number of commutations and lower the inverter losses. As for the aforementioned techniques, third harmonic injection is utilized by adding additional signal content to the three phases, as discussed in the previous section.

Mathematically, DPWMMIN and DPWMMAX are expressed as

$$u_0 = \begin{cases} \frac{V_{dc}}{2} - max\left(u_a, u_b, u_c\right) & \text{DPWMMAX} \\ -\frac{V_{dc}}{2} - min\left(u_a, u_b, u_c\right) & \text{DPWMMIN} \end{cases}$$

where u_0 is the zero sequence component to be subtracted from the phase voltage references.

In Fig. 2.9 and 2.11 phase voltage references and the calculated zero sequence components are presented for DPWMMAX and DPWMMIN, respectively. In Fig. 2.10 and 2.12 the resulting phase voltage when the zero sequence component is subtracted are presented for both methods.

As can be seen, both methods clamp one phase at the time to either $\pm V_{dc}/2$ during a total of 120 electrical degrees. Considering the consequences of this technique, it is evident that in total one of the phases remains clamped through out each and every switching period reducing the number of commutations by 1/3. The attentive reader obviously questions the reason for centering the clamping period over the peak voltage when it would decrease the losses even further if it is phase shifted to clamp during a period when the transmitted power is at its peak. Clearly, there are a few options in how to place the clamping region. This study is limited to clamping around the peak voltage as an initialization to DPWM methods.

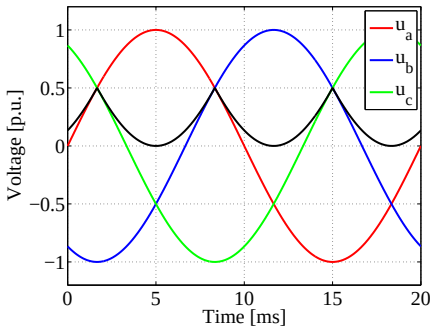

Figure 2.9 Sine phase potential references with zero sequence component using DPWMMAX

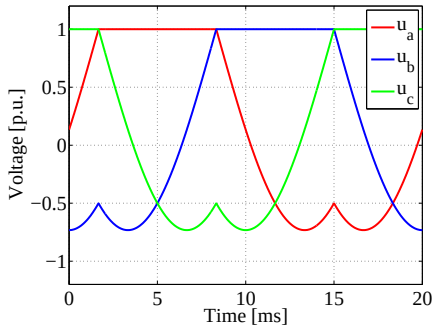

Figure 2.10 Resulting phase potential references using DPWMMAX

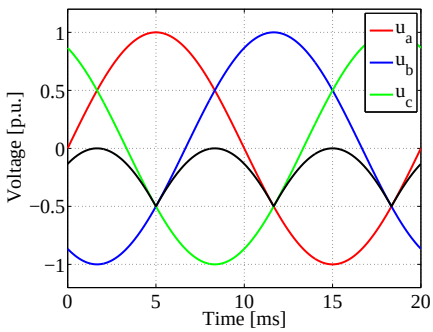

Figure 2.11 Sine phase potential references with zero sequence component using DPWMMIN

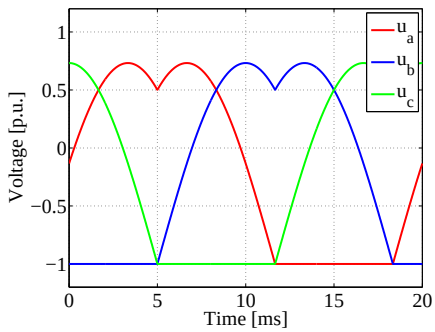

Figure 2.12 Resulting phase potential references using DPWMMIN

2.3.2.1 DPWM30 and DPWM60

The DPWMMIN and DPWMMAX methods can be combined and switched in between as the voltage reference propagates in the $\alpha\beta$-reference frame. Combining these differently gives rise to additional sub-categories of DPWM. Two of these are covered in this section; DPWM30 and DPWM60.

Instead of only using DPWMMIN or DPWMMAX, both can be combined to increase performance while still keeping the number of commutations to a minimum. Conceptually, DPWM30 and DPWM60 are the same. The methods switches between DPWMMIN and DPWMMAX, using the one that is the more favourable.

In Fig. 2.13 it is illustrated how DPWMMIN and DPWMMAX are used and

combined. For DPWM30, the active clamping (δ) occurs during 30 electrical degrees, whereas for DPWM60 the active clamping occurs during 60 electrical degrees. In Fig. 2.14 and 2.15 the DPWM60 method is illustrated. As can be seen, the phase potentials are clamped to either $\pm V_{dc}$. Clearly, a consequence of the method is distortion to the reference potentials. In this work, the DPWM60 method is used. In the remaining of the thesis the shortened abbreviation DPWM is used for DPWM60.

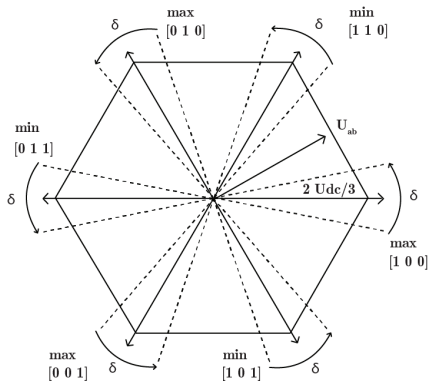

Figure 2.13 Illustration of where to use DPWMMIN (min) and DPWMMAX (max)

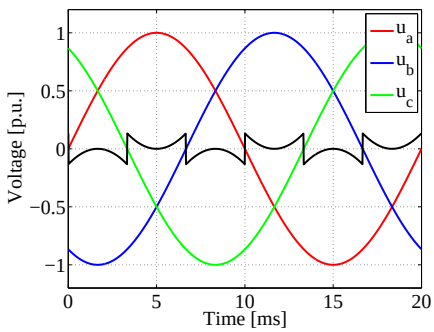

Figure 2.14 Sine phase potential references with zero sequence component using DPWM60

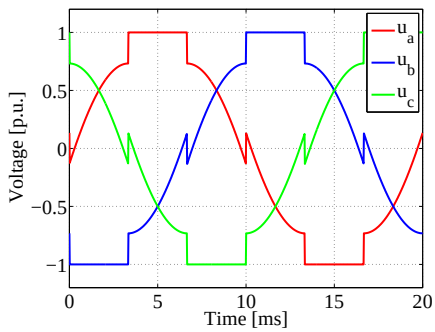

Figure 2.15 Resulting phase potential references using DPWM60

2.3.3 Random PWM

In order to decrease the tonality in the emitted noise from the machine, randomization of the switching frequency can be used. As previously discussed and further evaluated in Chapter 7 and 8, the tonality of the emitted noise is thought to be a variable of importance

for the perception of noise hence motivating the need for investigation. In the work presented, the randomization is based on a given distribution with an expected value and a variance. Both Uniform and Gaussian distributions have been considered, implemented and evaluated.

Implementation of variable switching frequency can be done in different ways. In the configuration selected, the switching frequency defines the data sampling and the update frequency of the control system. The phase current sampling is synchronous with the trigger wave for the PWM and samples are collected at the start of each switching period. The data collection from the rotor position resolver is done synchronously as well. This data is collected in the center of each switching period. This selection is based on limitations in the equipment used in the experimental testing. Subsequently, the second half of the switching period is intended for the control system to calculate the next reference values to be supplied to the PWM modulator.

When the switching frequency is changed, the delay from sampling to execution needs to be supervised and known to a high certainty for accurate compensation to be possible. Moreover, the integrators in the controllers needs to be considered when the update frequency is changed in the control system, to assure that errors are not introduced. Collectively, scheduling and timing is of importance when randomization of the switching frequency is used.

2.4 Loss calculations

2.4.1 Core loss calculations

The machine losses are divided into two categories, core losses and copper losses. Magnet losses are not included in the work presented. The core losses include eddy current and hysteresis losses in the stator teeth and the stator yoke, as well as the rotor.

Eddy currents are introduced when a conductive material is subjected to a varying magnetic field, losses due to this phenomena is known as eddy current losses. Typically, thinner lamination sheets are used to reduce the eddy current by restricting the ability for the current to flow. As presented in [15], the eddy current losses are proportional to the square of the lamination thickness. Hysteresis losses occurs due to that the magnetic domains of the ferromagnetic material is forced to change their alignment. It is dependent on material properties such as grain size and the external magnetic fields intensity and frequency.

The combined contribution can be summarized with the simplified Bertotti-model

as

$$P_{fe} = k_h f B_{max} + k_c f^2 B_{max}^2 \tag{2.19}$$

where k_h and k_c are constants, f is the fundamental frequency and B_{max} is the peak flux density [15]. The first part constitutes the hysteresis losses and the second part the eddy current losses. Excess losses, which sometimes are used as a complement to the hysteresis and the eddy current losses, added by an additional third term is not included in this work. The motivation for this is that the hysteresis losses and the eddy current losses are representing the total losses hence the excess losses are zero.

For analytical calculations the domain of (2.19) is limited due to its usage of only a fundamental component. If the flux density were to be decomposed and evaluated for each harmonic according to (2.19), it is reasonable that high frequency flux density harmonics might cause non-negligible core losses even though their magnitude are much lower than the fundamental, especially considering the contribution of the eddy current losses. The resistive losses in the stator windings are defined as

$$P_{cu} = \rho \int J^2 dV \tag{2.20}$$

where ρ is the resistivity and J is the current density in the windings. The volume integral covers the conductor area times the stack length, hence end winding effects are not included. Effects such as skin effect and proximity effects are neglected.

2.4.2 Inverter losses

The inverter loss calculations are based on the energy loss data for the IGBT modules provided by the manufacturer. The energy loss during turn on, turn off and reverse recovery is used to derive a complete outlook over the inverter losses.

The provided loss data is only valid for a single operating point, and is therefore linearly scaled with current and voltage to be universal. The energy losses for IGBT switching on or off and diode reverse recovery are thereby described as

$$E_{on} = E_{on,ref} \frac{V_{dc}}{V_{ref}} \frac{i_{ph}}{I_{ref}} \tag{2.21}$$

$$E_{off} = E_{off,ref} \frac{V_{dc}}{V_{ref}} \frac{i_{ph}}{I_{ref}} \tag{2.22}$$

$$E_{rr} = E_{rr,ref} \frac{V_{dc}}{V_{ref}} \frac{i_{ph}}{I_{ref}}. \tag{2.23}$$

2.5 Longitudinal vehicle dynamics modelling

Drive cycle assessments are used as an additional evaluation tool, creating further understanding and quantification of the impact of various solutions. To enable drive cycle analyses, a vehicle dynamics model is required where the dynamics of the mechanical system is models. As with any modelling, is can be done with different levels of detailing. In this thesis a fairly simple longitudinal vehicle dynamics model is used. The model resembles a uni-directional two-axis vehicle including aerodynamic drag, rolling resistance and the force required for vehicle acceleration, suitable for energy efficiency and fuel consumption studies [29].

Despite the somewhat coarse detailing, the model is considered sufficiently accurate for the purpose of its usage to be fulfilled, to give an understanding of the impact of various solutions. At firsthand, the drive cycle assessment is used in comparative studies. The impact of load distribution, which occurs during acceleration and braking or due to the vehicle body acting as a lever while subjected to aerodynamical forces, is not included. Neither is the traction limitation and the tire slip and force relations in the contact patch between tire and tarmac. The maximum vehicle acceleration in the drive cycle used, the Extra Urban Driving Cycle (EUDC), is 0.833 m/s^2 which is considered moderate.

The dynamics of any moving object in one direction can be expressed according to Newton's second law of motion as

$$ma = m\frac{dv}{dt} = \sum F \tag{2.24}$$

where m is the vehicle mass, a is its acceleration and $\sum F$ is the summation of forces acting on the vehicle, in this case summarized as

$$\sum F = F_{tractive} - F_d - F_r \tag{2.25}$$

where $F_{tractive}$ is the driving force generated by the electric powertrain, F_d is the aerodynamic drag and F_r is the rolling resistance. The aerodynamic drag and the rolling resistance are expressed as

$$F_d = \frac{1}{2}\rho_a C_d A_f v^2 \tag{2.26}$$

$$F_r = C_r mg \tag{2.27}$$

where ρ_a is the air density, C_d is the drag coefficient, A_f is the vehicle frontal area, v is the vehicle speed, C_r is the rolling resistance coefficient and m and g are the vehicle mass and the gravity constant [29].

The force required for acceleration, F_{acc}, needs to be included in the model. It is calculated as

$$F_{acc} = m\frac{dv}{dt}. \tag{2.28}$$

The vehicle data used to parameterize the vehicle model is based on the Volvo C30 Electric, presented in Table 2.1.

Table 2.1 Vehicle dynamics model data, based on Volvo C30 Electric

Parameter	Abbreviation	Value	Unit
Aerodynamic drag coefficient	C_d	0.28	-
Frontal area	A_f	2.18	m^2
Air density	ρ	1.225	kg/m^3
Rolling resistance coefficient	C_r	0.009	-
Vehicle mass	m	1660	kg
Tire radius	r_t	0.32	m
Gear ratio	R_g	8	-

Chapter 3

Electromagnetic forces in relation to NVH for a PMSM

Over the past decade, noise and vibrations from electric drives has increasingly become an area of attention for both academia and industry. The absence of the broad band noise from the internal combustion engine brings new noise, vibration and harshness (NVH) challenges for hybrid/electric vehicle applications.

Noise and vibrations from an electrical drive unit can be categorized based on origin as either electromagnetic, mechanic or aerodynamic. Mechanical noise arise due to mechanical interaction in for example bearings and speed reducers whereas aerodynamic noise is a result of air flow due to mechanical movement [1]. Electromagnetic noise from electrical machines is of particular interest in automotive applications and focused upon in this thesis. It is not only related to the geometrical design of the electrical machine, but also to the choice of control approach and voltage modulation strategy, which is discussed more in detail in Chapter 6 and 7.

The forces acting on the inside of the machine can be decomposed into airgap forces and magnetostrictive forces. Magnetostrictive forces are cased by the magnetic fields ability to stress the iron in the field direction and thereby cause the mechanical structure to deform. Radial and tangential airgap forces are orthogonal to each other and can be explained as attraction and repulsion between the stator and rotor in radial and tangential direction, respectively [30].

Furthermore, the radial component of the air gap forces can be viewed as a byproduct due to lack of contribution to the rotational movement, which is solely a result of the tangential force component. However, radial forces can contribute significantly to mechanical displacements of the stator yoke which results in emitted noise due vibrations.

Additionally, the tangential component acting on the stator teeth tips creates bending in the stator teeth causing local deformation influencing the over-all stator deformation. Besides electromagnetic noise, primarily mechanical noise is a significant contributor to the total noise from the rear axle drive unit. However, in this work only electromagnetic noise is covered.

The relation between airgap flux density and force density can be expressed with Maxwell's stress tensor as

$$f_n = \frac{1}{2\mu_0}\left(B_n^2 - B_t^2\right) \tag{3.1}$$

$$f_t = \frac{1}{\mu_0}\left(B_n B_t\right) \tag{3.2}$$

where f_n, f_t, B_n, B_t and μ_0 are radial and tangential force densities, radial and tangential flux densities and absolute permeability, respectively [31, 32, 33, 34]. The relation between flux density and force density and its harmonic content is further discusses in Section 3.3 and thoroughly analyzed in Chapter 6. Although, before the electromagnetic forces are investigated, the flux density needs to be discussed due to its influence on the force density. As discussed by Chang et. al [33] and Zhu et. al [34], the Maxwell Stress Tensor method is a straight forward and fairly simple way of calculating the forces, and in literature it is commonly used. However, local errors due to coarseness in the model discretization and selection of integration contour are areas of concern. The centerline in the airgap is selected as contour for data collection in the majority of the data presented in this work.

3.1 Modal analysis

Flux distribution or force density appearing in the airgap can be analysed based on descriptions relating to different domains. They can be described in either spatial or temporal domains, e.g. space or time. To understand the analyses in the continuation of the thesis as well as the methodology, it is of high importance to understand the concept of modal analysis.

The relation between spatial, temporal and frequency domains can be exemplified by a cylindrical shell that is excited by either a periodically varying forces or by simply being struck. The vibration response contains a finite number of pure tones, vibrating at certain discrete frequencies. The deformation, or vibrational pattern, can be expressed with modal analysis. In analogy to frequency domain analysis where a signal can be decomposed into a finite number of frequency harmonics with specific magnitudes, frequencies and phase angles, a deformation or a vibrational pattern of an object

can be decomposed into a finite number of mode shapes characterized by displacements, mode shapes and frequencies (modal frequencies). Hence, the complete dynamics of the deflection can be described by the superimposition of the individual mode shapes. Although complete knowledge is needed to understand the dynamics of the system as a whole, each of the mode shapes holds the information about the specific (relative) deformation of that modal frequency. In a similar manner, the flux distribution and the force density in the airgap can be expressed with modal analyses considering the quantities by fourier decomposition as standing waves that propagate in time and space. In Fig. 3.1 mode shapes $N = 2$ and $N = 5$ are illustrated. The dashed circle represents the item at rest, as a perfectly shaped circle. Mode shapes can be defined by the modal number as the number of lobs in the deformation.

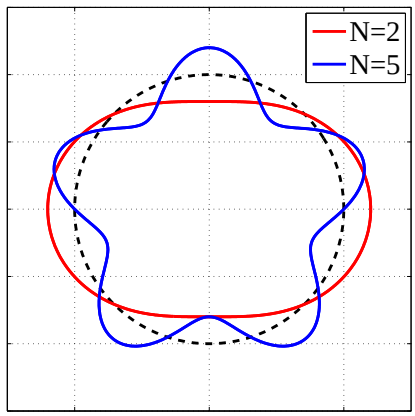

Figure 3.1 Illustration of circumferential mode shaped $N = 2$ and $N = 5$

On the topic of electrical machines, low circumferential mode numbers are of highest importance from a noise and vibration perspective [35]. Simplified, the mechanical deflection Δd of the stator yoke is inverse proportional to the mode number to the power of four, as

$$\Delta d \propto \frac{1}{N^4}. \tag{3.3}$$

Considering a mode shape or vibrational order with order 2 and a frequency of twice the electrical fundamental frequency, i.e. $f_r = 2f$ and $N = 2$. In comparison to a vibrational mode of $f_r = 2f$ and $N = 4$, magnetic force in the latter mode will be $1/16$ of the former [1].

The first mode, $N = 0$, is the so called breathing mode. Its shape is cylindrical and

the motion is solely based on radial expansion and contraction caused by a force density uniformly distributed around the stator periphery that are periodic with time. Without loosing generality, such a magnetic force f can be expressed as

$$f_0 = A_0 cos(\omega_0 t) \tag{3.4}$$

where f_0 is the force density, A_0 is a scaling factor and $\omega_0 t$ is the frequency of the mode shape. The subscript 0 indicates mode shape $N = 0$. The second mode shape, $N = 1$, is the bending mode, which can be seen as a beam in bending expressed as

$$f_1 = A_1 cos(\omega t - \alpha). \tag{3.5}$$

As the equation indicates, a single sided magnetic pull/rejection will occur which causes the bending force, rotating with an angular frequency of ω_1. The next mode shapes $(N = 2, 3, 4, ...)$ are so called oval modes which will generate wave shaped deformations as those depicted in Fig. 3.1 [1]. It is worth noting that when expressing airgap flux density, force density or vibrations in terms of modes and modal frequencies, one mode shape can oscillate with different frequencies, meaning that the mode-shapes are not necessarily tied to a single frequency component. This is not to be confused with eigenfrequencies where one mode-shape as a certain eigenfrequency.

If the frequency of the mode shapes, excited by for instance electromagnetic forces in the machine, coincides with natural frequencies of the machine, resonance occur [35]. Consequently, the stator vibrations is dependent on the electromagnetic design of the machine, the operating point and the mechanical design of the system. The electromagnetic design will affect the appearance of flux distribution and force density, the operating point affects the frequencies of the different mode shapes as described in for example (3.4) and (3.5), and the mechanical design affects the natural frequencies of the system. On the basis of this reasoning, it is reasonable that the acoustic response varies strongly with the rotational speed. Areas of particular concern might arise as a consequence of resonance. In other words, the acoustic response might be problematic at certain frequencies if resonance occur.

3.2 Airgap flux density

3.2.1 Appearance of flux density

The flux field appearing in the airgap can be categorized based on its origin. By superposition, the airgap flux density can decomposed into origin from armature and PM (rotor).

In the remaining of this section, the analytical expressions for the airgap flux density are presented and the influence of the stator slots are discussed.

3.2.1.1 Rotor generated flux distribution

The radial component of the rotor flux, originating from the permanent magnets, can be expressed as [1, 36, 37],

$$B_{n,m} = \sum_{u=2k-1} B_{m,u} cos\left(up\omega t - up\theta\right) \tag{3.6}$$

where $k = 1, 2, 3...$, p is the pole-pair number, ωt is the mechanical frequency and θ is the mechanical circumferential angle stretching along the airgap. As shown in (3.6) the harmonic content of the rotor harmonics consists of pure circumferential orders, indicated by the equal orders of both frequency and mode number [1, 36]. Note that all harmonics rotate synchronously with the rotational speed of the machine due to the inherent synchronicity in the machine, which would not be the case for an induction machine.

In Fig. 3.2 the radial flux density is presented during no-load operation, the data is obtained from FEM-simulations. In the y-direction, mark *Position* (ωt), the time dependency can be seen. In the x-direction, marked *Position* (θ), the space dependency can be seen. In Fig. 3.3 the corresponding 2D-FFT of the time and space domain data is presented in a frequency/wave-diagram. Space and time dependencies are described with mechanical references by the x-axis and the y-axis, respectively. Each of the harmonics consist of a vibrational/circumferential mode that rotates with a certain frequency. As previously described and explained by (3.6) the harmonics are synchronous with the rotational speed of the machine. This can be seen as the harmonics on the diagonal passing through circumferential order n=0. The data is presented with logarithmic z-axis to clearer illustrate the harmonic content. As can be seen, there are some outliers at vibrational orders -50 and 40 which is not represented in (3.6). These are caused by the slotting of the stator, which is further discussed in Section 3.2.2.

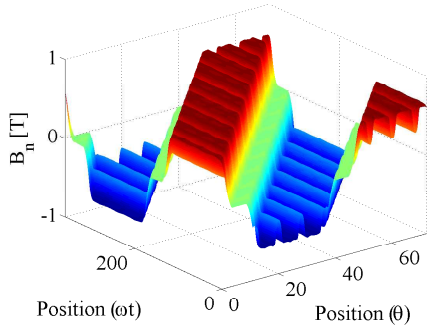

Figure 3.2 Radial airgap flux density as a function of both time (ωt) and space (θ) at no-load

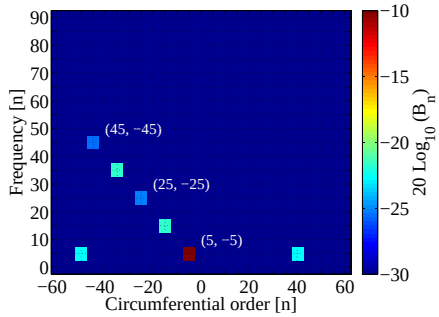

Figure 3.3 Frequency and mode number of the radial airgap flux density at no-load derived by 2D-FFT, normalized with the number of pole-pairs

3.2.1.2 Stator generated flux distribution

Consider an ideal stator with a three-phase winding where the phases are evenly distributed, spatially shifted by ± 120 electrical degrees, distributed in a fictitious manner without slots nor discrete winding distribution. Exciting this fictive three-phase winding with a fixed (non-varying) three-phase current, the resulting flux-density at any time instance being observed in the airgap along the span of the stator can be expressed as

$$B_{n,s} \propto cos(p\theta) \tag{3.7}$$

where $B_{n,s}$ is the armature flux density in radial direction, p is the pole-pair number and θ is the mechanical circumferential angle. Clearly, at any time instance the flux would appear sinusoidal in space. If the stator excitation is changed to a sinusoidally varying current with electrical frequency $p\omega t$, the flux density can instead be studied as a function of time at a single point, geometrically, where it now would appear sinusoidal too. This can be seen by studying Fig. 3.2. At the geometric position $\theta = 0$, the fundamental temporal component of the flux density can be seen propagating along the axis marked *Position (ωt)*. Likewise, at time instance ωt=0, one can see the propagation in space along the axis marked *Position (θ)* where the fundamental component is clearly seen. Considering only the fundamental component, this can mathematically be expressed as

$$B_{ns} \propto cos(p\omega t)cos(p\theta) = \frac{1}{2}\left[cos\left(p\omega t - p\theta\right) + cos\left(p\omega t + p\theta\right)\right] \tag{3.8}$$

using the trigonometric identity $cos(\alpha)cos(\beta) = 0.5\left[cos(\alpha-\beta)+cos(\alpha+\beta)\right]$. The first term on the right hand side of (3.8) rotates backwards whereas the second term

rotates forward, visualizing the concept of backward and forward rotating fields [15]. As can be seen, the flux propagates both spatially and temporally, in relation to the previous discussion in Section 3.1.

With analogy to circuit theory, the magnetic flux follows the path of least reluctance, where reluctance is similar to resistance in an electric circuit. As the reluctance in the airgap by far exceeds the reluctance in the iron material, the intensity of the magnetic field in the airgap is very high. The armature excitation and the flux density can be linked by Hopkinsons law, where reluctance equals the magnetomotive force divided by the flux. Consequently, the flux density is proportional to the magnetomotive force divided with the airgap reluctance. When a current flow in the stator windings, a magnetomotive force (MMF) arise in the airgap, expressed in ampere-turns. With the use of MMF, the armature excitation and the flux can be linked as

$$B(\theta,t) = \mathscr{F}(\theta,t)\Lambda(\theta). \tag{3.9}$$

Focusing only on the harmonic content, the following MMF waves originating from the three phases are obtained at a given time

$$\mathscr{F}_{s,a} \propto \sum_{v=1,3,5,\ldots} i_a cos(vp\theta) \tag{3.10}$$

$$\mathscr{F}_{s,b} \propto \sum_{v=1,3,5,\ldots} i_b cos\left[vp\left(\theta - \frac{2\pi}{3}\right)\right] \tag{3.11}$$

$$\mathscr{F}_{s,c} \propto \sum_{v=1,3,5,\ldots} i_c cos\left[vp\left(\theta - \frac{4\pi}{3}\right)\right] \tag{3.12}$$

where i_a, i_b and i_c are the momentary phase currents in the given time instance. The amplitude of the MMF depends on various scaling factors defined by the machine design such as number of turns in the stator, distribution factor etc.

Spatially, the MMF wave produced by each winding is of a square wave characteristics hence the appearance of only odd harmonics. The appearance of a square wave is due to the discretization which is a result of the winding distribution and the stator slots. This is clearly seen in Fig. 3.2. Multi-layer winding configurations can be used to smoothen the characteristics, which will change the magnitude of spatial harmonics. Note that the third harmonic is spatially in phase for all three phases and will not be present when the three phases are summed up, due to the three-phase symmetry in the machine.

Adding the influence of time to the magnetomotive force of the three phases, the following is obtained

$$\mathscr{F}_{s,a} \propto \sum_{v=1,3,5,\ldots} cos(p\omega t)\,cos(vp\theta) \tag{3.13}$$
$$= \frac{1}{2}\sum_{v=1,3,5,\ldots} [cos(p\omega t - vp\theta) + cos(p\omega t + vp\theta)]$$

$$\mathscr{F}_{s,b} \propto \sum_{v=1,3,5,\ldots} cos\left(p\omega t - \frac{2\pi}{3}\right) cos\left(v\left(p\theta - \frac{2\pi}{3}\right)\right) \tag{3.14}$$
$$= \frac{1}{2}\sum_{v=1,3,5,\ldots} cos\left[p\omega t - vp\theta + (v-1)\frac{2\pi}{3}\right] +$$
$$\frac{1}{2}\sum_{v=1,3,5,\ldots} cos\left[p\omega t + vp\theta - (v+1)\frac{2\pi}{3}\right] \tag{3.15}$$

$$\mathscr{F}_{s,c} \propto \sum_{v=1,3,5,\ldots} cos\left(\omega t - \frac{4\pi}{3}\right) cos\left(v\left(p\theta - \frac{4\pi}{3}\right)\right) \tag{3.16}$$
$$= \frac{1}{2}\sum_{v=1,3,5,\ldots} cos\left[p\omega t - vp\theta + 2(v-1)\frac{2\pi}{3}\right] +$$
$$\frac{1}{2}\sum_{v=1,3,5,\ldots} cos\left[p\omega t + vp\theta - 2(v+1)\frac{2\pi}{3}\right] \tag{3.17}$$

and summarizing the contributions the total MMF from the stator excitation $\mathscr{F}_s$ and the flux density can be expressed as

$$\mathscr{F}_s = \mathscr{F}_{s,a} + \mathscr{F}_{s,b} + \mathscr{F}_{s,c} \propto \sum_{v=6k\pm1} cos(p\omega t \mp vp\theta) \tag{3.18}$$

$$B_{n,s} = \Lambda\mathscr{F}_s \propto \Lambda \sum_{v=6k\pm1} cos(p\omega t \mp vp\theta) \tag{3.19}$$

where $k = 0,1,2,\ldots$ and Λ is the airgap permeance [1, 36]. Of the spatial harmonics, $v = 1,5,11,17\ldots$ rotate forwards (indicated by the negative sign before the second term in the cosine function) whereas the harmonics $v = 7,13,19,\ldots$ rotate backwards. Note that the harmonics only consists of forward and backward rotating fields, all with a frequency equal to the fundamental electrical frequency. The harmonics $v = 3,9,15,\ldots$ are shifted in space by 0, -120 and -240 electrical degrees for the three phases and are therefore not appearing in the summation of the contribution from all three phases, as previously discussed.

In Fig. 3.4 the radial flux density is presented for a case with only armature excitation, the data is obtained with a solid rotor without any magnets or flux barriers to

remove the influence of rotor flux and reluctance variations in the rotor. In the y-direction, mark *Position* (ωt), the time dependency can be seen. In the x-direction, marked *Position* (θ), the space dependency can be seen. In Fig. 3.5 the corresponding 2D-FFT of the time and space domain data is presented in a frequency/wave-diagram. As can be seen, the strongest circumferential orders are $-p = -5$, which is in line with theory obtained by $k = 0$ in (3.19). It is clearly seen that the harmonics present are focused at the frequency $p\omega t$. Additionally, harmonics appear at the orders $n = 40$ which is not consistent with (3.19). As for the rotor flux distribution, this is a result of the slotting in the stator, which is discussed in the following section. Comparing Fig. 3.4 to Fig. 3.2, it is seen that the flux has more sinusoidal characteristics in both time and space which is a result of the sinusoidal current exciting the stator windings. The influence of the stator slots can graphically be seen in both figures.

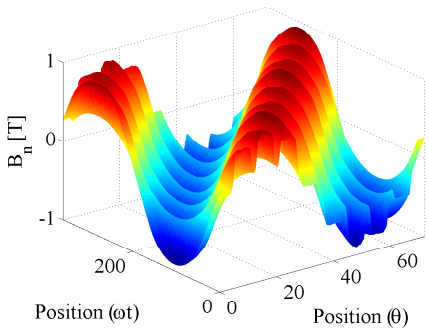

Figure 3.4 Radial airgap flux density as a function of both time (ωt) and space (θ) with only stator excitation

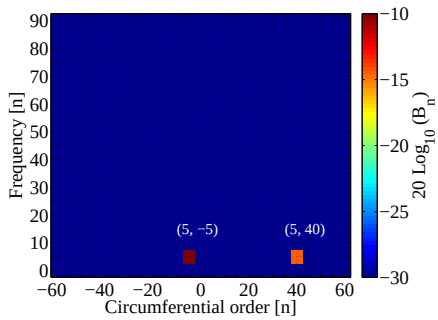

Figure 3.5 Frequency and mode number of the radial flux density from stator excitation derived by 2D-FFT

3.2.2 Effects of stator slots

When slots are introduced in the stator, a variation occurs in the airgap reluctance and hence the permeance. As previously discussed, the flux can be expressed by the product of magnetomotive force $\mathscr{F}(\theta,t)$ and permeance $\Lambda(\theta)$, as $B(\theta,t) = \mathscr{F}(\theta,t)\Lambda(\theta)$. A part of the rotor outer arc that is aligned with a stator tooth is in a preferred position experiencing minimum reluctance. Resultantly, the magnetic field is at its peak. Likewise, when a part of the rotor outer arc is aligned with a stator slot, the resulting magnetic field is at its minimum due to the increased reluctance. When the rotor position is changed the pulsating magnitude difference in the magnetic field creates a force density which peaks during the alignment with the teeth and vise versa during alignment with the slots.

The influence of the variable permeance is seen in both the armature field and the rotor field. The previously derived equations for the MMF and the flux densities can be multiplied with a set of cosine functions representing the variations in the permeance, in order to include its influence on the harmonic content. The permeance can be expressed as a set of cosine functions with a periodicity defined by the an integer multiplier of the number of slots as

$$\Lambda = \Lambda_{g0}\left[1 + \sum_{x=1,3,5,\ldots} A_x cos(xN_s\theta)\right] \simeq \sum_{x=0,1,3,5,\ldots} A_x cos(xN_s\theta) \tag{3.20}$$

where N_s is the number of stator slots and A_x is the magnitude of the x^{th} harmonic [1]. Assuming that the permeance can be represented with a square wave, the harmonics appearing are all odd. Multiplying the obtained MMF in (3.18) with the variable permeance, the following expression is obtained for the armature flux density

$$B_{n,s} \propto \sum_{v=6k\pm1} \sum_{x} cos\left(p\omega t \mp vp\theta \pm xN_s\theta\right) \tag{3.21}$$

where $k, m = 0, 1, 3, 5, \ldots$. As the equation explains, additional space harmonics arise whereas the time frequency content is unchanged.

As can be seen in (3.21) with $k = 0$ and $x = 1$, the vibrational order $n = (-p + N_s) = 40$ arise. This harmonic is clearly seen in Fig. 3.5, rotating with a frequency of $p\omega t$.

In a similar fashion, the PM flux density can be multiplied with the same permeance function resulting in the following expression

$$B_{n,m} \propto \sum_{u=2k-1} \sum_{x} B_{m,u} cos\left(up\omega t - \left(up \pm xN_s\right)\theta\right). \tag{3.22}$$

As can be seen in (3.22) with $k = 1$ and $x = 1$, the vibrational orders $n = -50$ and $n = 40$ arise. These two are clearly seen in Fig. 3.3, rotating with the frequency $p\omega t$.

3.3 Electromagnetic forces

In this section the derivation of the radial force density acting on the stator is presented. For this analysis the Maxwell Stress Tensor presented in (3.2) is used and simplified accordingly,

$$\begin{aligned} f_n(\theta,t) &= \frac{1}{2\mu_0}\left[B_n(\theta,t)^2 - B_t(\theta,t)^2\right] \\ &\simeq \frac{1}{2\mu_0}B_n(\theta,t)^2 \\ &= \frac{1}{2\mu_0}\left(B_{nm}(\theta,t) + B_{ns}(\theta,t)\right)^2 \end{aligned} \tag{3.23}$$

where subscripts n and t indicates radial and tangential components and m and s indicate origin from permanent magnets or stator excitation, respectively. Three parts are obtained if the equation is further evolved, contributions from the armature field only, permanent magnets only and a contribution from the interaction of both fields.

If, for simplicity, no cross coupling of harmonics are considered nor any stator slot influence, the three force density components can be expressed as

$$\begin{aligned} f_{n,s} &\propto \left[\sum_v cos\left(p\omega t \mp vp\theta\right)\right]^2 \\ &= \sum_v cos\left(2p\omega t \mp 2vp\theta\right) \end{aligned} \tag{3.24}$$

$$\begin{aligned} f_{n,m} &\propto \left[\sum_u cos\left(up\omega t - up\theta\right)\right]^2 \\ &= \sum_u cos\left(2up\omega t - 2up\theta\right) \end{aligned} \tag{3.25}$$

$$\begin{aligned} f_{n,sm} &\propto \sum_v \sum_u cos\left(p\omega t \mp vp\theta\right) cos\left(up\omega t - up\theta\right) \\ &= \sum_v \sum_u cos\left[(1 \mp u)p\omega t \pm (u \mp v)p\theta\right] \end{aligned} \tag{3.26}$$

where $v = 6k \pm 1$ and $u = 2k - 1$. Mathematically, the square of a sum results in a function of two summations. However, neglecting the interaction of different harmonics, e.g. cross coupling among harmonics, the above expressions are obtained. In Fig. 3.6, 3.8 and 3.10 the force density are presented in time/space for PM excitation only, stator excitation only and normal operation, respectively. In Fig. 3.7, 3.9 and 3.11 the force density for the three cases are presented with frequency/wave diagrams obtained from 2D FFT. Comparing the data with (3.25), (3.26) and (3.27) it is clear that the harmonics present are the expected ones. Additionally, when the rotor and armature fields interact, the harmonic content is rich. The pure circumferential modes, located on the line crossing

the zero point, is the most dominating. As of before, the harmonics seen at $n = \pm 45$ with a frequency of $\omega t = 0$ result from interaction with the stator slots. As can be seen, harmonics as concentrated not only to the diagonal crossing circumferential order $n = 0$, but also to the diagonals crossing the circumferential orders $n = \pm 45$. These are also a result of the interaction with the stator slots.

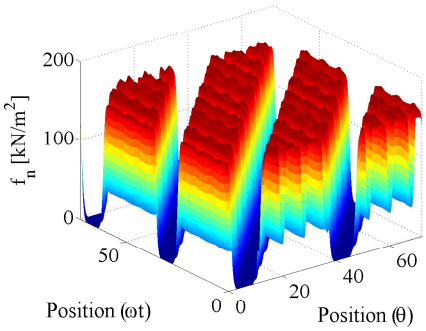

Figure 3.6 Radial force density density as a function of both time (ωt) and space (θ) with only PM excitation

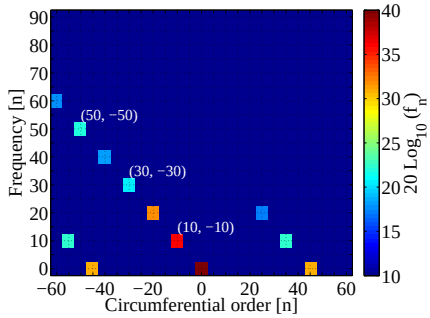

Figure 3.7 Frequency and mode number of the radial force density from PM excitation derived by 2D-FFT

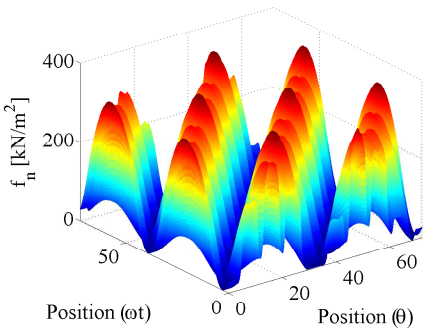

Figure 3.8 Radial force density density as a function of both time (ωt) and space (θ) with only stator excitation

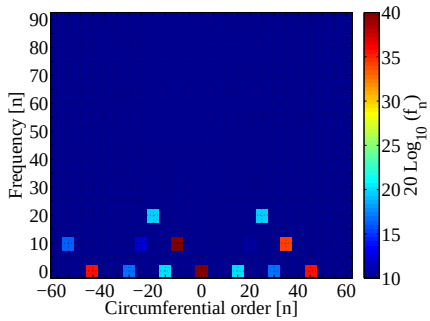

Figure 3.9 Frequency and mode number of the radial force density from stator excitation derived by 2D-FFT

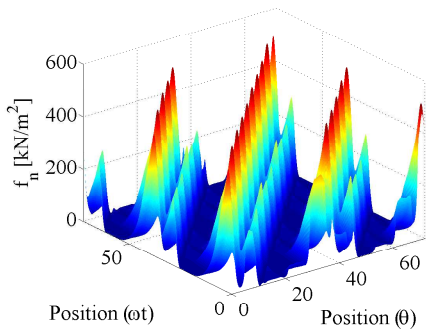

Figure 3.10 Radial force density density as a function of both time (ωt) and space (θ) with at normal load operation

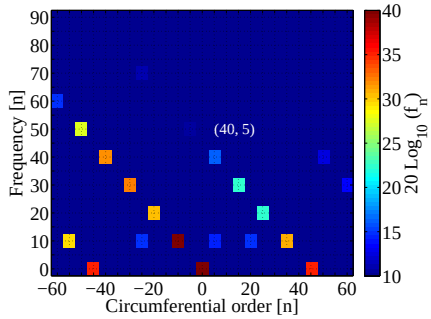

Figure 3.11 Frequency and mode number of the radial force density during normal load operation derived by 2D-FFT

The harmonic content in both the stator and the rotor is affecting the torque production in the machine. If modes in the MMF originated from the stator are of the same order as those from the rotor, torque will be produced. If two modes has the same frequency components a smooth and steady torque will be produced. However, if the frequencies of the modes with the same mode numbers differs, the torque generation will pulsate. This is a result of the difference in relative speed of which the modes propagate in time.

3.4 Radial and tangential components

In literature, usually the tangential component is neglected in the context of force density calculations for simplification purposes [1, 30, 38]. Neglecting the tangential component is only valid if the difference in magnitude between the two components is sufficiently large. If the permeability is significantly larger in the ferromagnetic core than in the airgap, the tangential component of the flux density across the boundary at the stator teeth is strongly suppressed.

Assuming that there is no surface current at the stator teeth, the tangential component of the magnetic field on both sides of the boundary where the airgap meets the teeth are the same, since the surface current can be expressed as

$$J_s = H_{1t} - H_{2t} \tag{3.27}$$

where H_{1t} and H_{2t} is magnetic field in tangential direction at the two sides of the boundary and J_s is the surface current on the boundary. As a result, the tangential component

of the flux density inside the stator teeth is significantly larger than in the airgap, due to the higher relative permeability. This can be explained as

$$H_{1t} = H_{2t} \rightarrow \frac{B_{1t}}{\mu_1} = \frac{B_{2t}}{\mu_2}. \tag{3.28}$$

Consequently, if the permeability is higher in the ferromagnetic material than in the airgap, so will the tangential component of the flux density also be. Additionally, Maxwell's equations and Gauss's theorem tells that the normal component of the flux density must be continuous across the boundary as a consequence of the law of conservation [30], [38]. With this in mind, it is understandable that the tangential component of the flux density is significantly lower than the normal component in the airgap at the boundary between airgap and stator teeth, which motivates the validity of ignoring the tangential component.

However, even zero tangential component at the boundary does not necessarily comply with flux density in the airgap consisting only of radial components, which might seem contradictory. But even though the transition of flux through the boundary at a tooth consists only of a radial component, flux does not only flow through surfaces at teeth facing the rotor, but also through surfaces facing adjacent teeth. Some of this flux is leakage and will not contribute to force density harmonics, but some will flow to or from the rotor. Consequently, the flux density across the air gap will consist of both tangential components as well as radial components, even though there is no tangential components at the boundary.

Consider a case, starting at the centerline of a stator tooth. For the flux density, it is reasonable that the radial component at the centerline of the tooth by far exceeds the tangential component, since the transition of flux from or to the tooth is of pure radial nature due to that the tooth and rotor are facing each other. However, as the angular position is changed from the centerline of a tooth towards a stator slot, conditions change and the magnitude of the tangential component is increased whereas the radial component is significantly decreased. This is partly a result of that the normal to the stator tooth is no longer facing the rotor, but instead the next stator tooth, giving a normal direction which is now parallel to the tangential direction of the rotor surface. Consequently, the radial and tangential flux density components suffer from irregularities occurring during every transition from stator tooth to stator slot or vice versa, seen from the angular position in the airgap [39].

In figure 3.12 the radial and tangential components of the flux density are presented, the data is obtained from FEM-simulations without stator excitation and is solely a result of the magnetization from the PMs. It is geometrically obtained in the center of the airgap. The location in the airgap at which the flux density is observed is of interest

as it influences the characteristics of especially the tangential component. Closer to the stator the tangential component has more distinct peaks with higher magnitude and less duration. In the figure, one can clearly see discontinuities in both the radial and tangential components, as previously discussed. The irregularities are initialized as the stator contour facing the rotor are changed from stator tooth to stator slot.

Studying figure 3.13, illustrating a time instance of the same FEM-simulation, showing a region around the airgap and the flux lines, one can see the curvature of the flux lines and the concentration of flux in the stator teeth. In the airgap in the centerline of the figure, both the radial and tangential components of the flux density are zero correlating to an angular position of 100 electrical degrees in Fig. 3.12. In the teeth to the left and to the right of the centerline the flux flows from the rotor to the stator, and from the stator to the rotor, respectively. This is indicated by the black arrows pointing in the direction of the flow.

In the figure, a majority of the flux is exciting the tooth to the right of the centerline in the lower rightmost corner, corresponding to an angular position of roughly 65 degrees in figure 3.12, where the tangential component is strongly negative. In the same way, a majority of the flux is entering the tooth to the left of the centerline in the lower leftmost corner, corresponding to an angular position of roughly 135 degrees in figure 3.12, where the tangential component, as well, is strongly negative.

With analogy to circuit theory, the magnetic flux follows the path of least reluctance, as previously discussed. Changes to the reluctance as a consequence of mechanical rotation of the rotor or magnetic saturation will affect the flux density and hence the resulting forces acting on the stator. From Fig. 3.12 and 3.13 it is also reasonable to assume that the teeth dimensioning heavily influences the harmonic content of the airgap flux density. In Chapter 6 the slotting and the dimensioning of the stator teeth influence on the airgap flux density is investigated.

To conclude, the accuracy of the simplification of neglecting the tangential component depends to a large extent on the objectives of the study and the point of data collection, i.e. the location in the airgap where the data is collected (in FEM-simulations). If the data is collected in the vicinity of the stator rim, in opposition to collecting the data close to the rotor surface, the tangential component might not be negligible. In the presented data obtained from FEM-simulations in the continuation of the thesis, both the radial and tangential components are included. However, in Section 3.3 only the radial component is considered for simplification purpose when the analytical expressions are derived for the force density harmonics.

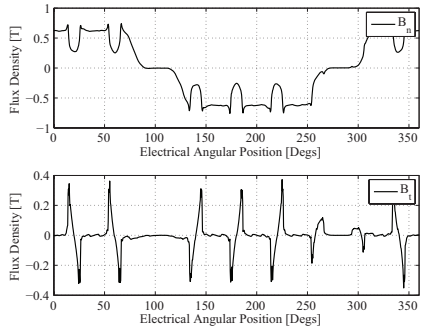

Figure 3.12 Radial and tangential flux densities as functions of electrical angular position in the airgap. The data is obtained from generator-mode FEM-simulations

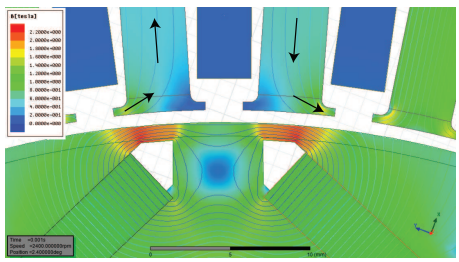

Figure 3.13 Flux linkage distribution and flux lines without stator excitation

3.5 Stator dynamic response and radiated sound power

Without any knowledge of the dynamic response of the stator and the radiation efficiency, the ability to draw any conclusions from the force density is limited. Simply because, in such case, it is unknown how the system responds to the force density harmonics.

As noise and vibrations appear, these can be quantified as either forced vibrations or resonances. Forced vibrations occur continuously for each and every force density harmonic as its magnitude, frequency and mode number forces the stator to deform. Resonance, on the other hand, occurs when the stator eigenfrequency coincides which the excitation frequency of the force density component, simultaneously as the vibrational order of that eigenfrequency equals the vibrational mode number of the excitation force. For instance, if the stator has an eigenfrequency of 1000 Hz with a corresponding mode number of 5, a resonance will occur if it is excited by a force with a frequency in the vicinity of 1000 Hz and a vibrational mode number of 5 [40, 41].

As discussed in Section 3.1, the low order circumferential modes are of highest

importance from a noise and vibration perspective. For pure circumferential orders, the mechanical deflection Δd of the stator yoke is inverse proportional to the mode number to the power of four [1], for convenience presented here again.

$$\Delta d \propto \frac{1}{N^4}. \tag{3.29}$$

As discussed by Dupont et al. [41] the low orders are acoustically significant because of the high radiation efficiency. In other words, excitation of these modes will transform mechanical movement into acoustic noise very efficiently.

Free vibration analysis can be used to analyse the mode shapes and the natural frequencies of any object. In this case, the stator is of interest and the parts that are included is the stator teeth and yoke. One can argue the importance of the copper windings in this type of analysis. However, the initial approach is to use only the aforementioned objects. All objects are considered to be fully bounded, meaning that they are acting as one piece and without any friction.

In ANSYS Workbench, the Modal solver is used to study free vibrations. The finite element method calculates deflection and displacement in every node of the mesh. Consequently, a finer mesh gives a more detailed result due to higher resolution.

The solving procedure is to solve the non-linear vibration equation

$$M\ddot{x}(t) + C\dot{x}(t) + Kx(t) = F(t) \tag{3.30}$$

where M, C and K are the mass, damping and stiffness characteristics and F is the load vector. In the following free vibration analysis the damping and the load vector are set to zero. In Fig. 3.14, 3.15, 3.16, 3.17, 3.18 and 3.19 the first six circumferential modes are presented for the machine. In Table 3.1 the mode shapes are summarized with there corresponding eigenfrequencies. With the harmonic content of the force density presented in Fig. 3.11 one can conclude that a potentially problematic force density harmonic is $n = 5$ rotating at 40 times the rotational speed. At a rotational speed of roughly 5500 r/min the eigenfrequency of the fifth mode coincides with the excitation frequency and resonance occurs. However, at other frequencies than the eigenfrequency of the fifth mode shape, emitted noise due to forced vibrations are likely to occur due to the high radiation efficiency of the low circumferential order. In a similar manner, the force density harmonic with frequency 10 times the rotational speed, with a circumferential order of 5 is likely to cause significant vibrations as well.

Table 3.1 Vibrational orders and corresponding eigenfrequencies

Mode shape $[n]$	Frequency $[Hz]$
1^{st}	0
2^{nd}	1150
3^{rd}	1611
4^{th}	2924
5^{th}	3686
6^{th}	4243

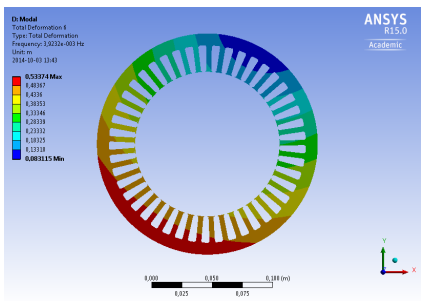

Figure 3.14 Stator deformation mode 1

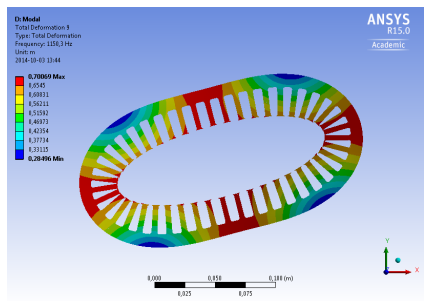

Figure 3.15 Stator deformation mode 2

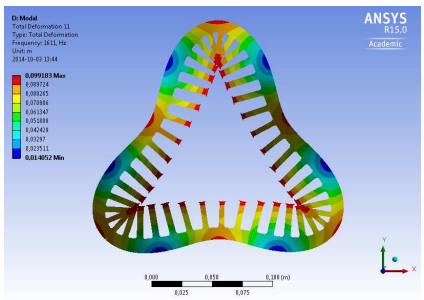

Figure 3.16 Stator deformation mode 3

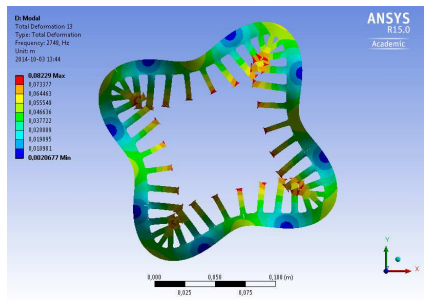

Figure 3.17 Stator deformation mode 4

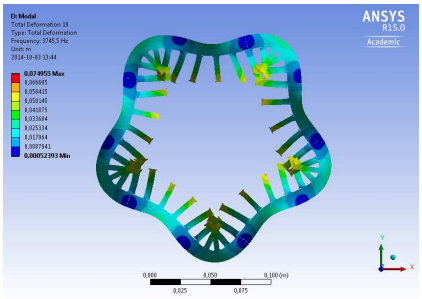

Figure 3.18 Stator deformation mode 5

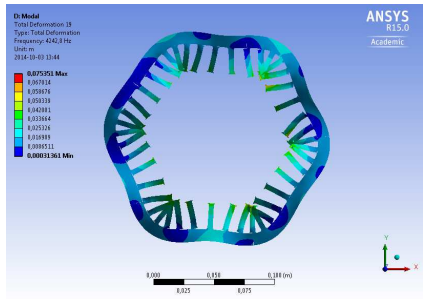

Figure 3.19 Stator deformation mode 6

Chapter 4

Experimental setup

Experimental testing is used both as a complement to simulations and to study phenomena that are either too uncertain or too complex to model. In this case, for instance the radiated noise from the electrical machine. Despite the considerable effort required to design, manufacture and install a complete test-rig, it is considered valuable from a scientific perspective, hence motivating the effort. Additionally, the intention is to continue the utilization of the experimental testing equipment in future work, further motivating the efforts. Evaluating concepts and ideas with practical implementations and experimental testing strengthens the scientific results while adding educational benefits.

4.1 Testing equipment

An electrical rear axle drive (ERAD) unit is used in the experimental testing. The ERAD consists of a three-phase PMSM incorporated with a speed reducer, differential and clutch. The electric drive unit is presented in Fig. 4.1 and illustrated in Fig. 4.2. The unit is currently in production of a mass-produced hybrid electric vehicle.

The drive unit is mounted in a subframe which is rigidly attached to the machine bed. The attachment of the drive unit to the subframe has not be altered and is therefore the same as for the intended application.

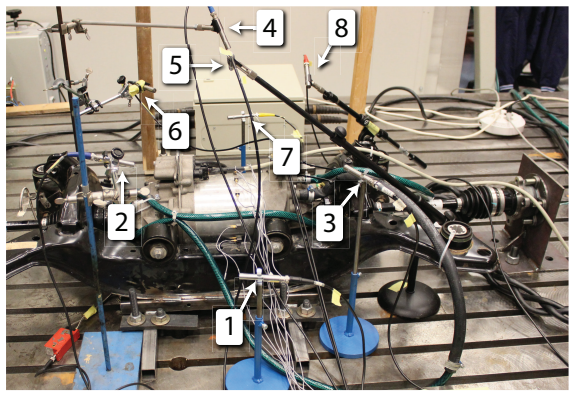

Figure 4.1 Experimental setup with PMSM and instrumentation for sound and vibration measurements. The PMSM is mounted in a subframe and attached to the load machine to the left.

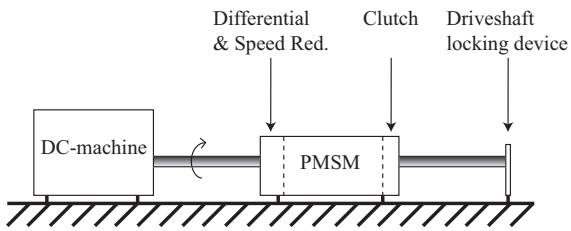

Figure 4.2 Illustration of the electrical rear axle drive unit installation

4.1.1 Inverter and electrical machine

A three-phase two-level inverter was constructed. It is fed by a 220 V DC voltage supply and controlled via a real-time interface. The real-time interface allows for complete access and control of the machine and the load at all times. The technical data of the PMSM is presented in Table 4.1. The technical data of the IGBT module used in the experimental testing is presented in Table 4.2. The inverter loss calculations are based on the IGBT module presented in Table 4.3, which is a reasonably sized module for the intended application.

In Fig. 4.3 the stator and rotor geometries are presented for the used PMSM. In the photograph, a single lamination sheet is seen of both the rotor and the stator. In Fig. 4.4 the stator geometry is presented, including windings and the three-phase winding connection.

Table 4.1 PMSM parameters

Variable	Value	Unit
Number of pole pairs	5	n
Number of slots	45	n
Number of parallel branches	8	n
Yoke outer radius	90.0	mm
Yoke inner radius	80.7	mm
Stator inner radius	59.0	mm
Rotor outer radius	58.2	mm
Airgap length	0.8	mm
Active length	140	mm
PM material coercivity	820	kA/m
Iron material	M270-35A	-
Winding type	Double layer	-
Iron Material	M270-35A	-
DC-voltage*	220	V
Peak phase current*	150	A
Base speed**	3700	r/min
Peak torque**	61	Nm

* Values used in this work

** With $V_{dc} = 220V$ and $i_{ph,peak} = 150A$

Table 4.2 Technical Data for IGBT Module used in the experimental testing (SKM800GA125D)

Variable	Value	Unit
E_{on} @ 600V, 600A	88	mJ
E_{off} @ 600V, 600A	48	mJ
E_{rr} @ 600V, 600A	28	mJ
$R_{on,IGBT}$	3.83	$m\Omega$
$R_{on,diode}$	1.7	$m\Omega$
$V_{f,IGBT}$	1.7	V
$V_{f,diode}$	0.85	V

Table 4.3 Technical Data for IGBT Module used in theoretical calculations (FZ600R17KE4)

Variable	Value	Unit
E_{on} @ 300V, 400A	4.2	mJ
E_{off} @ 300V, 400A	16	mJ
E_{rr} @ 300V, 400A	7.25	mJ
$R_{on,IGBT}$	1.0	$m\Omega$
$R_{on,diode}$	1.4	$m\Omega$
$V_{f,IGBT}$	0.8	V
$V_{f,diode}$	0.9	V

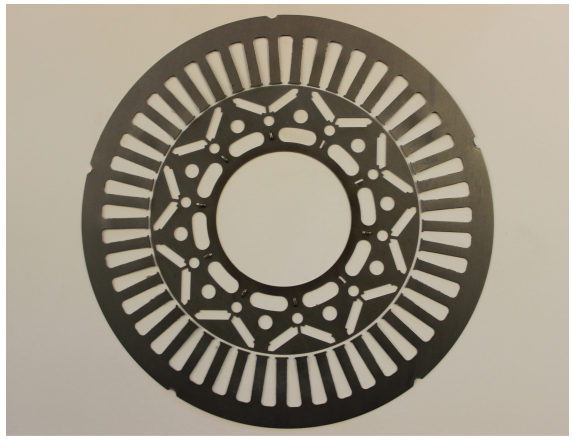

Figure 4.3 Single lamination sheets of the rotor and the stator geometries of the PMSM used in the work presented. The machine is parameterized in Table 4.1.

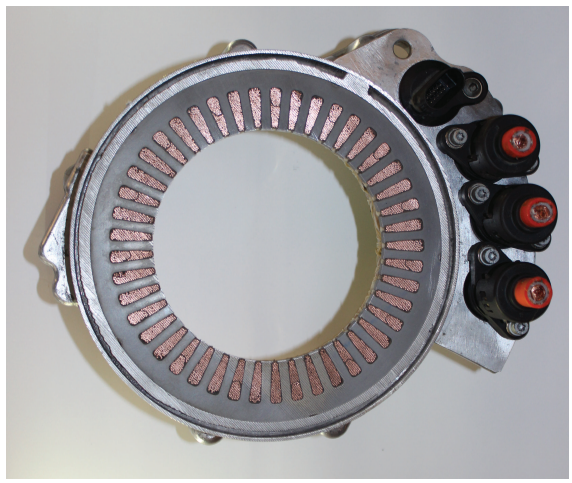

Figure 4.4 Stator geometry of the used machine including windings. To the right, the three-phase winding connection is seen.

4.1.2 Noise measurements

For the noise measurements, eight 0.5" microphones with a nominal sensitivity of 50 mV/Pa were evenly distributed in order to obtain a robust global measure of the radiated sound around the PMSM drive with coordinates according to Table 4.4. The distance between the surface of the electric drive unit to each of the microphones ensured avoidance of measuring in the acoustic near-field for the frequency range of interest, which

is in the region from 0 Hz to roughly 16 kHz. For the vibrational measurements, nine 5 gram uniaxial accelerometers were glued, with a very thin layer of cyanoacrylate in order to reduce the influence of the accelerometer-adhesive resonance, evenly along the axial center line on the upper arch of the cooling jacket of the stator. Microphones and accelerometers can be seen in Fig. 4.1.

In order to reduce the impact of background noise, an acoustic box, seen in Fig. 4.5, with sides consisting of a 22 mm medium density fibreboard (MDF) in combination with 30 mm foam was constructed. A similar box was also constructed for the brake machine. As Fig. 4.6 reveals, the spectrum contains less noise up to about 10 kHz with the acoustic box applied. Note that the x-axis is in a logarithmic scale, hence the orders are curved instead of straight as they are with linear scaling.

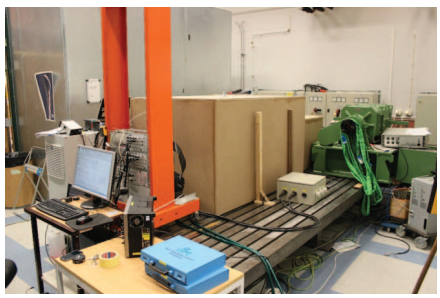

Figure 4.5 Acoustic box made of 22 mm MDF for background noise reduction positioned around the test object and real-time control system (left).

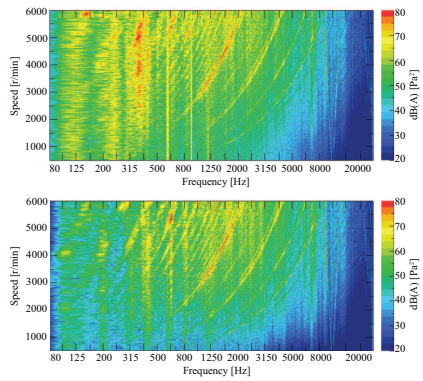

Figure 4.6 Autopower noise spectrum without (upper) and with (lower) acoustic box for SPWM, at 30 Nm, and $f_s = 10$ kHz.

Table 4.4 Microphone Coordinates

Mic. Pos.	X (m)	Y (m)	Z (m)
1	0	0.41	0.27
2	0.23	0.22	0.40
3	-0.21	0.23	0.40
4	0	0.13	0.52
5	0	-0.12	0.53
6	-0.21	-0.23	0.40
7	0	-0.38	0.27
8	-0.22	-0.21	0.41

4.1.3 Instrumentation

The instrumentation that is used in the experimental testing is presented in Table 4.5. A 40 channel data acquisition system is used primarily for acquisition of noise and vibration data whereas the Lecroy oscilloscope with AP011 probes are used only for current measurements. Two different types of accelerometers are used. The uniaxial ones are mounted on the stator cooling jacket measuring radial accelerations, whereas the triaxial accelerometers are mounted on the subframe to measure blocked forces.

Table 4.5 Instrumentation used in experimental testing

Item	Instrument	Comment
1	LMS Scadas Mobile 40 channel acquisition system	Used for NVH measurements
2	Lecroy Wavesurfer 24MXs-B	Used for current measurements
3	0.5 inch B&K G.R.A.S microphones	-
4	Uniaxial B&K 4507B accelerometers	Mounted on stator housing
5	Triaxial 4524B accelerometers	Mounted on subframe
6	Lecroy AP011 Current probe	Current measurement probe
7	Lecroy AP032 Differential probe	Voltage differential measurement probe
8	dSpace RTI1006	Control system

4.2 Test procedures

Both steady state and transient analyses are done. The steady state analysis is suitable for data collection of electrical quantities such as phase current, whereas transient analysis is suitable for noise and vibration measurements. During the transient analyses, the rotational speed is swept from 500 to 7500 r/min over a time period of 60 seconds. The data collection is handled in parallel with separate analog to digital conversion for each of the 40 channels of the LMS Scadas acquisition system with a sampling frequency of 22 kHz.

Chapter 5

Finite element modelling

Finite element modelling (FEM) is used to solve complex electromagnetic boundary value problems, i.e. problems defined by differential equations subjected to constraints. As a numerical technique, the obtained solutions are approximate and to a certain level erroneous. The accuracy of the solution depends on the resolution of the finite element model. For instance, the resolution can be defined by the mesh refinements of the geometrical representation of the electrical machine [42]. Moreover, the problems are solved in the time-domain, hence the time resolution is another variable that influences the results.

An evaluation of the FEM-model is of importance for many reasons. To grasp the limitations in FEM as a method, the outcome from the calculations needs to be validated with measurements. Without any knowledge of the accuracy of the solution, the ability to draw any conclusions from the FEM are limited, to say the least. Furthermore, an understanding for the sensitivity of the solution accuracy with respect to solver defined parameters is of interest as well. For instance, geometry detailing, meshing and time resolution will greatly affect the computational time. Instead of consistently maximizing the computational time by refining the mesh and the simulation time stepping, a more prominent engineering method would be to study each parameters influence on the accuracy and select a setup that will generate an accuracy that is in line with what is needed for the targeted investigation. Doing so, a sufficiently adequate result will be obtained while the simulation time is kept small.

In this chapter, the 2D FEM-model is described and parameterized. The finite element modelling is described and the resolution is studied by the use of zero cell size extrapolation and the model is evaluated with measured data. Thereafter, an approach to enable voltage excited finite element modelling is presented. Lastly, multi-physic simulations are presented, which is used when coupling electromagnetic forces to vibrations on

the stator. The simulation software used is ANSYS with the engineering suites Maxwell and Mechanical.

5.1 2D ANSYS Maxwell model

5.1.1 Machine parameter identification

The 2D FEM-model is validated by comparing data from the FEM-model to measurements. The parameters that are verified are the PM flux (Ψ_m), the dq-inductances (L_d) and (L_q) and the stator resistance (R_s). The verification is based on a series of measurements where the machine is operated in generator mode. Both open-circuit and loaded generator mode measurements are done.

Firstly, the DC component of the stator resistance is estimated. Thereafter, open-circuit measurements of line-to-line voltage are done to estimate the PM flux component and lastly loaded generator mode is used to estimate the inductances. The DC component of the stator resistance is determined by feeding the machine with a given line-line current whereas the voltage drop over the two phases are measured. The measurement includes both machine resistance and the resistance in the three-phase cabling connecting the machine to the inverter.

The PM flux component (Ψ_m) is estimated by operating the machine in generator mode. From the theory in Section 2.1.1, the stator voltage in the quadrature direction can be expressed as

$$u_q = j\omega\Psi_m \tag{5.1}$$

at open-circuit, whereas the d-axis voltage is zero. The PM flux component is extracted and presented in Table 5.1 together with the rotational speed for the four cases. With a coercivity of the PM material of 820 kA/m the flux constant of 49.30 mWb is obtained from FEM-simulations when the machine is operated in no-load.

Table 5.1 Estimated flux linkage from no-load operations

#	f_0 [Hz]	ω_m [r/min]	$\hat{\Psi}_m$ [mWb]
1	18.7	224.4	47.85
2	38.4	460.8	47.82
3	56.0	672.0	48.00
4	73.6	883.2	49.48

The dq-inductances are estimated based on measurements in loaded generator

operation where the three phases are connected to a three-phase resistive load unit. The line-to-line voltages, phase currents, rotational speed as well as the rotor position are measured and the dq-inductances are calculated as

$$L_d = \frac{u_q - R_s i_q - \omega \Psi_m}{\omega i_d} \tag{5.2}$$

$$L_q = -\frac{u_d - R_s i_d}{\omega i_q}. \tag{5.3}$$

The inductances are estimated for four rotational speeds where the current is determined by the voltage drop over the resistive load unit caused by the induced voltage of the machine. Note that both i_d and i_q are negative due to the generator operation mode and that the four cases presented differs from the four cases used previously to determine the PM flux component. The estimated inductances are presented in Table 5.2 where they are compared to the values obtained from FEM-simulations. As can be seen, there is a deviation in L_d whereas the measurements coincides well with FEM-simulations for L_q. Additionally, the dq-current is considered low in the three first cases which is not representative for the analysis done further on in the thesis. Therefore, the results are considered sufficiently accurate.

Table 5.2 Comparison of L_d and L_q between FEM-simulations and measurements

			Measurements			Deviation from FEM	
#	ω_m $[r/min]$	i_d $[A]$	i_q $[A]$	L_d $[\mu H]$	L_q $[\mu H]$	ΔL_d [%]	ΔL_q [%]
1	923.1	-9.3	-28.8	281.3	438.8	+56.5	+3.8
2	1846.2	-31.6	-50.8	220.9	435.0	+23.0	+5.0
3	2823.5	-58.7	-64.8	212.4	427.8	+19.1	+4.5
4	3692.3	-84.2	-71.8	206.4	417.7	+15.9	+2.7

5.1.2 Harmonics in induced voltage

The induced voltage is studied in open-circuit generator operation where the FEM results are compared with measurements at a rotational speed of 4000 r/min. For the FEM-simulations a time-step of 10 μs is used, in accordance with the findings in the following sections. The measurements from the experimental testing are performed with a sampling frequency of 2.5 MHz. This analysis aims to evaluate the magnitude of the fundamental component and harmonics of the induced voltage and indirectly the flux linkage. Parameters affecting the result for this analysis, and what might cause deviations, are related to geometry and material properties. Minor faults in the FEM-model

geometry in relation to the physical machine will of course contribute to deviations between the two. In the same way, unknown imperfections in the physical machine will of course affect the comparison as well.

In Fig. 5.1 one electrical period is presented for both the measurement and the FEM-simulation. No corrections are made in neither magnitude nor time in terms of scaling, except for a first order low pass filtering of the measured signal to suppress measurement noise. As can be seen in the figure, the data correlates reasonably well. Considering deviations in the harmonics, selecting the FEM-simulation as reference, the fundamental component of the measurement differs by +2.47 percent whereas the higher harmonics does not correlate as well. In Table 5.3 deviations of the low order harmonics are presented, with the FEM as reference. Based on the presented data, one can conclude that the fundamental component is well represented in the FEM-model whereas the low order harmonics in the voltage are compromised to some extend.

Based on the data presented in this section as well as the previous section, one can confirm the functionality of the 2D-FEM model. The low order harmonics, which are not very well represented in the FEM-simulations, do not affect the continuation of the thesis hence these are considered to be of secondary importance.

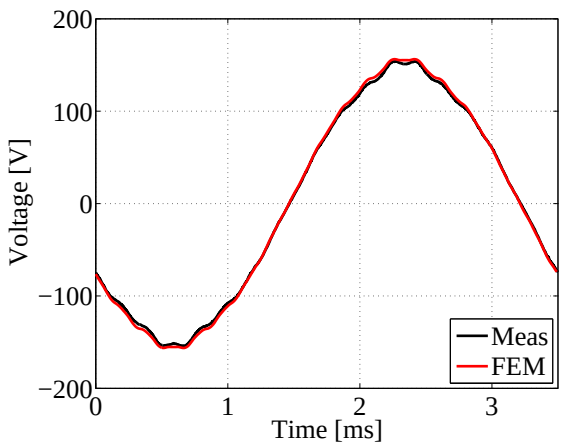

Figure 5.1 Comparison of induced line-to-line voltage in generator mode at 4000 r/min

Table 5.3 Comparison of line-to-line voltage between FEM-simulations and measurements

Harmonic [n]	FEM [V]	Measurement [V]	Deviation in percent [%]
1	149.7	153.4	+2.47
5	2.806	2.049	-26.98
7	1.809	1.507	-16.69
11	0.285	0.243	-14.74
13	0.295	0.149	-49.49
17	1.548	1.127	-27.20
19	1.306	1.332	+1.2

5.2 Sensitivity of Maxwell 2D-model

In this section the 2D Maxwell model is further evaluated and sensitivity to mesh size and time step size is investigated. The evaluation is done accordingly. Firstly, parameter sensitivity analyses of the cell sizing are performed followed by a sensitivity analysis of the time step size. The aim is to gain understanding in how these affect the results and to properly motivate the selection used in the following analyses.

The size of the triangular mesh is an important parameter, as previously discussed. The number of elements and the number of computational nodes greatly impacts the resolution of the analyzed object. In contrast to resolution is computational time. It is reasonable that the roughness of the mesh should be defined primarily by the objective of the simulation, i.e. the level of detailing required, in order to obtain a computational time as modest as possible.

Considering the fictive case of performing a FEM-simulation with infinite mesh resolution, i.e. zero cell size, one could use the results to easily quantify deviations resulting from any finite mesh size. The resulting infinite simulation time for such a simulation is however troublesome, hence zero cell size results can only be achieved by extrapolation of results based on finite mesh-sized simulations. In the same manner, zero time step results can be obtained by extrapolation of finite time step results.

The sensitivity analysis is focused around the induced voltage and the airgap flux density. The selection of the induced voltage as a parameter of interest is because of its direct relation to flux linkage. The interest in the airgap flux density is related to the continuation of the thesis, where its influence on force density is of interest. As discussed previously in Chapter 3, radial and tangential forces acting on the stator can be calculated from the airgap flux density.

Firstly, a sensitivity analysis on cell size is performed, followed by a sensitivity

analysis of the time step size. The analysis approach is the same for both cases, and are therefore only covered for the cell size analysis case.

5.2.1 Sensitivity analysis of mesh size

Based on a series of simulations where the cell size relation are chosen accordingly

$$\frac{h_i}{h_{i+1}} = \frac{h_{i+1}}{h_{i+2}} \tag{5.4}$$

where h_i, h_{i+1} and h_{i+2} are the cell sizes for simulation i, $i+1$ and $i+2$, the order of convergence can be estimated as

$$p = \frac{ln\left(\frac{I(h_i)-I(h_{i+1})}{I(h_{i+1})-I(h_{i+2})}\right)}{ln\left(\frac{h_i}{h_{i+1}}\right)} \tag{5.5}$$

where $I(h_i)$ is the outcome from the FEM-simulation and h_i is the cell size of that simulation [42].

The parameters dependency on cell size can, more or less accurately, be described analytically by Taylor expansion. Assuming that two components is sufficient to describe a variables dependency on for instance the cell size, the following analytical expression can be used

$$f(h_i) = f_0 + f_1 h_i^p \tag{5.6}$$

where $f(h_i)$ is the results based on the mesh size h_i, f_p is a scaling factor and p is the order of convergence. In this representation, f_0 equals the value at zero cell size since the second term goes to zero as h is decreased. If the assumed decomposition is not representative enough, it can be extended with more components to achieve a more accurate representation. Using a simulation series of minimum three different cell sizes the unknown coefficients f_0 and f_1 can be calculated by defining the problem as

$$\begin{bmatrix} f(h_1) \\ f(h_2) \\ \vdots \\ f(h_n) \end{bmatrix} = \begin{bmatrix} 1 & h_1^p \\ 1 & h_2^p \\ \vdots & \vdots \\ 1 & h_n^p \end{bmatrix} \begin{bmatrix} f_0 \\ f_1 \end{bmatrix} \tag{5.7}$$

and solved for $[f_0 \ f_1]^T$ by matrix algebra using the pre-calculated convergence, according to (5.5). Note that it is not evident that a convergence can be established based on the methodology presented and the parameter variations selected. For instance, for a parameter that is not correlated with the variables that are changed, it is very unlikely that a converge can be established.

The cell size analysis is focused on the cell size of the outer part of the rotor, the stator teeth tips and the airgap, keeping the cell size of the remaining parts of the stator and rotor fixed. The analysed cases are presented in Table 5.4 where *Rotor2* is the outer part of the rotor, i.e. the surface of the rotor with a depth of 0.87 mm, facing the airgap.

Table 5.4 Cell sizes used for zero cell size analysis, in [mm]

Case	Stator	Windings	PM	Rotor	Rotor2	Airgap	Stator rims	Cells
1	3	1	1	1	0.125	0.125	0.125	78698
2	3	1	1	1	0.25	0.25	0.25	37616
3	3	1	1	1	0.5	0.5	0.5	26869

In Fig. 5.2 and 5.3 the induced voltage and the radial airgap flux density are presented, respectively. The flux density is studied 0.2 mm from the stator teeth tips, in the 0.8 mm wide airgap. For the flux density, the data is collected in one time instance, hence the data represent the distribution in space, covering one electrical period. As can be seen, the flux density is of reasonable magnitude considering the level of flux in relation to material saturation properties. Note that the curvature is symmetric and that the nine slots for one electrical period can be seen, centralized around roughly [20 60 100 140 180 220 260 300 340] electrical degrees in Fig. 5.3. The spikes appearing in the radial flux density occurs in the changeover from stator tooth to stator slot, as previously discussed in Section 3.2.

In Fig. 5.4 and 5.5 are the extrapolation of the fundamental component and the 9^{th} harmonic of the radial flux density presented, respectively. The solid lines represents the extrapolation and the red circles indicates the results from the FEM-simulations. The errors are calculated as

$$e(h) = 100 \times \frac{x_0 - \hat{x}_0}{x_0} \tag{5.8}$$

where x_0 is the final value of the extrapolation, denoted f_0 in (5.6), and $\hat{x}_0$ is the extrapolation as a function of h, denoted $f(h_i)$ in (5.6).

From the data, a few important conclusions can be drawn. The flux density is clearly correlated with the mesh size in the region around the airgap, which is expected. Also, the proposed Taylor expansion presented in (5.6) is sufficient to express the trajectory. Moreover, the error for both are within 0.4 percent for the three given cases, which is considered small. In order to achieve significant improvements in absolute values, the additional mesh size refinements required would be substantial. To conclude, the coarsest of the three cases are considered fine enough to generate sufficiently adequate results and will be used in the continuation of the work.

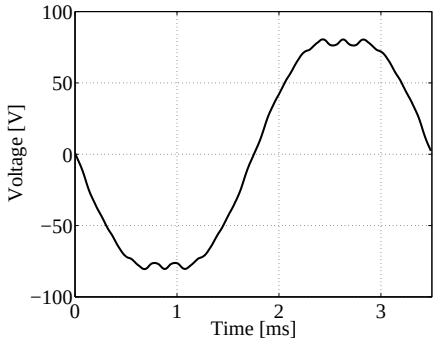

Figure 5.2 Induced voltage from FEM-simulations at generator operation at 4000 r/min

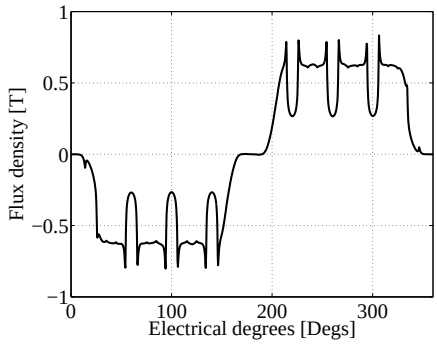

Figure 5.3 Radial airgap flux density from FEM-simulations at generator operation at 4000 r/min

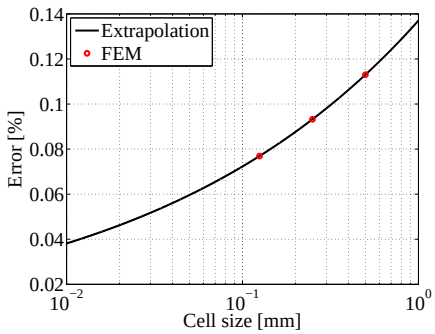

Figure 5.4 Extrapolation towards zero cell size of the fundamental component of airgap flux density at generator operation at 4000 r/min

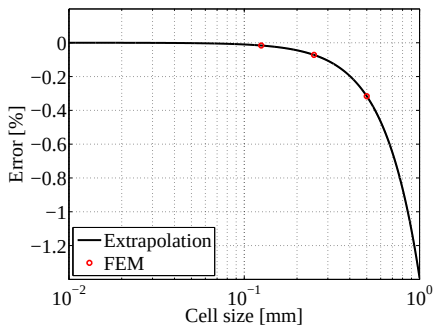

Figure 5.5 Extrapolation towards zero cell size of the 9^{th} harmonic of the radial airgap flux density at generator operation at 4000 r/min

5.2.2 Sensitivity analysis of time step size

For the time stepping five cases are studied. The step sizes selected are given in Table 5.5, all in conjunction with the interrelations presented in (5.4). Samples per electric period is based on a rotational speed of 4000 r/min. With a fundamental frequency of $1/0.0035 \simeq 286$ Hz, a resolution of up to $t_s = 40\mu s$ should be sufficient to catch the fundamental component very accurately, hence $0.0035/0.000040 = 87.5$ samples per fundamental period.

Table 5.5 Time step sizes used for the zero time step size analysis

Case	Time step [μs]	Samples per electric period [n]
1	2.5	1400
2	5	700
3	10	350
4	20	175
5	40	87.5

In Fig. 5.6, 5.7 and 5.8 the extrapolations for the fundamental component, the 5^{th} and the 7^{th} harmonics are presented, respectively. As can be seen, the fundamental component is correctly observed even for large step sizes, as $t_s = 40\mu s$. However, one can clearly see that the harmonics are subjected to substantial errors as the time resolution is too coarse.

Moreover, in Fig. 5.9 the same analysis is done for the core losses of the machine, including eddy current losses and hysteresis losses. As can be seen, simulation step times of less than $10\mu s$ is not significantly affecting the results.

For the purpose of the FEM-simulations, a time step size less than $10\mu s$ is considered excessive.

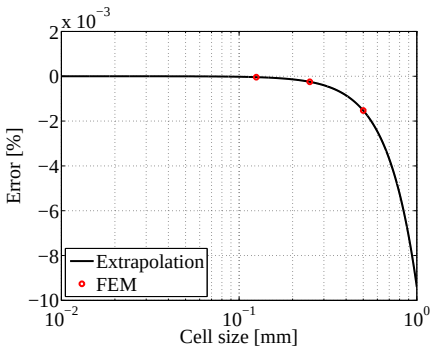

Figure 5.6 Extrapolation towards zero time step size of the fundamental component of the induced voltage at generator operation at 4000 r/min

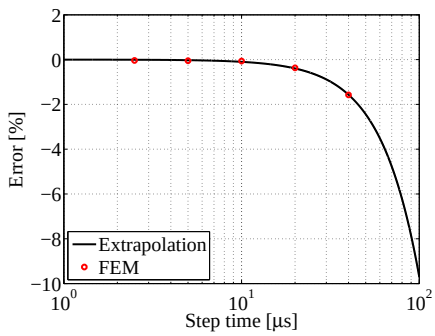

Figure 5.7 Extrapolation towards zero time step size of the 5^{th} harmonic of the induced voltage at generator operation at 4000 r/min

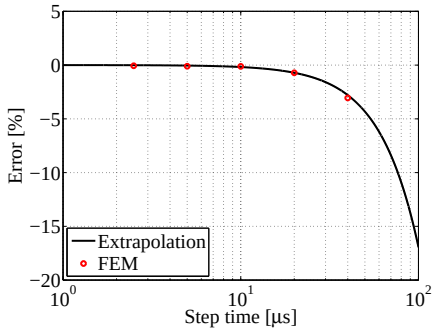

Figure 5.8 Extrapolation towards zero time step size of the 7^{th} harmonic of the induced voltage at generator operation at 4000 r/min

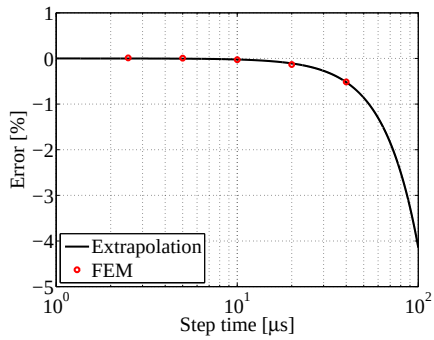

Figure 5.9 Extrapolation towards zero time step size of the core losses at generator operation at 4000 r/min

5.3 Voltage excited FE modelling in ANSYS Maxwell

In order to investigate high frequency harmonics in the airgap flux density and force density originating from the pulse width modulation, a methodology is developed enabling switched voltage source fed FEM-simulations. The objective is to investigate different modulation techniques influence and to verify differences in vibrations and radiated noise from the experimental testing. Normally, computational time restricts transient FEM analyses to cover only a few electrical periods in time. Obviously, minor errors in the initialization to such a simulation will cause offsets that are very unlikely to decay during the simulation time. Consequently, a method to overcome the issue with initialization errors in voltage excited FEM-simulations is needed. In principle, the method is based on a series of four simulations where the relatively long settling time of transients occurring due to initialization errors is used for detection and compensation.

In the case of voltage excited FEM-calculations a couple of items needs to be addressed in order to obtain an proper initialization, and hence adequate results. The items of high importance are:

1. Derivation of the induced voltage
2. Derivation of stator winding resistance and its usage
3. Elimination of initialization error in the phase current.

These three parts are described in the same order in the following sections. The PWM is implemented by deriving the switching patterns offline and the FEM-simulations

are executed in an open-loop fashion. Alternatively, a co-simulation with for instance ANSYS Simplorer can be used.

5.3.1 Derivation of induced voltage

Assuming perfect three-phase symmetry, only one phase needs to be considered, since the remaining two are solely phase shifted by 120 and 240 degrees, respectively. The induced voltage is needed when defining the voltage vectors to be applied in the voltage excited simulations. The applied voltage for phase A can be expressed as

$$u_a = R_s i_a + \frac{d\Psi_a}{dt} \tag{5.9}$$

where the derivative of the flux linkage equals the induced voltage [15]. Accordingly, the data obtained from the sinusoidally current excited FEM-simulation is the phase currents and the flux linkage, or the induced voltage. The time derivative definition used by ANSYS Maxwell is the s.c. backwards stepping [43], defined as

$$\frac{dx^{k+1}}{dt} = \frac{x^{k+1} - x^k}{\Delta t}. \tag{5.10}$$

Deriving the induced voltage with this definition introduces a phase error in the induced voltage, supplied by the FEM-program, that is proportional to the time step size. The phase error in electrical degrees can be expressed as

$$\tilde{\theta} = 180\frac{\Delta t}{t_0} \tag{5.11}$$

where Δt is the time step size and t_0 is the inverse of the fundamental frequency. As can be seen, the error is proportional to the time step size. Whether or not the induced voltage supplied by Maxwell is used, or if it is manually derived from the flux linkage, one should compensate for the phase error introduced by the derivative function for more accurate phase information.

As a result of the use of the backward stepping time derivative function, the initial induced voltage values in the FEM-calculation will be zero, naturally. If this is not considered, the phase current derivatives between the first simulation time $(t = 0)$ and the second $(t = \Delta t)$ will be faulty. As a result, the phase current will be subjected to an error. This can be explained by the stator equation expressing the dynamics in the voltage and current, as

$$\Delta t \begin{bmatrix} u_a - e_a \\ u_b - e_b \\ u_c - e_c \end{bmatrix} = \begin{bmatrix} L_{aa} & L_{ab} & L_{ac} \\ L_{ba} & L_{bb} & L_{bc} \\ L_{ca} & L_{cb} & L_{cc} \end{bmatrix} \begin{bmatrix} \Delta i_a \\ \Delta i_b \\ \Delta i_c \end{bmatrix} + R_s \begin{bmatrix} i_a \\ i_b \\ i_c \end{bmatrix} \tag{5.12}$$

$$\begin{bmatrix} \Delta i_a \\ \Delta i_b \\ \Delta i_c \end{bmatrix} = \begin{bmatrix} L_{aa} & L_{ab} & L_{ac} \\ L_{ba} & L_{bb} & L_{bc} \\ L_{ca} & L_{cb} & L_{cc} \end{bmatrix}^{-1} \left(\Delta t \begin{bmatrix} u_a - e_a \\ u_b - e_b \\ u_c - e_c \end{bmatrix} - R_s \begin{bmatrix} i_a \\ i_b \\ i_c \end{bmatrix} \right). \tag{5.13}$$

As can be seen, if the induced voltage at time step $t = 0$ are zero, the current derivatives will be severely enlarged. The result from this is phase currents that are erroneous in magnitude and possibly phase shifted. Either or, the airgap flux distribution will also be erroneous with consequences such as faulty electromagnetic torque production.

Both the issue with the phase shift due to time derivatives and due to zero induced voltage at the initial sampling point are linearly proportional to the sampling time. Consequently, the error introduced by both is decreased with a decrease in sampling time. However, an understanding of the issue and the use of suitable counter actions are more time efficient than decreasing the sampling time.

5.3.2 Stator winding resistance handling

The stator winding resistance is derived based on the copper losses as

$$R_s = \frac{P_{cu}}{3 i_{rms}^2}. \tag{5.14}$$

For the voltage excited simulations, the resistive losses is not calculated as in the current excited simulations. Instead of integrating the current density and using the conductivity of the material, the method used is the $i^2 \times R_s$. Consequently, the value of the stator winding resistance should be applied in the simulation settings in order to achieve power loss balance when using voltage excitation.

5.3.3 Initial phase current

When the simulations with different excitations are to be compared it is important that the fundamental components are comparable in magnitude and phase. If not, the simulations represent different operational points. When selecting initialization values for the phase currents in voltage excited simulations, it is reasonable to base these on values on the fundamental component of the current. However, due to harmonics, the fundamental values are unlikely to be an option that is correct in the sense that no transient behaviour arise. The correct values to be used as initial values for the phase current can be obtained in different ways.

As a result of the machine design, the flux linkage consists of a fundamental component and harmonics. If these harmonics are known in both magnitude and phase,

superposition can be used and the machine can be represented with several parallel systems, each with only one component. If this approach is used, the initial value for each of the parallel systems can be composed into a value that is correct for the machine as a whole. However, this approach requires unreasonable efforts, especially if the flux linkage is heavily distorted with a vast number of harmonics with significant magnitude.

An alternative option to detect the correct initialization values is to make use of the fact that the transients have a long settling time. If the fundamental current component is used as initialization, one can then study the outcome of the simulation and by fourier analysis detect the transient component in the current and add a correction term to cancel that frequency component. An obvious drawback is that two simulations are required. One simulation is required to detect the transients that are to be cancelled. Anyway, this solution is proposed due to its inherent simplicity and satisfying results.

5.3.4 Proposed simulation sequence in ANSYS Maxwell

The proposed simulation sequence used in this work can be seen in Table 5.6 and described more in detail in the following subsections. In all of the four steps, two electrical periods are simulated.

Table 5.6 Simulation sequence used in ANSYS Maxwell

Simulation step	Description
1	Current excitation (Sine)
2	Voltage excitation (Sine)
3	Voltage excitation (SPWM or DPWM)
4*	Voltage excitation (SPWM or DPWM, corrected)

* Correction is based on FEM-calculations of simulation # 3.

5.3.4.1 Step 1

Initially, a sinusoidal current excited simulation is performed at the operational point of interest. The phase current, flux linkage, rotor position and copper losses are extracted and used further on.

5.3.4.2 Step 2

Based on the obtained data from step 1, the first of the voltage excitations is defined. The phase error due to the time derivative of the flux linkage is compensated for and the

initial phase current values are based on the fundamental component of the phase current from step 1. In this simulation, the voltage is not switched but purely sinusoidal.

The outcome from this simulation will, most likely, not be without transients. Based on the current excited simulation (step 1), the magnitude of the fundamental component of the induced voltage and its phase angle is used (in addition to the resistive voltage drop) to determine the voltage references. However, note that the induced voltage during neither of the excitations are perfectly sinusoidal. The harmonics are partly due to space harmonics in the permeance as consequence of the variations in the airgap reluctance and the distribution of the windings in the stator.

In Fig. 5.10 the induced voltage is presented for sinusoidal current and voltage excitation (step 1 and 2). As can be seen, the induced voltage for neither of the cases is sinusoidal. Accordingly, using only the fundamental component (as in this case) the initialization will most likely be erroneous with transients in the current and torque as a result. However, this is compensated for in step 4. If the induced voltage for all three phases coincides with the values of the fundamental component, transients will not arise.

5.3.4.3 Step 3

From the previous simulation, the phase current, rotor position and flux linkage are used to define a new set of sinusoidal phase voltage reference vectors. This new set of sinusoidal references is modulated with a triangular wave to obtain the PWM patterns used in this step, being the first step with PWM input. The transients from step 2, which do not decay during the two electrical periods, will naturally be seen in the outcome from this step too. Which is why the forth step is required.

5.3.4.4 Step 4

Lastly, the obtained phase current, rotor position and flux linkage from step 3 are used to once again defining a new set of phase voltages to be applied. The new set of references is once again modulated with a triangular wave to obtain the PWM vectors used in this step. Additionally, the phase currents from step 3 are studied in the dq-reference frame and harmonics of interest are simply removed, by decomposing the data into its frequency components. From the adjusted phase currents (with unwanted harmonics removed) the very first samples are extracted and used as initialization values in this fourth simulation. Note that a prerequisite for this to work, is that the harmonics do not decay during the first two periods in step 3, which is very unlikely. However, if they do, the third step simply needs to be extended with an additional electrical period in order to obtain satisfying results.

In Fig. 5.11 the results of the initial current correction in this step can be seen. The data that is without correction is from step 3 and the data with correction is from this step, step 4. In the case without correction, one can clearly see a slowly varying component with a frequency equal the fundamental frequency.

In all the cases studied in this work, only the fundamental frequency has been removed from the dq-current. However, if additional harmonics are present that should not be, these can be excluded as well. Furthermore, in Fig. 5.12 and 5.13 the electromagnetic torque is presented with and without this correction. Clearly, a harmonic with the fundamental frequency can be seen in the non-compensated cases (step 3).

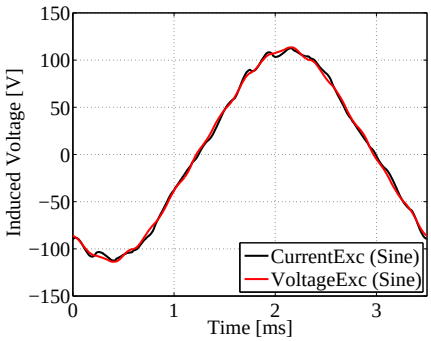

Figure 5.10 Comparison of induced voltage for phase A for sinusoidal current and voltage excitation.

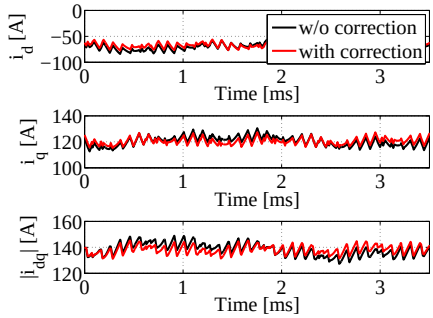

Figure 5.11 Comparison of dq-current between FEM-calculations with and without initial current value correction (step 3 in Table 5.6) for DPWM. The time corresponds to one electrical period.

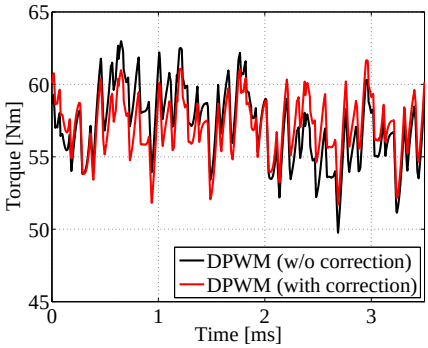

Figure 5.12 Electromagnetic torque over one electrical period visualizing the effects of the initial current correction for DPWM voltage excitation.

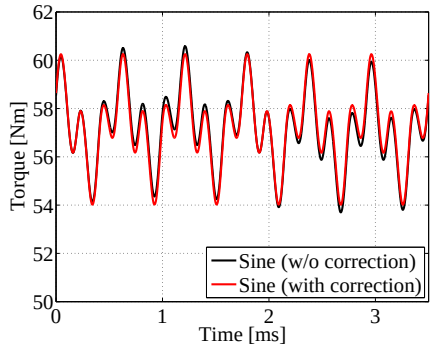

Figure 5.13 Electromagnetic torque over one electrical period visualizing the effects of the initial current correction for sinusoidal voltage excitation.

5.3.4.5 Remarks

The reason for the intermediate step (step 2) is to guarantee steady state in the operational point of interest. When step 2 is neglected, occasionally the initialization is too corrupted generating data that are beyond correction possibilities in the forth step.

The simulation setup in ANSYS Maxwell is partly tabulated in Table 5.7. Note that the simulation time is not fixed when PWM is used. An underlying time step size of 2 μs is used. However, whenever a switching of one of the phases occurs, two additional calculations are performed in the vicinity of the switching event. This is used to increase the accuracy and suppress errors that are due to a sparse simulation time stepping. Practically, this is done by controlling the time stepping in the simulation. An alternative solution would have been to use a fixed, but very dense, time stepping. Resultantly, such a case would require far more computational time.

Additionally, the simulation time and rotational speed of the machine are defined to coincide in an odd number of switching periods per fundamental period, in order to eliminate subharmonics in the phase current due to asynchronous PWM [44].

Table 5.7 ANSYS Maxwell Simulation Setup

Parameter	Value	Unit
f_0	0.0035^{-1}	Hz
T_{start}	0	μs
T_{step}*	2	μs
$T_{step,2}$**	10	ns
T_{stop}	7000	μs
Mesh nodes	52738	-

* Smaller time steps are taken in the vicinity of the switching events.

** Time step used in the vicinity of switching events.

5.4 ANSYS multi-physics simulations

5.4.1 Simulation setup

To perform multi-physical simulations the ANSYS Workbench Platform is used, enabling complex multi-physics analyses with drag-and-drop simplicity, illustrated in Fig. 5.14. As the figure illustrates, the interactions between the engineering suites in ANSYS are defined as forces originating from electromagnetic pressure acting on the stator teeth and vibrations on the stator yoke, due to mechanical displacements. For the structural analyses the geometrical description is inherent from ANSYS Maxwell and partly simplified by removal of parts with no or low importance. These analyses focuses on the stator deformation, hence stator teeth, rims and stator yoke are considered the most important parts.

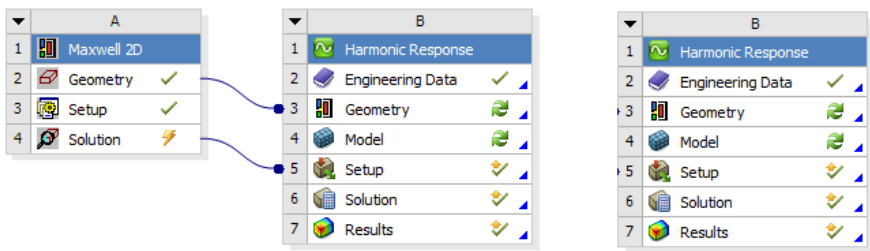

Figure 5.14 Illustration of acoustic analysis in ANSYS Workbench Platform

As one can expect, the material properties of the object are of high importance when performing structural analysis. The ones of particular interest are the Young's

Modulus, Poisson's ratio and the density. The Young's Modulus, also known as Elastic Modulus, measured in pressure $[Pa]$, is the ratio between stress and strain. The Poisson's ratio is used to define material behaviour when exposed to stress. If an object is compressed in one dimension it tends to expand in other dimensions, which is quantified by the Poisson's ratio. In Table 5.8 values used for these parameters are defined.

Table 5.8 Material properties for multi-physics analysis

Variable	Value	Unit
Young's Modulus	1.85×10^5	$[MPa]$
Poisson's Ratio	0.3	-
Density	7650	$\left[kg/m^3\right]$

Chapter 6

Theoretical analysis of electromagnetic flux and force density

The forces that are acting on the stator teeth, which generates deformations and consequently noise and vibrations, are closely related to the airgap flux density. For that reason, both flux density and force density are of particular interest to investigate. In the following sections these are investigated with focus on magnitude as well as frequency content in terms of spatial and temporal harmonics. This work is done with the machine presented in Chapter 4. In addition to the design presented in Chapter 4, the stator design is altered to study the impact and effects of slotting on both temporal and spatial harmonics. The alteration includes different slot opening widths, complete removal of the slots by bridging adjacent teeth, as well as the use of a significant increase in permeability to suppress the influence of magnetic saturation.

The selection of only altering the stator teeth tips opposed to the entire stator geometry is motivated by first and foremost the hypothesis of its significant influence on particular force density harmonics causing significant noise emissions. Furthermore, it is an isolated variable which simplifies the re-design without considerably effects on the overall performance of the machine. One should view the study as an investigation of the relation between the variable and harmonics of interest, rather than a search for an optimal design. As discussed in Section 3.1, the spatial orders of most significance from a NVH perspective are the lowest orders. Due to the geometric design of the machine, force density harmonics with spatial order of 0, 5 and 10 are the three lowest. Consequently, these are of highest significance.

The airgap flux density, considering only the radial component, can be decomposed into contributions from the stator excitation, $B_{ns}(\theta,t)$, and from the rotor permanent magnets, $B_{nm}(\theta,t)$. The resulting force density is presented here once more for the sake of clarity, it can be expressed as

$$f_n \simeq \frac{1}{2\mu_0}B_n^2 = \frac{1}{2\mu_0}\left[B_{n,s}+B_{n,m}\right]^2 \tag{6.1}$$

$$= \frac{1}{2\mu_0}\left[B_{n,s}^2+2B_{n,s}B_{n,m}+B_{n,m}^2\right] \tag{6.2}$$

resulting in a contribution which can be decomposed into three parts. The stator contribution and rotor flux contributions are results of the armature excitation and the PMs, respectively, where as the third term is a contribution from the interaction of the two fields. In Sections 3.2 and 3.3 the derivation of these contributions are presented and is only briefly summarized here. If the effects of stator slots are neglected, the frequencies and circumferential orders of the three contributions can be summarized as

$$f_{nm} \propto [2up\omega t,\ 2up\theta] \tag{6.3}$$

$$f_{ns} \propto [2p\omega t,\ 2vp\theta] \tag{6.4}$$

$$f_{nsm} \propto [(1\mp u)p\omega t,\ (u\pm v)p\theta]. \tag{6.5}$$

where $u = 1,3,5,...$ and $v = 1,5,7,11,....$ In the square brackets, the first term constitutes the time harmonics and the second term the absolute value of the spatial orders. Equations (6.3), (6.4) and (6.5) represent the contributions from the PMs, the stator excitation and the interaction of the two, respectively. As of before, p, ωt and θ are the number of pole pairs, the mechanical frequency of the mechanical circumferential angle, respectively.

6.1 Influence of stator slots

6.1.1 Closed stator

The design of the stator teeth becomes a sensitive matter if magnetic saturation in the material is considering. When a ferromagnetic material, such as iron, is exposed to an external magnetic field (H) a magnetization occurs in the material, creating a magnetic flux (B). The relation between magnetic field and flux can be expressed as $B = \mu H$, where μ is the permeability. At a certain level, an increase in magnetic field will no

longer generate a higher magnetic flux, a phenomena known as saturation. Physically, saturation occurs when the magnetic domains in the material are all aligned.

As previously discussed, the effects of the slots on the flux density and force density is studied by changing the stator teeth design. As a starting point, closed stator slots are investigated, meaning that the stator slots are removed by completely uniting adjacent teeth. Obviously, this is not a realistic design for a physical machine since the flux to a very large extent will leak between the teeth instead of passing through the stator joke and the rotor. Additionally, such a design will have implications on manufacturability. However, it gives an understanding for the magnetic saturation and the appearance of spatial harmonics caused by the slotting.

In figure 6.1 results from FEM-simulations with closed stator slots are presented for two cases in no-load operation. Firstly, with permeability according to a B-H curve for the non-linear iron material. Secondly, with a constant permeability of $\mu_r = 10^5 H/m$. On the y-axis is the flux intensity presented and on the x-axis is the circumferential angle seen. The data is obtained at a single time instance. In relation to Fig. 3.2 and 3.4 in Chapter 3, the data is obtained along the axis marked *Position (θ)*. As can be seen, the difference in permeability results in different flux density characteristics, even in the case of no-load operation. Considering the case with $\mu_r = 10^5$ as the ideal case, one can conclude that saturation itself affect the results. The largest deviations are seen in the areas where the stator slots normally would have been. The filler material bridging two adjacent teeth is 1.6 mm thick which is narrow enough to cause local saturation when the non-linear iron material is used, even though the stator current is zero. In figure 6.2 the harmonic content of the two cases is presented. The space harmonics are presented with mechanical rotational angle as reference. Therefore, the first harmonic (n=5) corresponds to the fundamental electric component due to the five pole pair rotor design.

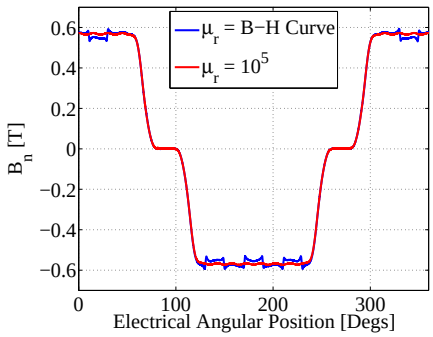

Figure 6.1 Comparison of flux density magnitude in the airgap close to the stator teeth for a closed stator with different permeability during no-load

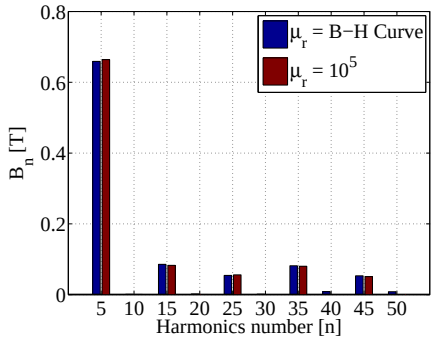

Figure 6.2 Harmonic content of the flux density in the airgap close to the stator teeth for a closed stator with different permeability during no-load

At first sight the 45^{th} harmonics, equaling the number of stator slots, would be expected to change considerably when the slots and permeability is changed. This can be explained with the theory presented in Section 3.2 where in Fig. 3.3 the resulting space and time harmonics of no-load conditions are presented in a frequency/wave-diagram. According to theory, the slotting influence primarily the 40^{th} and the 50^{th} space harmonics, in the case of 45 slots and 5 pole-pairs. Studying the analytical expression for the radial flux density originating from the PMs, for convenience presented here once more, the origin of the different components can be declared. It can be expressed as

$$B_{n,m} \propto \sum_{u=2k-1} \sum_{x} B_{m,u} cos\left(up\omega t - (up \pm xN_s)\,\theta\right). \tag{6.6}$$

where $k = 1, 2, 3, ...$ and $x = 0, 1, 2, ...$ Neglecting the stator slots (x=0), it is seen that the first five spatial harmonics are $|-up| = [5,\ 15,\ 25,\ 35,\ 45]$. For $x = 1$, the five lowest even harmonics obtained are $|-(up \pm N_s)| = [0,\ 10,\ 30,\ 40,\ 50]$. Clearly, with the configuration of 45 slots and 5 pole-pairs, the even PM flux density harmonics are caused by the interaction with the stator slots, which is in correlation with literature [1], [36].

6.1.2 Variation of stator slot opening width

In this section, the permeability is represented by the non-linear B-H curve previously used and the stator slot opening, B_{s0}, is changed in discrete steps. Both the tangential and the radial components are investigated and the FEM-data is obtained in the airgap in the

close vicinity of the stator teeth. The analysis is done both in no-load operation and in motor operation with a RMS current of 150 A. The variable B_{s0} is visualized with black arrows in Fig. 6.3, and the five discrete steps are tabulated in Table 6.1.

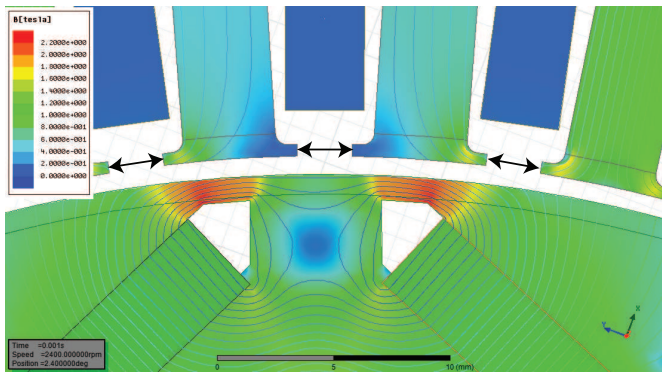

Figure 6.3 2D FEM-model. The variable B_{s0} is indicated by black arrows

Table 6.1 Discrete steps of stator slot opening width B_{s0}

#	Width [mm]
1	1.6
2	2.0
3*	2.4
4	2.8
5	3.5

* Original value

Results of changing the width of the stator slot opening for the no-load case can be seen in figure 6.4 and 6.6 for the radial (B_n) and tangential (B_t) flux densities, respectively. In figure 6.4 one can clearly see that the duration (in angular degrees) of the irregularities in the radial flux is highly affected, as expected due to the variations in stator slot width. In figure 6.6 one can also see that the magnitude is affected significantly for the tangential component. For the case when the machine is loaded in motor operation, the characteristics are to a certain extent different due to the interaction of the armature field. However, the effects of changing the slot opening width, B_{s0}, are the same as for the no-load case, which can be seen comparing figure 6.4 to 6.5 and figure 6.6 to 6.7.

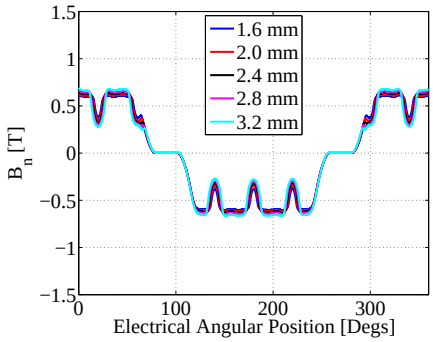

Figure 6.4 B_n as a function of angular position at no-load operation

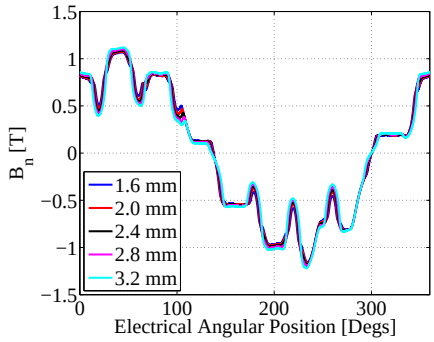

Figure 6.5 B_n as a function of angular position at load with i_{rms}=150 A

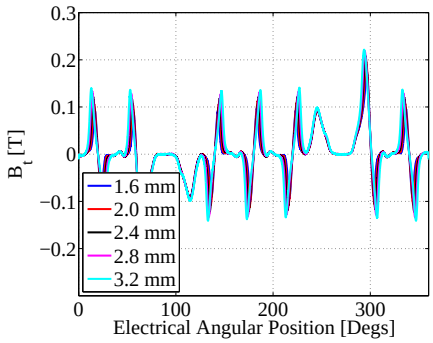

Figure 6.6 B_t as a function of angular position at no-load operation

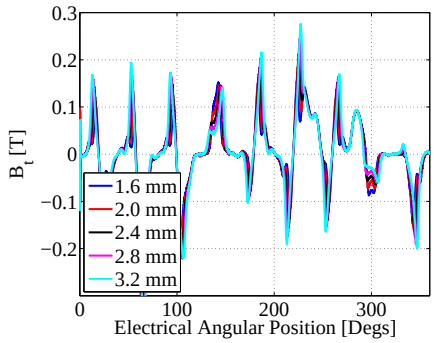

Figure 6.7 B_t as a function of angular position at load with i_{rms}=150 A

In figure 6.8 the spatial harmonics up to 50 are presented for the radial flux density during no-load operation, normalized with the mechanical rotational speed. The fundamental component of the radial component which can be seen in figure 6.1 is translated to the 5^{th} harmonic due to five pole pairs, when using mechanical references. Note that the data is collected at a single time instance, hence the harmonics represents space harmonics and not time harmonics.

As can be seen in figure 6.8 and 6.9, the magnitude of the 40^{th} and the 50^{th} harmonics tends to decrease with a decreased slot width. Comparing this data with figure 6.2, where the harmonic content is presented for a closed stator with different permeability, one can clearly see a difference in particularly the 40^{th} order. The 40^{th} order is not present in the ideal case in figure 6.2. However, when the permeability is defined by the B-H curve, it is. Its appearance is a result of the combination of number poles pairs and

stator slots, as previously discussed.

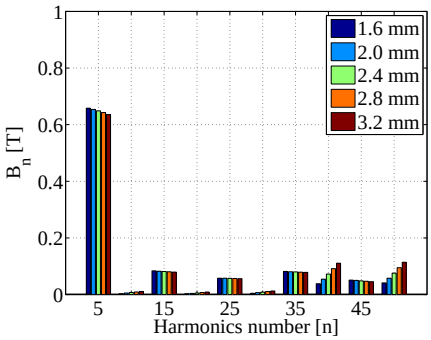

Figure 6.8 Space harmonics of B_n normalized with the mechanical rotational speed at no-load operation

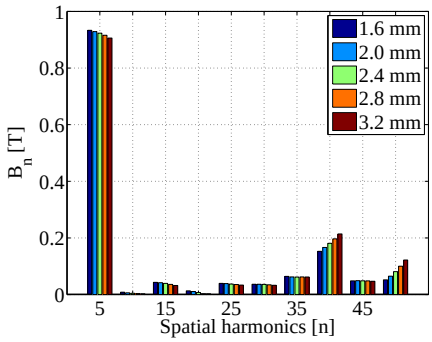

Figure 6.9 Space harmonics of B_n normalized with the mechanical rotational speed at load with i_{rms}=150 A

In figures 6.10 and 6.11 the spatial harmonics of the force density is presented during no-load and load operation for the five different cases of stator slot opening widths. As for the previous cases, FEM-data from one electrical period is used. As can be seen, the width of the stator slot opening has a more significant affect on the odd harmonics than on the even ones. Clearly seen in figure 6.11, when the machine is loaded, the 35^{th}, 45^{th} and 55^{th} space harmonics are significantly increased as the slot opening is extended.

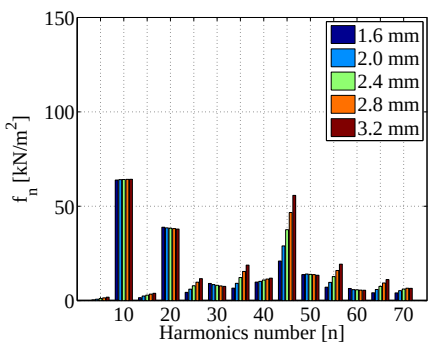

Figure 6.10 Force density space harmonics normalized with the mechanical rotational speed for different stator slots opening at no load

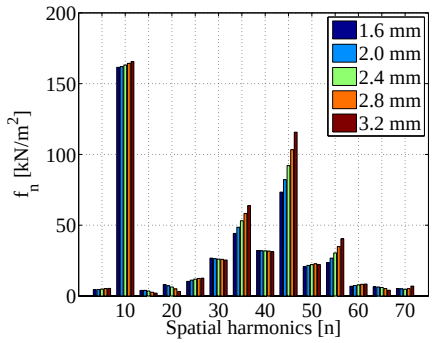

Figure 6.11 Force density space harmonics normalized with the mechanical rotational speed for different stator slots opening at load with i_{rms}=150 A

Studying only spatial harmonics gives an understanding for how the slots and the slot opening width affects the harmonics. However, the information about frequency is lost hence the ability to draw any conclusions are limited. As discussed in Chapter 3 it is of high importance to keep track of both spatial or temporal harmonics.

In Fig. 6.12 and 6.13 the force density is presented in frequency/wave-diagrams for $B_{s0} = 1.6$ mm and $B_{s0} = 3.2$ mm, respectively. It can be seen that the harmonic (40,5), meaning a frequency component of 40 times the mechanical rotational speed (y-axis) and a circumferential order of 5 (x-axis), is changed significantly. This component is an origin for noise due to the low circumferential order and the relatively high frequency, as discussed in Chapter 3. In Fig. 6.14 this component as well as (90,0) is presented as function of B_{s0}. The values are presented percent, where the largest slot opening ($B_{s0} = 3.2$ mm) are used as reference. As can be seen, the magnitude of the force density component (40,5) is continuously decreased with the slot opening width, whereas there is a minimum in the region around 2.5-2.8 mm for the component (90,0). One can conclude that the variable can be used to control or limit the radiated noise associated with these vibrational orders.

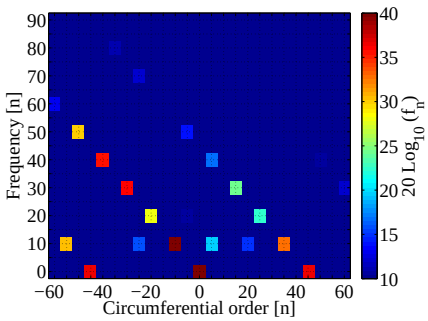

Figure 6.12 Frequency and mode number of the radial force density during normal load operation with $i_{rms} = 150$ with $B_{s0} = 1.6$ mm

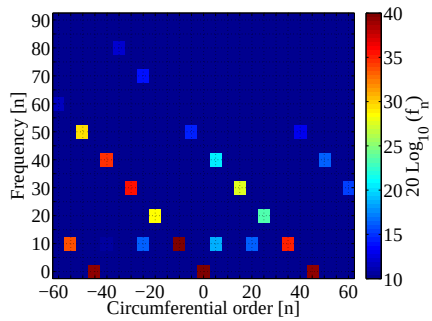

Figure 6.13 Frequency and mode number of the radial force density during normal load operation with $i_{rms} = 150$ with $B_{s0} = 3.2$ mm

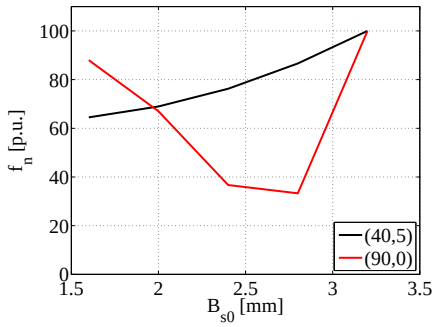

Figure 6.14 Comparison of force density harmonics (40,5) and (90,0) in relation to stator slot opening width B_{s0} during normal load operation with $i_{rms} = 150$

6.2 Inverter switching influence on force density harmonics

In Fig. 6.15 the differences in airgap force density are presented between SPWM and DPWM, as $f_{n,SPWM} - f_{n,DPWM}$ in kN/m^2. Data from the two cases are obtained from voltage excited FEM-simulation where the input voltage is supplied by an ideal three-phase inverter. In the DPWM case, one phase is always clamped to either the positive or the negative DC-link voltage, as discussed in Chapter 2.

Comparing the two cases, the difference in magnitude is considered negligible. When the sinusoidal phase current excitation is changed to voltage excitation the current is not an input but rather a result of the operating point and the applied voltage. Consequently, the difference that is presented might be a result of a slightly different magnitude of the fundamental component and hence a slightly different operating point.

No significant harmonic components are added within the presented range of frequency and circumferential orders, when the source is changed from a ideal current source to a switched voltage source. Consequently, one can argue that the switching in the inverter has small influence on low order force density harmonics. Meaning that the fundamental component of the phase current is the most dominating contributor to low order harmonics. This is also motivated by the theory presented in Section 3.3. In Fig. 6.16 the phase A current is presented in time domain. As can be seen, the DPWM case has more harmonics, which is expected. However, these are high frequency harmonics which is a result of the inverter switching.

Harmonics in the current will generate harmonics in the flux density. Considering the square operator in the Maxwells Stress Tensor, it is reasonable that additional harmonics in the flux density has small impact on the total force density. A harmonic

with a magnitude of 1% of the fundamental in the flux density is simply translated to a force density harmonic of $0.01^2 = 0.0001$ or 0.01% of the fundamental force density component.

Consequently, one can argue that noise and vibration originating from the lower vibrational orders and frequencies are caused by the fundamental component in the armature and rotor fields as well as the geometric design allowing for interaction and influence of stator slots. Resultantly, variations in the modulation technique and/or switching frequency is therefore assumed to have a small impact. Although, the angle of the dq-current might influence since it will affect the phase shift between the armature and the rotor fields. However, this is not treated in this work.

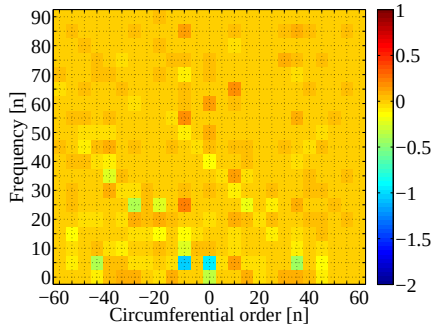

Figure 6.15 Difference in radial force density harmonic content using SPWM and DPWM as $f_{n,SPWM} - f_{n,DPWM}$ in kN/m^2 at 2400 r/min, $i_{rms} = 150$ A

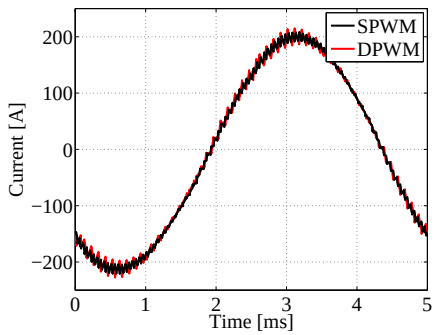

Figure 6.16 Phase A current using SPWM and DPWM at 2400 r/min, $i_{rms} = 150$ A

Chapter 7

Evaluation of modulation techniques

The objective of investigating DPWM and different levels of switching frequency randomization, as an alternative to SPWM with a fixed switching frequency, is to increase the energy efficiency of the inverter. Also, a positive effect of decreased inverter losses is that the peak power transfer through the inverter can be increased, which would result in an increase in both peak torque and peak power. Another essential point is to investigate the high frequency noise and vibrations that are caused by the inverter switching, and hence affected the choice of modulation technique.

The frequency content of the radiated noise can be divided into machine harmonics and PWM harmonics. For the investigated machine and with a switching frequency of 10 kHz, the PWM harmonics are located in the region of 5-10 kHz. Up to this point, only low frequencies have been considered (machine harmoncis), both spatially and temporally, for airgap flux density and force density. As previously discussed, the machine design and the fundamental component of the airgap flux density contributions cause noise complications. This is due to force density components which all can be categorized as low frequency components by the relative low frequency in both time and space. In a similar manner, the appearance of harmonics in the phase current due to inverter switching causes high frequency components in both flux density and force density which might result in emitted noise with the potential of being very annoying for persons inside a vehicle. This is due to the characteristics and frequency content in the region of 5-15 kHz. These PWM harmonics are focused upon in this chapter.

The work presented in this and the next chapter is focused on sideband harmonics centered at the switching frequency. Harmonics centered at twice the switching fre-

quency are in the upper end of, or above, what a human ear normally can detect. At very high rotational speeds, some of these sideband harmonics are in a frequency range where they normally can be heard. However, for the intended application, at high rotational speeds the inverter noise is masked by noise from tires and aerodynamic origin. Therefore, these harmonics have not been considered.

At this point, it is of importance to return to the concept of radiation efficiency, resonance and forced vibrations. As the fundamental component of the phase current by far exceeds the harmonics caused by the switching, it might seem contradictory that the inverter switching will have any significant influence at all. However, the radiation efficiency's frequency dependency puts the magnitude of the force density in a secondary position. In other words, force density harmonics with, what might be considered, having a low amplitude can cause significant emitted noise if the radiation efficiency of the stator for the particular frequency is high. Moreover, although eigenfrequencies of low order mode-shapes are unlikely to be excited by the high frequency forces, noise can still be generated by the concept of forced vibrations.

The inverter switching generates phase current harmonics which cause harmonics in the flux density and further on in force density. Consequently, it is reasonable to assume that the selection of modulation technique highly influences the emitted noise with frequency content in the vicinity of the switching frequency.

An evaluation on a system level, in opposition to component level, gives a greater insight on performance as well as possible consequences. From all possible evaluation methods and criteria, a few key performance indices are selected in the evaluation of high frequency harmonics; the invert energy efficiency and the perceived sound quality as well as stator back vibrations and velocity. The perceived sound quality evaluation is further discussed in Chapter 8 whereas the inverter efficiency is covered in this chapter. In addition to these performance indices, parameters such as electromagnetic torque ripple and disturbances on the power supply side of the inverter are parameters that are of interest as well. However, difference in torque ripple due to inverter modulation technique is considered to be of high frequencies and thereby having less impact due to the significant mechanical inertia in the system. The dc-side of the inverter and possible adverse effects due to the modulation are not within the scope of the thesis.

In this Chapter, firstly the inverter energy efficiency is studied, solely based on simulation results. Thereafter, phase current harmonics are investigated based on measurements to give a more comprehensive understanding of the outcome from the different modulation techniques. Lastly, harmonics in the flux density and force density are studied to understand how harmonics due to the modulation are related to noise and vibrations and how the core losses are affected by the harmonic content.

7.1 Inverter energy efficiency

In this section, firstly, a loss decomposition analysis is done where the different loss components are compared for the two modulation techniques, SPWM and DPWM. Thereafter, an evaluation is made based on drive cycle analysis. The evaluation aims to put the findings in a context to further investigate the impact of the energy savings.

7.1.1 Loss decomposition

Studying the loss decomposition in the inverter provides a broad understanding for how DPWM differs from SPWM. In Fig. 7.1 and 7.2 the total inverter losses for SPWM and DPWM are presented, respectively. The data is obtained from complete drive system simulations including battery, inverter and the electrical machine where the IGBT used is the one tabulated in Table 4.3.

As can be seen, the loss difference is considerable throughout the entire diagram. For instance, at a rotational speed of 4000 r/min and 35 Nm of torque the decrease in losses is roughly -20 percent. The field weakening region is clearly noticeable. As the PM flux in the machine needs to be counteracted, the phase current magnitude is increased with increased inverter losses as a result.

In Fig. 7.3 and 7.4 the switching losses are presented for SPWM and DPWM, respectively. For the switching losses, which is the loss component with the most significant difference, it is evident that the fewer commutations when using DPWM has a large impact. Although the number of commutations is decreased by $1/3$, the loss difference does not necessarily need to be of the same magnitude. For instance, at a rotational speed of 4000 r/min and 35 Nm of torque the difference is roughly -42 percent whereas at a rotational speed of 6000 r/min and 10 Nm of torque the difference is roughly -20 percent. This is further discussed in the end of this section.

As previously discussed, the clamping of the phases are centered around the peak of the phase voltage. With a power factor equal to one, this coincides with the peak of the momentarily power flowing through the IGBT or diode of that phase. It is reasonable to assume that a change in power factor impacts the difference in switching losses between the two modulation techniques due to the impact of the power flow distribution in the IGBTs and the diodes. Moving into the field weakening region, the power factor is decreased. This is a consequence of the need of counteracting the PM flux with stator current in order to reach higher rotational speeds. More reactive power is fed to the electrical machine to achieve this. As a result, apart from an increased current magnitude, the power flow is transitioned from passing through the IGBTs to the diodes. Consequently, the loss distribution in the inverter is affected by the power factor and hence the rotational

speed of the machine.

In Fig. 7.5 and 7.6 the reverse recovery losses are presented for SPWM and DPWM, respectively. As the number of commutations is decreased when DPWM is used, so is the number of reverse recovery event, causing a decrease in reverse recovery losses. As can be seen, the loss difference is significant in percent. However, the low absolute value results in small impact on the over-all losses.

Finally, in Fig. 7.7 and 7.8 the conduction losses are presented for SPWM and DPWM, respectively. Clearly, there is no difference in conduction losses which is expected. As the operational points and the power factor do not differ between the two modulation techniques, neither should the conduction losses. This might seem contradictory, since the switching pattern differs between the two options. However, during one switching period, the same active and zero vectors are used for both techniques. The duration of when the vectors are applied are also the same. The only difference is the order in which they are applied.

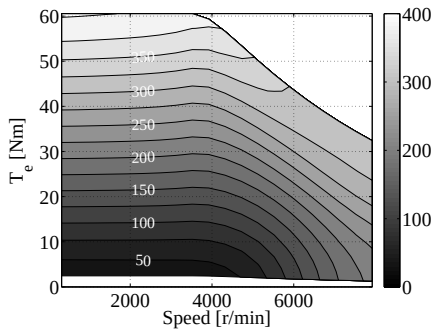

Figure 7.1 Total inverter losses using SPWM

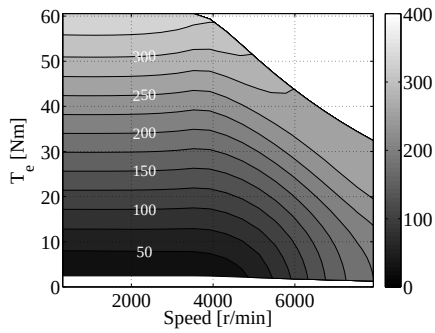

Figure 7.2 Total inverter losses using DPWM

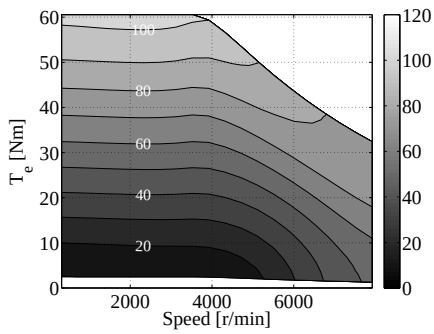

Figure 7.3 Turn-on and turn-off losses using SPWM

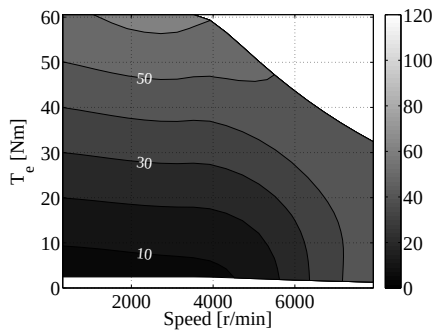

Figure 7.4 Turn-on and turn-off losses using DPWM

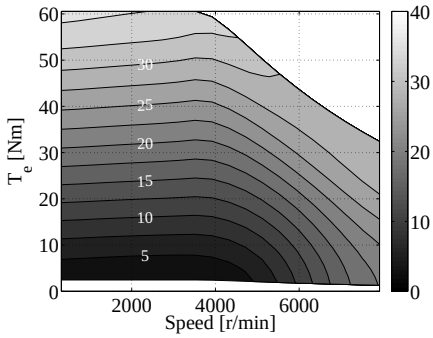

Figure 7.5 Reverse recovery losses using SPWM

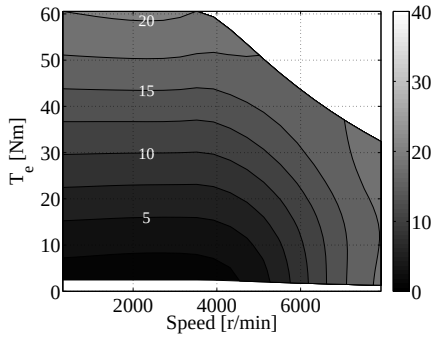

Figure 7.6 Reverse recovery losses using DPWM

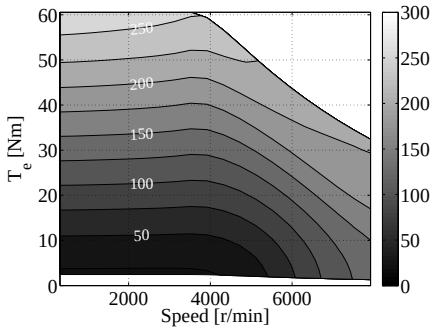

Figure 7.7 Conduction losses using SPWM, including both IGBTs and diodes

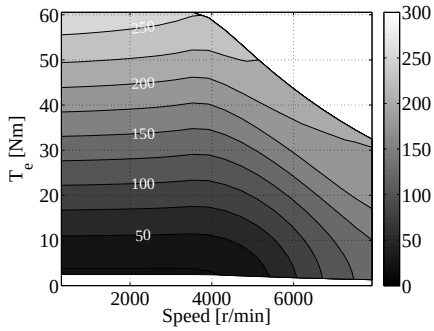

Figure 7.8 Conduction losses using DPWM, including both IGBTs and diodes

In Fig. 7.9 and 7.10 a detailed comparison between the two modulation techniques are presented, for four operating points. In Fig. 7.9 the selected operating points are presented and in Fig. 7.10 the loss data is presented in percent where SPWM is used as reference. As can be seen, the major part of the losses consists of conduction losses, followed by switching losses with the reverse recovery losses as the least significant contributor. Clearly, a decrease in the region of -15 to -18 % is obtained in the majority of the torque-speed diagram.

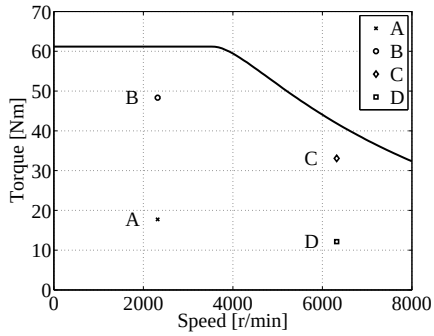

Figure 7.9 Selected operational points for comparison between loss decompositions

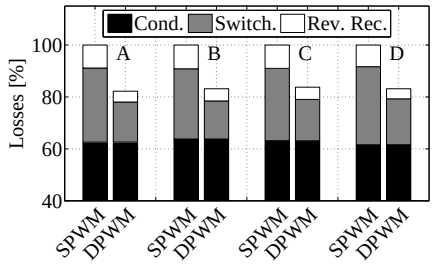

Figure 7.10 Comparison of decomposition of losses between SPWM and DPWM

In Fig. 7.11 and 7.12 the total inverter losses and the switching losses are presented as the percentage difference between SPWM and DPWM as

$$\Delta P = \frac{P_{DPWM} - P_{SPWM}}{P_{SPWM}} \times 100\%. \tag{7.1}$$

As can be seen, the electrical energy savings are substantial. Unsurprisingly, the DPWM modulation results in lower inverter losses. This is the result of the decrease in the number of commutations which results in, primarily, decreased switching losses. However, the decrease in number of commutations also decreases the number of reverse recovery events which amplifies the difference between SPWM and DPWM.

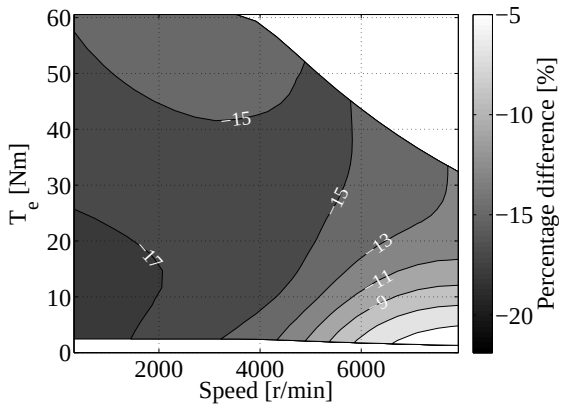

Figure 7.11 Difference in total inverter losses between SPWM and DPWM in percent.

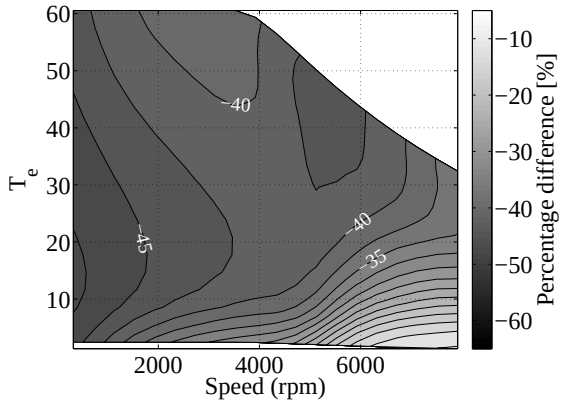

Figure 7.12 Difference in inverter switching losses between SPWM and DPWM in percent.

As can be seen in the lower right corner in the figures, the difference is decreased. This is a result of both the change in power flow distribution and how the transition from when a phase is clamped to returning to normal operation, or vise versa, is treated. In the simulations and the experimental testing the transition to and from clamping-state is done at the end of a switching period with the voltage vector [0 0 0].

To both enable and disable positive clamping, switching that phase is needed. In order words, positive clamping requires an action in terms of switching to enter and to leave the state. Accordingly, the influence on the energy savings is decreased as the number of consecutive switching periods when a phase is clamped is reduced. When the time to complete 60 electrical degrees of rotation equals the switching period time, the advantage of DPWM is lost since the number of commutations in a switching period is then unchanged. At 6000 r/min the fundamental frequency equals 500 Hz. At this rotational speed 60 electrical degrees is completed in $\frac{1}{500}\frac{60}{360} = 333.33\ \mu s$. With a switching frequency of 10 kHz, a total of 3.33 switching periods are covered during these 60 electrical degrees. Consequently, this phenomena is likely to affect the outcome even though the rotational speed and the switching frequency is of reasonable values.

Clearly, the energy savings in percentage is dependent of the IGBT-module parameters, hence these results are not unanimous for all IGBT-modules. However, the same analysis was done with the IGBT-module SKM800GA125D presented in Table 4.2, showing very similar results. The percentage difference in total inverter savings for the two IGBT-modules is less than 2 percentage units.

7.1.2 Evaluation based on drive cycle analysis

The drive cycle used to further analyse the impact on the energy savings is the extra urban drive cycle (EUDC) for low power vehicles. In comparison to the normal EUDC cycle, the top speed of the extra urban version is reduced from 120 km/h to 90 km/h. The vehicle used in the drive cycle analysis is the Volvo C30 Electric, presented and parameterized in Section 2.5. It is worth noting that the drive system is small for the vehicle it is propelling in the analysis. Although, the analysis is done to give further insight in the differences between the two modulation techniques from an energy efficiency perspective.

In Fig. 7.13 the speed profile and the vehicle acceleration for the EUDC cycle is presented and in Fig 7.14 the electromagnetic torque from the simulation are presented. As can be seen, the peak electromagnetic torque is achieved during braking at the end of the cycle reaching -61 Nm, regenerating approximately 25 kW. During acceleration the peak torque is 40 Nm and the peak output power is roughly 22 kW, which can be seen in Fig. 7.15 presenting the momentary output power of the electrical machine. The output power and the torque might seem moderate, although it is sufficient to track the speed profile.

The total inverter losses for both SPWM and DPWM are presented in Fig. 7.16. Summarizing the losses, the total energy loss during the entire cycle is 20.3 Wh and 17.7 Wh for SPWM and DPWM, respectively. In percentage, the decrease in total energy loss when using DPWM in comparison to SPWM is -12.9 percent. With a gear ratio of 9:1 the peak vehicle speed of 90 km/h corresponds to a rotational speed of the electrical machine of 6714 r/min. The high rotational speed and low torque corresponds to the lower right corner in Fig. 7.11. If a higher gear ratio is used, the rotational speed of the machine would be decreased whereas the energy difference would likely increase, considering the data previously presented.

To conclude, energy savings from the EUDC analysis and the analysis presented in Section 7.1.1 it is reasonable to assume a total decrease in inverter losses in the region of 12-17 percent, when DPWM is used instead of SPWM. The majority of the decrease is due to decreased switching losses, but also the decreased number of reverse recovery events influences positively, all due to the decreased number of commutations.

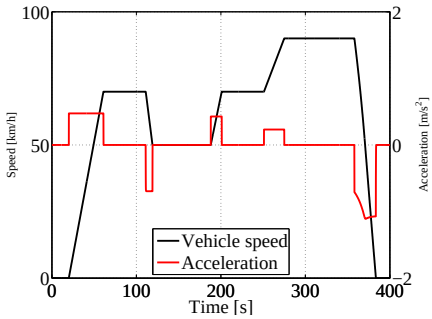

Figure 7.13 Speed profile and acceleration as function of time for the EUDC driving cycle

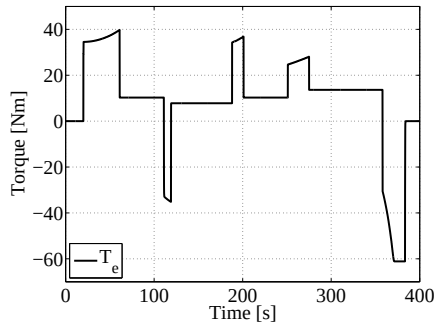

Figure 7.14 Resulting electromagnetic torque and load torque during the EUDC-cycle

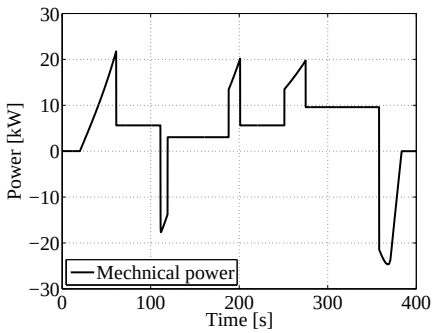

Figure 7.15 Output mechanical power during the EUDC-cycle

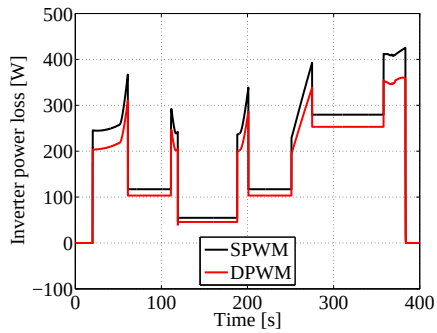

Figure 7.16 Total inverter power loss during the EUDC-cycle

7.2 Measured phase current harmonics

As a consequence of decreasing the number of commutations, the harmonic content of the phase current will be affected. The frequency range of interest is in the vicinity of the switching frequency, covering the most significant switching frequency sideband harmonics. The frequency range are within the hearable frequency range of the human ear and is usually perceived as disturbing, as discussed by Chai et al. [45]. Moreover, harmonics around twice the switching frequency are affected as well. Although, these do not contribute as significantly to issues with sound quality hence improving these by lower their magnitude are of secondary importance.

In Fig. 7.17 the most significant phase current harmonics are presented, obtained by measurements. The data is collected during a rotational speed sweep from 500-6500

r/min with peak torque corresponding to the upper profile in Fig. 7.1, with a fix switching frequency of $f_s = 10$ kHz. As can be seen, the magnitude of the presented harmonics for the DPWM case exceeds the SPWM case below base speed. In the field weakening region, the difference between SPWM and DPWM for $f_s \pm 4f_0$ is considerably decreased. Here, f_0 is the fundamental frequency.

Additionally, the characteristics of the data presented in Fig. 7.17 is clearly in line with findings presented by Tsoumas et al. [24], where the characteristics of the different harmonics are presented up to unity modulation index.

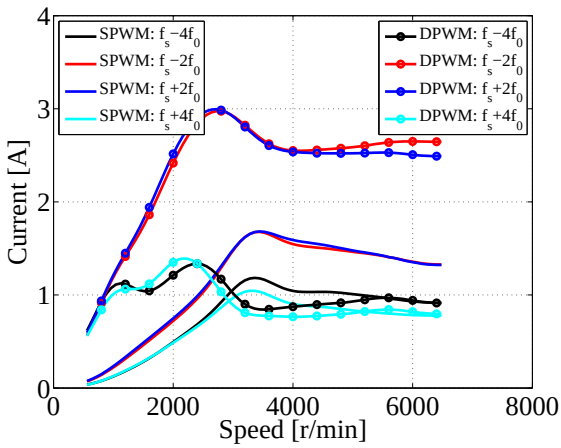

Figure 7.17 Measured phase current harmonics around the switching frequency during rotational speed sweep from 500 to 6500 r/min with peak load torque. The base speed is approximately 3700 r/min

Based on the data presented in Fig. 7.17 it is evident that the rotational speed affect the harmonic content. This, as well as the influence of load torque, is studied in Section 7.2.1. As previously discussed, randomization of the switching frequency is of interest to decrease the magnitude of the harmonics and ultimately decrease the tonality of the emitted noise, by smearing out the high frequency harmonic spectra of the force density. The influence of switching frequency randomization on the phase current harmonic sidebands to the switching frequency is studied in Section 7.2.2.

7.2.1 Influence of rotational speed and load torque

The harmonic content is dependent on the rotational speed of the machine, as previously discussed and presented in Fig. 7.17. In Fig. 7.18 and 7.19 the harmonics around the switching frequency is presented for different load torques and rotational speeds,

respectively. The data is obtained from measurements. As can be seen in Fig. 7.18, $f_s \pm 2f_0$ is significantly enlarged when DPWM is used, in comparison to SPWM. On the other hand, DPWM results in lower magnitudes for the harmonics $f_s \pm 4f_0$. Focusing on the harmonics $f_s \pm 2f_0$ and $f_s \pm 4f_0$, it can be seen that for SPWM the influence of load torque is small. For DPWM, the case of a load torque of 35 Nm results in the highest magnitudes. As can be seen, the magnitude of the harmonics is not consistently increasing nor decreasing as the load torque is changed.

In Fig. 7.19 it can be observed that the harmonic content follows the characteristics seen in Fig. 7.17. One can see a significant decrease in magnitude for $f_s \pm 4f_0$ for DPWM when the speed is increased. Moreover, the two last cases are very similar with respect to magnitude. Comparing the data to the measurements presented in Fig. 7.17 is it seen that in the field weakening region the magnitude of the most significant harmonics are more or less constant.

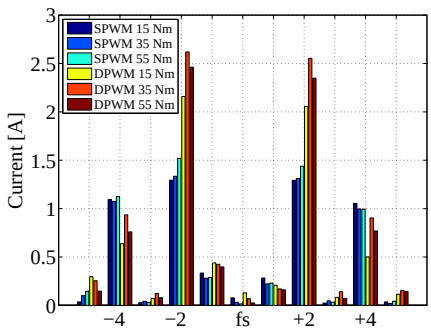

Figure 7.18 Influence of load torque on phase current harmonics around the switching frequency for a rotational speed of 3500 r/min

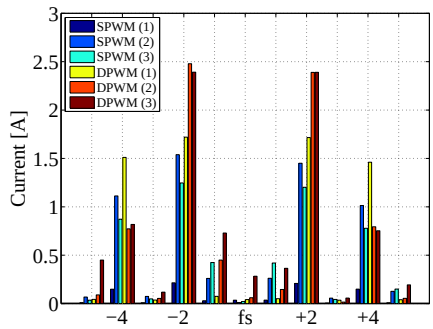

Figure 7.19 Influence of rotational speed on phase current harmonics around the switching frequency. The three speed cases are accordingly: (1) 1000 r/min 55 Nm, (2) 3500 r/min 55Nm, (3) 6000 r/min 35 Nm

7.2.2 Influence of switching frequency randomization

The randomization of the switching frequency is based on a Gaussian distribution with an expected value of $f_s = 10$ kHz and with different levels of variance (σ), presented in Table 7.1. In the context, the first case of $\sigma = 100$ Hz is by the author considered moderate, whereas the last case with $\sigma = 1000$ Hz is considered to have a rather substantial spread.

Table 7.1 Level of variance for the three cases used in the investigation of randomized switching frequency

Case [n]	Variance [Hz]
1	100
2	500
3	1000

In Fig. 7.20 and 7.21 the harmonics around the switching frequency for different levels of randomization are presented for both SPWM and DPWM, respectively. Generally, it can be concluded that even a moderate level of randomization significantly affects the tonality. Tonality is referred to as the difference between magnitude of harmonics and the over-all noise level. Also, the impact of increasing the variance is gradually decreased. As can be seen, the difference when the variance is changed from $\sigma = 500$ Hz to $\sigma = 1000$ Hz is significantly less than for instance the step from $\sigma = 100$ Hz to $\sigma = 500$ Hz.

It is of importance to understand the implications when the switching frequency is randomized. Clearly, the tonality is decreased, which is seen in decreased magnitudes of the specified harmonics in Fig. 7.20 and 7.21. However, the background noise level is consistently increased with an increased level of randomization. In Fig. 7.22 the phase current is presented, in the frequency interval of 8 to 12 kHz, when DPWM is used both without randomization ($\sigma = 0$) and with two level of randomization ($\sigma = 100$ Hz and $\sigma = 500$ Hz). As can be seen, the magnitude of the peaks are decreased, whereas the background noise level is increased. At a level of $\sigma = 1000$ Hz, the noise is comparable with the magnitude of the harmonics themselves, hence further randomization is without any gain. This case is not presented in Fig. 7.22 for clarity reasons.

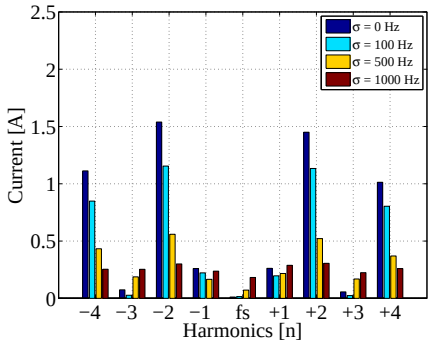

Figure 7.20 Measured phase current harmonics around the switching frequency using SPWM with different levels of randomization at a load torque of 55 Nm at 3500 r/min

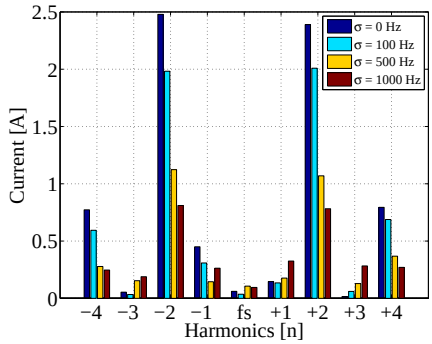

Figure 7.21 Measured phase current harmonics around the switching frequency using DPWM with different levels of randomization at a load torque of 55 Nm at 3500 r/min

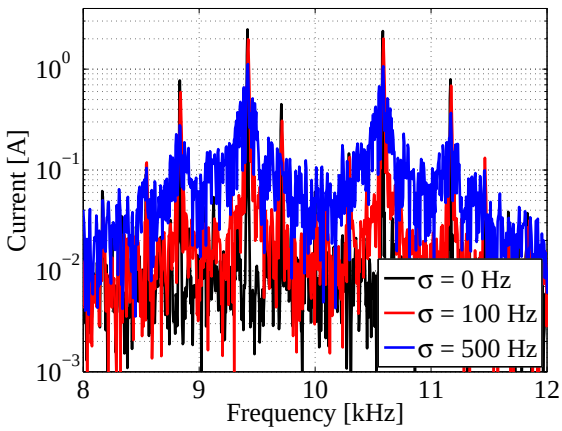

Figure 7.22 Comparison between different levels of randomization using DPWM, the data is obtained from measurements

Worth noting is that the same behaviour is expected in the radiated noise. Although, tonality is not the only measure of sound characteristics and hence not of sound quality. Previous research proclaims that randomization of the switching frequency is a prominent method to increase the sound quality by harmonic spreading [3, 6, 22, 23, 24, 25], which brings attention to the method.

To conclude, the randomization has favourable results on the tonality of the phase

current harmonics. Moreover, the harmonic spread is substantial as the variance is increased towards 1000 Hz, which for the given system is the limit where further randomization does not contribute to any decrease of the harmonics of interest. In Chapter 8 the randomization of the switching frequency is evaluated from a sound quality perspective by investigating the perceived annoyance.

7.2.3 Measured stator velocity and radiated noise harmonics

When evaluating the effect on stator housing vibrations, it should be pointed out that the global response is considered instead of single measurement points. The reason for this is that significant variations can occur between different measurement points due to the considerable modal density in the frequency range of interest. At higher frequencies different mode-shapes occur more frequently hence the modal density is said to be high, i.e. a large ratio of mode-shapes over frequency range. In such cases the vibrations are not as pure as for lower frequencies and geometrically, the image can be viewed as very irregular and not as pure as the examples presented in last part of Chapter 3. Consequently, single measurements can possibly be misguiding hence average values from all accelerometers are used.

In Fig. 7.23, the measured stator surface velocity harmonics are presented. Below base speed the difference between SPWM and DPWM is substantial. The most prominent harmonics are $f_s \pm 3f_0$ for DPWM and $f_s + 3f_0$ for SPWM. Also $f_s \pm f_0$ is more prominent for DPWM compared to SPWM. In Fig. 7.24, the same harmonics for the measured radiated sound pressure are presented, averaged over the eight microphones. As can be seen, there is a correlation between surface velocity and sound pressure, which is expected. An enlargement of $f_s \pm 3f_0$ in the stator vibrations should also be reflected in the radiated noise, which clearly is the case.

Also, the differences between SPWM and DPWM can be motivated with the previously presented theory and measurements of the phase current. However, to fully understand the relations, factors such as radiation efficiency and harmonic wavenumbers need to be addressed.

In conclusion, the theoretical expressions for the harmonic content in the force density are correct. Although only the harmonics that are of interest is selected and presented in this section, Fig. 8.1 in Chapter 8 clearly show the complete harmonic spectrum. Additionally, knowledge about the force density alone is not sufficient to quantify stator vibrations or radiated noise noise in particular. However, in a comparative study, studying the difference in force density can very well be sufficient. Since the airgap force density is a result of both the PM flux and the stator flux, caused by the excitation of the stator windings, the harmonic spectra of the phase current will affect the harmonic

spectra of the stator flux and hence the force density.

It is worth noting that for the measured phase current that is presented in for example the previous section, a symmetry can be seen between harmonics above and below the switching frequency, such as for $f_s \pm 2f_0$. Whereas in neither the surface velocity or the radiated sound no symmetry is seen. Considering the appearance of stator deformations and radiated sound as a function of the input phase current, one can conclude that the system is not linear.

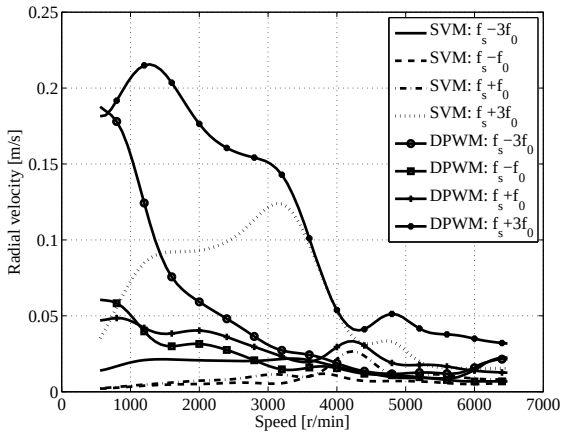

Figure 7.23 Measured radial velocity harmonics around the switching frequency during rotational speed sweep with peak load torque. The data is the average over the nine accelerometers mounted onto the cooling jacket of the PMSM.

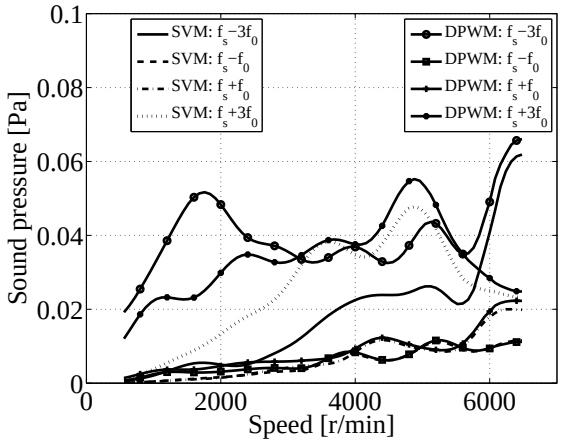

Figure 7.24 Measured radiated noise harmonics around the switching frequency during rotational speed sweep with peak load torque. The data is the average over the eight microphones.

7.3 Flux density and force density harmonics

As a consequence of the inverter operation, switching frequency sideband harmonics are created in the phase current, as previously seen. These harmonics are translated into the airgap flux density and consequently into the force density. The latter in accordance with the theory presented in Chapter 3. The phase current and flux density harmonics of significance, around the switching frequency, is dependent on the modulation index and hence the rotational speed of the machine [24]. For rotational speeds round base speed, the dominant switching frequency sideband harmonics are $f_s \pm 2f_0$ and $f_s \pm 4f_0$, where f_s and f_0 are the switching frequency and the fundamental electrical frequency, respectively. Due to the square operator in Maxwell Stress Tensor, for convenience presented here ones more

$$f_n \simeq \frac{1}{2\mu_0}(B_{ns} + B_{nm})^2 \tag{7.2}$$

switching frequency sideband harmonics with significant magnitudes in the force density are caused by the interaction between the fundamental component and harmonics in the flux density.

The resulting force density harmonics from interaction between the fundamental component, f_0, and the harmonic $f_s + 2f_0$ of the airgap flux density can be expressed as

$$f_n(t) \propto cos\left[2\pi(f_s - f_0)t\right] + cos\left[2\pi(f_s + 3f_0)t\right]. \tag{7.3}$$

Consequently, one of the flux density harmonics generate force density harmonics with frequencies corresponding to $f_s - f_0$ and $f_s + 3f_0$. Additionally, due to the synchronicity between the stator and the rotor fields, the term $2B_{ns}B_{nm}$, that originates from the evolvement of (7.2), will also generate force density harmonics with the same frequency content. In this case, due to the interaction between the fundamental component in the PM flux density and harmonics in the flux density from the stator excitation. Clearly, it is troublesome to determine cause of effect trying to link specific force density harmonics with specific flux density and phase current harmonics. One harmonic component in the force density is composed of several contributions with different phase angles and magnitudes.

However, a few relations can be established. Considering the most prominent harmonics and the fundamental component of the airgap flux density, a number of force density harmonics are obtained theoretically. The frequency content of these are tabulated in Table 7.2. It is worth noting that due to effects such as interaction with PM originated flux density, phase angle differences and magnetic saturation, the magnitude of the flux density harmonics does not necessarily scale linearly with the magnitude of the phase current harmonics.

A case study of three load cases and three stator excitations was done to numerically study switching frequency sideband harmonics in the stator current, flux density and the force density. The three load cases correspond to a mechanical rotational speed of 3500 r/min, equivalent to a fundamental frequency of approximately 292 Hz, with load torques of 15, 35 and 55 Nm.

If the total airgap flux density is expressed by a number of radial flux density harmonic components, the radial force density can be expressed using superposition, in conjunction with (3.27), as

$$f_n \simeq \frac{1}{2\mu_0}\left(\sum_i B_{n,i} cos\left(2\pi f_i + \theta_i\right)\right)^2. \tag{7.4}$$

As previously discussed in Chapter 6, harmonics in the stator current contribute to the airgap flux density. The most prominent harmonics in the flux density, around the switching frequency, are f_s, $f_s \pm 2f_0$ and $f_s \pm 4f_0$. Evolving (7.4), considering these harmonics and the fundamental component of the flux density, these flux density harmonics result in a number of theoretical force density components with the frequencies tabulated in Table 7.2.

Table 7.2 Frequency content relation between force density (f_n) and combinations of airgap flux density harmonics ($B_{n,i}$)

f_n	$B_{n,1}$	$B_{n,2}$
f_s+3f_0	f_0	f_s+4f_0
f_s+3f_0	f_0	f_s+2f_0
f_s+f_0	f_0	f_s+2f_0
f_s+f_0	f_0	f_s
f_s-f_0	f_0	f_s
f_s-f_0	f_0	f_s-2f_0
f_s-3f_0	f_0	f_s-2f_0
f_s-3f_0	f_0	f_s-4f_0

In Fig. 7.25 harmonics around the switching frequency of phase current, airgap flux density and force density are presented. The data is obtained from FEM-simulations where the three operational points are investigated using sinusoidal current excitation, SVM and DPWM. The FEM-simulations are performed using voltages from an ideally switched inverter, as described in Section 5.3. As can be seen, the most significant current harmonics are, as expected, $f_s \pm 2f_0$ and $f_s \pm 4f_0$. The same harmonics are also among the most significant ones in the flux density. Furthermore, the theoretical force density harmonics that were tabulated in Table 7.2 can be seen to coincide well with the most significant ones in Fig. 7.25. The most significant difference in the force density, comparing the two modulation techniques, is clearly $f_s \pm f_0$, which is a partly a result of the increase in the flux density and the phase current harmonics $f_s \pm 2f_0$, in accordance with the analytically determined relations presented in Table 7.2 as well as the measured phase current harmonics presented in Section 7.2.1 and 7.2.2.

The flux density components contributing to the different force density harmonics seen in Fig. 7.25 are included in, but not limited to, the options presented in Table 7.2. Additionally, considering phase differences between flux linkage harmonics as well as magnetic saturation in the material, the complexity of the task to analytically determine general expressions for correlations between the magnitudes of phase current, flux density and force density is extensive and beyond reasonable efforts. However, general conclusions can be made about the correctness of the assumed frequency content in both the flux density and the force density. Moreover, one can conclude that an increase in magnitude of phase current harmonics is likely to increase the magnitude of the correlative force density harmonics as well, which is clearly seen in Fig. 7.25.

In the bottom part of Fig. 7.25 one can see the harmonic content around the switching frequency of the airgap force density. The force density is obtained as pre-

viously discussed with contributions from both radial and tangential components. If however the tangential component was to be neglected, the largest difference in the force density from what is presented in Fig. 7.25 would be less than 0.0235 kN/m^2, which occurs for harmonic $f_s - f_0$. However, in percentage, the largest difference is 17.6 % which occurs for $f_s + 5f_0$. Accordingly, in this case the influence of the tangential component is small in absolute values whereas in percentage the difference is significant for some harmonics.

Based on the findings it is reasonable that around the switching frequency harmonics will occur in both the stator vibrations and the radiated noise at frequencies corresponding to $f_s \pm f_0$, $f_s \pm 3f_0$ and $f_s \pm 5f_0$. However, due to the mechanical dynamics of the machine it is not evident which ones that are going to be more prominent than others, even though the magnitudes are known. Although, it is likely that the frequency component in the radiated noise corresponding to $f_s \pm f_0$ will be enlarged when DPWM is used in comparison to SPWM.

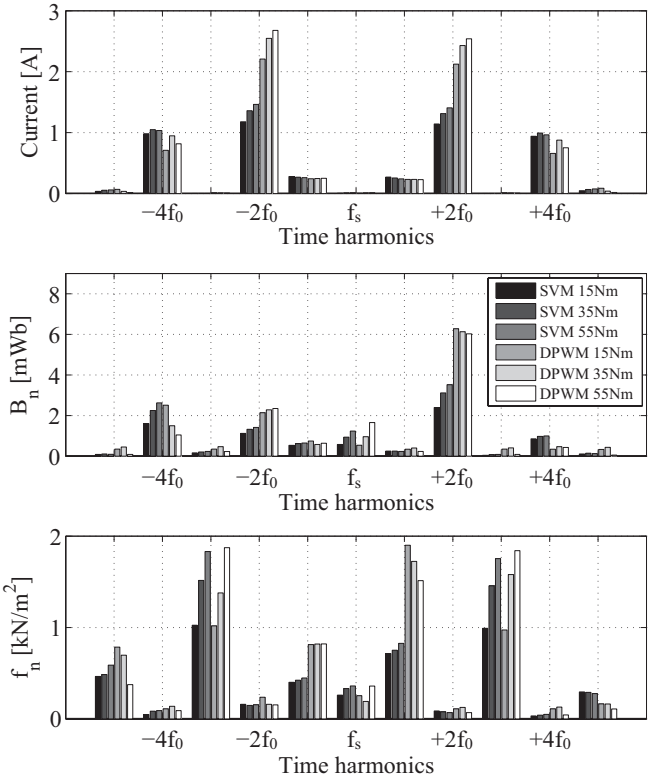

Figure 7.25 Harmonic content around the switching frequency, f_s=10 kHz, of phase current, airgap flux density (B_n) and force density (f_n) for the three investigated load cases at 3500 r/min, based on FEM-analysis

It is worth noting that due to effects such as interaction with PM originated flux density, phase angle differences and magnetic saturation, the magnitude of the flux density harmonics does not necessarily scale linearly with the magnitude of the phase current harmonics.

7.3.1 Machine and inverter losses

To evaluate the core losses for the three load cases the previously discussed Bertotti equation is used. In Table 7.3 a loss matrix is presented where the two PWM methods are extended with a third case of purely sinusoidal current excitation for comparison. The core losses are obtained from FE analysis. In the left-most column, the excitation

of the FE-modelling is presented and the three columns to the right lists the losses in Watt for three different load torques. The table is divided to show hysteresis losses, eddy current losses, copper losses and inverter losses individually. The data, which is obtained at 3500 r/min, can be compared with the measured phase current harmonics presented in Fig. 7.17, at the rotational speed of 3500 r/min. Clearly, the correlation between FEM-calculations and measurements are very good.

As can be seen, the differences between SPWM and DPWM are small. However, compared to a purely sinusoidal excitation, especially the eddy current losses are increased significantly. Furthermore, in [46] the Bertotti-formula and its limitations are investigated for different materials and frequencies. The findings indicate that the accuracy of the formula is questionable, with estimation errors for the material used in this thesis (M270-35A) reaching above 30 percent. However, comparatively, the obtained data is considered representative. Consequently, an increase in core losses when using DPWM can not be concluded based on the FEM-analysis only. Although, an increase is reasonable due to the increased phase current THD.

As can be seen, the losses in the inverter is a significant part of the total electrical losses for all the three load cases. The lack of possibility to draw any adverse conclusions about the core losses when SPWM is changed to DPWM, is favourable from a system-level loss perspective.

Table 7.3 Comparison of core losses and VSI losses for different excitations and load torque obtained from FEM-calculations at 3500 r/min

FEM excitation	T_e = 15 Nm	T_e = 35 Nm	T_e = 55 Nm
		Hysteresis Losses [W]	
Current	104.3	131.0	145.8
SPWM	104.7 (+0.5 %)	131.6 (+0.5 %)	147.7 (+1.3 %)
DPWM	105.3 (+1.0 %)	132.2 (+0.9 %)	149.2 (+2.3 %)
		Eddy Current Losses [W]	
Current	57.2	70.8	84.3
SPWM	100.1 (+75.0 %)	114.0 (+61.0 %)	126.3 (+49.7 %)
DPWM	99.1 (+73.2 %)	113.5 (+60.3 %)	126.2 (+49.6 %)
		Copper Losses [W]	
Current	19.5	85.7	189.2
SPWM	20.0 (+2.4 %)	85.7 (+0.0 %)	186.9 (-1.2 %)
DPWM	20.0 (+2.4 %)	85.6 (-0.1 %)	187.1 (-1.1 %)
		Inverter Losses [W]	
Current	-	-	-
SPWM	103.5 ($\pm$ 0 %)	245.9 ($\pm$ 0 %)	373.8 ($\pm$ 0 %)
DPWM	86.1 (-16.8 %)	207.6 (-15.6 %)	321.2 (-14.1 %)

Chapter 8

Influence of modulation techniques on NVH and perceived sound quality

8.1 Acoustic measurements

Several modulation techniques with different switching frequencies, switching frequency randomization and load torques are tested in both stationary and transient mode. Parts of the stationary testing results are presented in Chapter 7. The main vibrational harmonics of concern for the investigated machine, tabulated in Table 4.1, due to electromagnetic excitation in terms of direct radiated sound are orders 40 and 90 with respect to the mechanical rotational speed which was discussed in the previous chapter. In addition to these low circumferential vibrational orders, the frequency components at and centered around the switching frequency may also be audible and subject to perceived annoyance for passengers inside a car, which was briefly discussed in the introduction to the previous chapter.

As expected, only the sound or vibration components in the region of the switching frequency were affected with respect to changes of modulation technique and switching frequency. An illustrative example is given in Fig. 8.1 where both SPWM with and without random switching frequency and DPWM were sequentially used during a single rotational speed sweep. The most affected phase current harmonics, when going from SPWM to DPWM, are indicated in the figure. These harmonics were thoroughly investigated in the previous chapter.

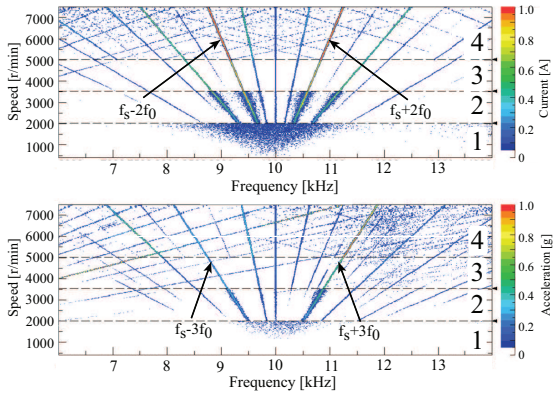

Figure 8.1 Phase current (above) and stator housing acceleration (below) for a combined rotational speed sweep at 55 Nm with $f_s = 6$ kHz. Segment 1: SPWM with 1 kHz bandwidth Gaussian random switching frequency, segment 2: SPWM with 100 Hz bandwidth Gaussian random switching frequency, segment 3: SPWM with fixed switching frequency, segment 4: DPWM60 with fixed switching frequency

Moreover, the frequency content of both the phase current and the stator vibration in Fig. 8.1 can be compared to Fig. 7.25 where the results of the FEM-calculations are presented. For the phase current, the six most dominant sidebands centered around the switching frequency (10 kHz) in the upper part of Fig. 8.1 are $f_s \pm f_0$, $f_s \pm 2f_0$ and $f_s \pm 4f_0$ which is clearly seen as the dominant ones in Fig. 7.25. Furthermore, the most affected phase current harmonics when going from SPWM to DPWM are $f_s \pm 2f_0$, indicated in the upper plot in Fig. 8.1. In Fig. 7.25, these can also be seen increasing when going from SPWM to DPWM.

From measurements, stator vibrations can be quantified. Based on acoustic transfer functions or acoustic measurements the acoustic response can be determined as well. Although, it is not evident how to evaluate the resulting acoustic image and how to quantify improvements or differences between different solutions from the perspective of a human ear and human perception in general. The question of how the noise is perceived was raised. To answer this question and to fully quantify the impact of modulations techniques as energy saving measures on the perceived annoyance, a listening test based on acoustic recordings was design and executed on 18 participants. In Section 8.2 the evaluation strategy, the methodology and the interpretation of the results are presented.

8.2 Sound quality assessments

8.2.1 Evaluation strategy

Since voltage modulation has acoustic drawbacks and switching frequency randomization might have positive impact on the sound quality perception, a directional survey was conducted in order to explore those relations. For each modulation strategy six sound files, each with a duration of five seconds, were created from rotational speed sweeps from 500 to 7500 r/min at peak torque from microphone #2 (see Fig. 4.6), according to Table 8.1 and 8.2. The purpose of the test was to evaluate the sound quality of components related to a switching frequency of 10 kHz. Therefore, the sounds were modified by a second-order recursive IIR high-pass filter with a cut-on frequency of 6 kHz, in order to suppress the influence of low vibrational orders and noise from surrounding equipment, such as the DC-machine used as load.

Table 8.1 List of modulation techniques used for sound quality assessments

#	Modulation
1	SPWM 10 kHz (reference)
2	SPWM 10 kHz, random switching frequency ($\sigma = 500$ Hz)
3	SPWM 10 kHz, random switching frequency ($\sigma = 1$ kHz)
4	DPWM 10 kHz
5	DPWM 10 kHz, random switching frequency ($\sigma = 500$ Hz)
6	DPWM 10 kHz, random switching frequency ($\sigma = 1$ kHz)

Table 8.2 Rotational speed sweep segments included in the sound quality assessment

Speed	Interval [s]	Speed range [r/min]
1	0-5	500-1090
2	10-15	1680-2280
3	20-25	2870-3470
4	30-35	4070-4670
5	40-45	5260-5860
6	50-55	6440-7040

The objective was to determine whether different modulation techniques alter the perceived annoyance caused by high frequency tones. Sounds recorded from the PMSM drive using different modulation techniques (number 2 to 6 in Table 8.1) were com-

pared to a reference sound (number 1 in Table 8.1) recorded from the PMSM drive using SPWM with a fixed switching frequency of 10 kHz.

8.2.2 Listening tests - method

A total of 18 subjects participated, 6 women and 12 men. All were volunteers. The mean age was 24 years (standard deviation 3.6 years) and all subjects had self-reported normal hearing. The sounds were reproduced through calibrated headphones (Head Acoustics PEQ V amplifier and Sennheiser HD600 headphones).

The test was based on the Multi Stimulus test with Hidden Reference and Anchor (MUSHRA) developed by the International Telecommunication Union [47]. The method was developed for audio reproduction where an unprocessed signal with full bandwidth may be used as the reference when the quality of processed or transmitted signals is evaluated. In the MUSHRA, the full bandwidth signal is used both as a known and a hidden reference. This means that the subjects at any time during the evaluation can listen to the reference and that the reference also is hidden among the remaining stimulus. In this study, the SPWM 10 kHz recording served as the reference sound and all other stimulus were to be compared to this reference. The MUSHRA approach is most appropriate for evaluating medium or large impairments. This makes the method suitable for evaluating differences caused by the use of different modulation techniques and different levels of switching frequency randomization.

In the MUSHRA, anchors are used to provide an indication of how the systems under test compare to well-known distortions [47]. Because the objective was to compare sounds from the PMSM drive with different modulation techniques, no conventional anchors existed and, therefore, were not included. As a result, the method was modified into a Multi Stimulus test with Hidden Reference (MUSHR) [48]. In the MUSHR, the subject was asked to judge the differences in annoyance for the sounds compared to the reference where 0 indicated no difference in annoyance, 100 indicated much more annoying and -100 indicated much less annoying. Only the stimulus that the subject thought was the hidden reference stimulus was given the value 0. For all other stimuli, the difference from the reference was judged on the scale ranging from -100 to 100. The listening test was controlled by the subject through a computer interface, shown in Fig. 8.2.

The analysis of the listening test results started with finding out how many of the subjects that could identify the hidden reference stimulus (SPWM 10 kHz) from the object stimuli (recordings of modulation techniques 2-6 in Table VI). This gave an indication of how similarly the stimuli were perceived. A Repeated Measures ANOVA was conducted to determine if the sound emitted during use of the different modulation techniques were perceived differently.

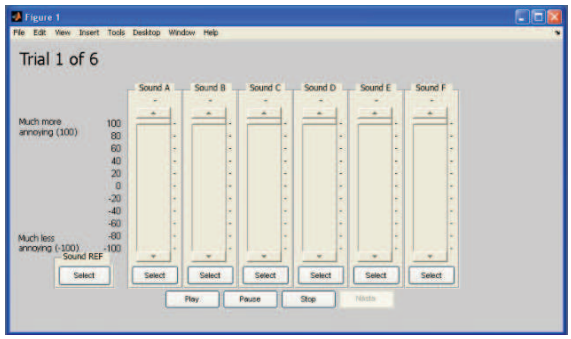

Figure 8.2 User interface for listening test.

8.2.3 Listening tests - results

The number of times each stimulus was judged as being the reference stimulus is shown in Table 8.3. From these results it is obvious that at lower rotational speeds most subjects easily identified the reference. At the highest rotational speed the differences between the stimuli (the different modulation techniques) became almost indistinguishable. This can be seen by the vast spread of what was perceived as the reference in the last and second to last rows in Table 8.3.

Table 8.3 Number of times each stimulus was judged as being the reference stimulus

Speed**	SPWM	SPWM 500 Hz	SPWM 1 kHz	DPWM	DPWM 500 Hz	DPWM 1 kHz
1	18	0	0	0	0	0
2	16	2	0	0	0	0
3	15	3	0	0	0	0
4*	13	2	0	1	1	0
5*	9	0	5	2	1	0
6*	3	1	3	4	1	5

* For each of these conditions one subject missed to mark one of the stimuli as being the reference stimulus

** Rotational speed sweep segments defined in Table 8.2.

A Repeated Measures ANVOVA was made to check whether there were significant $(p < .05)$ differences in perceived annoyance between the different modulation techniques. In order words, if the grading of the perceived annoyance varied significantly between the subjects. The objective of the test is to determine wether the differences in-

dicated by the subjects can be statistically ensured. Mauchlys Test of Sphericity was used to check whether the assumption of sphericity, one of the underlying assumptions for Repeated Measures ANOVA, had been violated. Sphericity refers to the condition that the variance of the difference of the subjects answers are all equal. If the variance of the difference between all combinations of the subjects answer, for each of the speed intervals, are roughly equal, the assumption of sphericity is not violated.

The ANOVA results show that there were significant differences in annoyance assessments between the different modulation techniques for all speed ranges, except for the highest speed segment. This is further discussed in the article *Influence of inverter modulation strategy on electric drive efficiency and perceived sound quality* which is now under review for publication in *IEEE Transactions on Transportation Electrification*, as presented in Section 1.4.

The mean annoyance is represented in Fig. 8.3. Note that the data is interpolated based on data from the six rotational speed sweep segments, seen in Table 8.2, for each combination of modulation technique and randomization. The peak torque is indicated to give further understanding for the rotational speed and appearance of the field weakening region. The figure is further discussed in the following section.

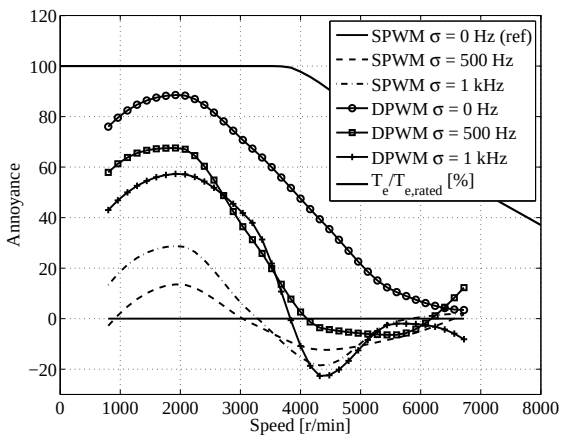

Figure 8.3 Perceived annoyance from acoustic listening test for the different modulation techniques. The data is interpolated based on the six speed cases presented in Table 8.2.

8.2.4 Interpretation of listening tests results

From the data, a three conclusions can be drawn. Firstly, the perceived annoyance is clearly higher for DPWM compared to SPWM for the first three speed segments. For the last three speed segments, the differences are generally small.

Secondly, up until field weakening, randomization of the switching frequency has a positive influence on sound quality for the DPWM samples. In most DPWM cases for these four speed segments, the 1 kHz randomization provides less annoyance than the 500 Hz variance. This is coherent with the impression from the visual inspection of Fig. 8.4 where a large number of prominent tonal components are being smeared out when using randomization, yielding a more broadband spectra. Although, Fig. 8.3 indicates that the step in variance from zero to 500 Hz has a larger impact than the step from 500 to 1000 Hz. It is also clearly seen below base speed in Fig. 8.3. Returning to the findings in Section 7.2.2, where the influence of switching frequency randomization on phase current harmonic spectra is studied, one can understand the reasonability in this phenomena. Conclusively, one can argue that randomization of the switching frequency is beneficial in the case of DPWM. However, further increasing the level of randomization does not necessarily improve the acoustic sensation substantially and as a tool it is not unanimously improving the situation, which can be seen for the SPWM cases.

Lastly, in the field weakening region, there were no statistically significant differences in perceived annoyance between the sound samples. This is coherent with the impression from the visual inspection of Fig. 8.5 where no large differences between the spectra can be observed. Note that the noise in that particular segment does not relate to the switching process itself. The broad band noise originates from the surroundings, possibly from equipment such as the speed reducer and the brake-machine.

Moreover, data presented in Fig. 8.4 agree with the theory in Chapter 3 and Fig. 7.17 where the current harmonics with highest magnitude for the given rotational speed are presented.

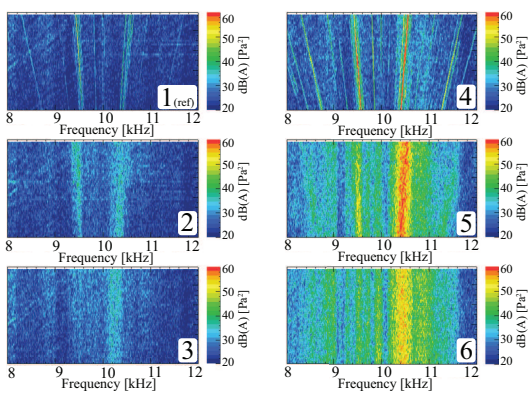

Figure 8.4 Autopower noise spectrum for the six modulation techniques, speed segment 2.

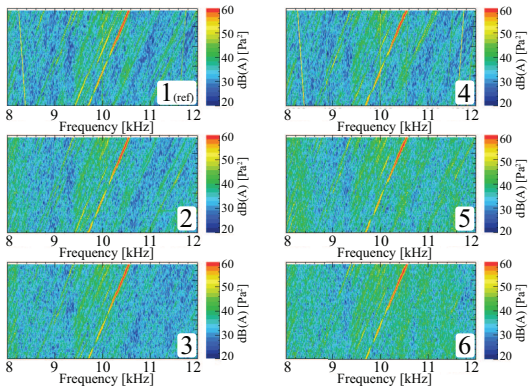

Figure 8.5 Autopower noise spectrum for the six modulation techniques, speed segment 6.

The results are to a certain degree expected based upon previous publications - For DPWM, randomization is positive with respect to the sound character and DPWM has a more unpleasant spectrum compared to SPWM. Interestingly, there was almost an opposite trend by increasing the amount of randomization for the SPWM samples. These conclusions gave rise to further questions, as *which factors or metrics contribute to the perceived annoyance?* This is essential to understand and to be able to set objective requirements for ensuring acoustic pleasantness. Previous publications where this topic has been explored for electric motor whining noise are [49, 50, 51].

Thorough examinations of Pearson correlations between established standard metrics as well as psycho-acoustic metrics and the annoyance ratings were conducted. In addition, multiple linear regression analyses including two-way interactions and quadratic terms were performed in order to investigate to what extent annoyance could be modeled by combining the available metrics. The squared correlation coefficient from the multiple regression analyses and the metrics having a correlation coefficient r, $-.5 > r > .5$ is tabulated in Table 8.4. From the statistical explorations, the following conclusions were drawn:

- Different variants of loudness (Zwicker-method according to ISO532B, Stevens mark VII-method), sharpness and the overall sound pressure level (SPL) are very highly correlated. This is rather expected due to the 6 kHz HP-filter applied to the samples.

- Among the available metrics for tonal exposure, tonality is most suitable for quantifying inverter-related tonal components. Prominence ratio (PR) and tone-to-noise ratio (TNR) need to be handled with care since the number of components around the switching frequency and the degree of randomization heavily will impact those

metrics.

- The level-oriented metrics (loudness, SPL and sharpness) have the largest impact on the perceived annoyance and this confirms to some extent the findings by Bassett et al. [49] and Fingerhuth [51]. However, tonality did not contribute substantially in explaining the variance in the data. This concludes that there are one or more dimensions in the nature of the sounds that cannot be captured with established sound quality metrics.

Table 8.4 Squared correlation coefficients from multiple regression and correlation coefficients for the variables having the largest weights in the model

Segment	R^2	Metrics
1	54.7 %	sharpness (r = .70), SPL (.68)
		loudness Zwicker FF (r = .66), roughness (-.53)
2	77.7 %	SPL $(r = .85)$, sharpness (.85), tonality (.54)
		loudness Zwicker FF (.84), roughness (-.68)
3	55.3 %	sharpness (r = .67), tonality (.53), SPL (.51)
4	29.8 %	tonality (r = .53)

Chapter 9

Conclusions and future work

9.1 Conclusions

This thesis focuses on energy efficiency enhancements in an electric vehicle, primarily of the three phase inverter. In addition to the energy efficiency perspective, also the creation of electromagnetic forces and NVH-perspectives are considered. Alternative modulation techniques are investigated, where the so called discontinuous pulse width modulation is proven to decrease the inverter losses, substantially.

The appearance of electromagnetic forces is investigated extensively, with focus on radial forces acting as attractive or repulsive forces between the rotor and the stator. Its influence on stator deformations and consequently noise and vibrations is studied where also influence of machine design, modulation techniques and perceived annoyance of the radiated sound are included. In summary, the main conclusions are presented in the following list.

- In Chapter 3, the formation of electromagnetic forces is presented. Analytical expressions for both temporal and spatial harmonics in both airgap flux density and force density is derived and verified with FE modelling. The harmonic spectra of the current and the vibrations are verified with experimental testing.
- In Chapter 5, FE modelling is covered. A method to perform voltage excited FEM-simulations are presented, instead of FEM-simulations where the phase current is predefined and hence driving the simulation. The method is based on a series of simulation steps where initially a sinusoidal phase current is exciting the machine. In the fourth and final step, an ideal voltage source inverter, operated with PWM is used to drive a voltage excited simulations. The phase current is a consequence

of the machine and the voltage created by the PWM-pattern, rather than an on beforehand defined quantity.

- In Chapter 6, the harmonic content of both the airgap flux density and force density is further investigated. The influence of stator slots on the harmonic spectra is investigated and its influence on the harmonic spectra is quantified. Additionally, it is concluded that minor design changes to the stator slot opening width can decrease the force component causing issues with vibrational order 40 (40 times the rotational speed, caused by excitation of the fifth mode shape). The slot opening width is changed in discrete steps from 1.6 mm to 3.2 mm and a total decrease in roughly -35 percent is seen in Fig. 6.14 in Chapter 6, comparing the largest stator slot opening width with the smallest.

- It is proven that when using discontinuous PWM (DPWM) instead of synchronous PWM (SPWM), the inverter losses can be decreased with up to -17 percent. While complementing the modulation with randomization of the switching frequency the increase in perceived annoyance, due to increased radiated noise for DPWM, is moderate. At rotational speeds above base speed, no difference in perceived annoyance between DPWM and SPWM could be statistically ensured when randomization is used. The decrease in inverter losses is based on numerical simulations, as presented in Chapter 7. Two types of IGBT modules, both suitable for automotive applications, where used and the difference in loss decrease between the two models was less than 2 percentage points.

- Switching frequency randomization is in literature commonly referred to as a prime method to decrease radiated noise and its perceived annoyance of PWM harmonics. The decrease of harmonic tonality by harmonic smearing is commonly presented as the main possibility of noise improvements. In Chapter 8 it is determined that switching frequency randomization does not unanimously improve the situation with acoustic pleasantness, which is contradictory to previous research. It is statistically determined that no improvements in the perceived annoyance can be established for SPWM above base speed. Below base speed it is determined that randomization when using SPWM deteriorates the perceived sensation, which also is a contradiction to previously presented research. However, significant improvements are seen when using randomization on DPWM, especially below base speed. A final observation is that, at a randomization level with a variance of $\sigma = 1000$ Hz the noise is comparable with the magnitude of the harmonics themselves, hence further randomization is without any gain.

9.2 Future work

An interesting continuation would be to further investigate the relations between electromagnetic forces and radiated sound through multi-physical FE modelling. Out of a number of interesting aspects, it is of particular interest to evaluate the accuracy in such simulations in terms of vibrations and radiated noise, as well as study implications of simplifications made to the mechanical design. For instance, structural components that are not influencing the electromagnetic behaviour of the machine might have a significant impact on the structural analysis, such as cooling jacket, mountings and directly attached transmission, speed reducer, etc.

It would also be of interest to study alternative rotor designs. For instance, it is a possiblity that minor geometric modifications to the rotor surface can be used to shape the airgap MMF wave by the change in permeance. If so, it would be interesting to investigate whether minor geometric changes could be beneficial from an NVH perspective, without deterioration of the dynamic performance of the machine. For instance, the airgap permeance could be changed by introducing grooves and thereby step away from a perfectly cylindrical outer profile.

A continuation on the study on how the stator teeth dimensioning affects particulary troublesome noise and vibrations harmonics would be of interest. With a focus on low vibrational orders, thus not on PWM harmonics. The aim would be to, through minor changes to the tips of the stator teeth, decrease the force density harmonics of interest without degrading the over-all performance of the machine. Due to resource limitations, such as time and financial limitations, experimental testing of different designs would be beyond reasonable efforts and hence not possible. However, with a FE model that is verified for one design with the use of experimental testing data, where deviations are quantified, the scientific value of a numerical investigation is assumed to be high and the results trustworthy.

Moreover, it would be of interest to study sensorless operation, where the rotor position sensor is removed and both rotor position and rotational speed is to be estimated instead, although it is outside the scope of this thesis. Sensorless operation is a highly researched area and the objectives of an investigation would be to relate possibilities and challenges with sensorless operation to the ISO standard ISO26262. In relation to the given ISO standard, which is a guideline of how electronics and software are to be developed in order to suppress possibilities of design faults, a number of automotive safety integrity levels (ASIL) classifications arise. Based on occurrence rate, severeness of potential consequences etc. each functionality is marked with a ASIL classification that are to be met in order to completely fulfill the ISO26262 standard. For instance, the electromagnetic torque that is produced by the machine is of high importance to be

estimated correctly due to safety reasons. Without sufficiently accurate rotor position estimation, the torque estimation is to some extent erroneous which is believed to be one significant challenge of sensorless operation in automotive applications. In addition to functionality aspects, also computational load is of importance. The experimental testing equipment, presented in Chapter 4, could very well be used to experimentally verify functionality and theoretical findings.

References

[1] C. W. Jacek F . Gieras and J. C. Lai, *Noise of Polyphase Electric Motors*. CRC Press, 2005.

[2] Y. Xu, Q. Yuan, J. Zou, and Y. Li, "Analysis of triangular periodic carrier frequency modulation on reducing electromagnetic noise of permanent magnet synchronous motor," *IEEE Transactions on Magnetics*, vol. 48, no. 11, pp. 4424–4427, Nov 2012.

[3] J.-Y. Chai, Y.-H. Ho, Y.-C. Chang, and C.-M. Liaw, "On acoustic-noise-reduction control using random switching technique for switch-mode rectifiers in pmsm drive," *IEEE Transactions on Industrial Electronics*, vol. 55, no. 3, pp. 1295–1309, March 2008.

[4] D. Torregrossa, D. Paire, F. Peyraut, B. Fahimi, and A. Miraoui, "Active mitigation of electromagnetic vibration radiated by pmsm in fractional-horsepower drives by optimal choice of the carrier frequency," *IEEE Transactions on Industrial Electronics*, vol. 59, no. 3, pp. 1346–1354, March 2012.

[5] C. Ma and S. Zuo, "Black-box method of identification and diagnosis of abnormal noise sources of permanent magnet synchronous machines for electric vehicles," *IEEE Transactions on Industrial Electronics*, vol. 61, no. 10, pp. 5538–5549, Oct 2014.

[6] M. Sarrazin, J. Anthonis, H. Van der Auweraer, C. Martis, and J. Gyselinck, "Signature analysis of switched reluctance and permanent magnet electric vehicle drives," in *International Conference on Electrical Machines (ICEM)*, Sept 2014, pp. 1831–1837.

[7] Y.-S. Lai, Y.-T. Chang, and B.-Y. Chen, "Novel random-switching pwm technique with constant sampling frequency and constant inductor average current for digitally controlled converter," *IEEE Transactions on Industrial Electronics*, vol. 60, no. 8, pp. 3126–3135, Aug 2013.

[8] Y.-S. Lai and B.-Y. Chen, "New random pwm technique for a full-bridge dc/dc converter with harmonics intensity reduction and considering efficiency," *IEEE Transactions on Power Electronics*, vol. 28, no. 11, pp. 5013–5023, Nov 2013.

[9] J. Prieto, M. Jones, F. Barrero, E. Levi, and S. Toral, "Comparative analysis of discontinuous and continuous pwm techniques in vsi-fed five-phase induction motor," *IEEE Transactions on Industrial Electronics*, vol. 58, no. 12, pp. 5324–5335, Dec 2011.

[10] R. Kirlin, M. Bech, and A. Trzynadlowski, "Analysis of power and power spectral density in pwm inverters with randomized switching frequency," *IEEE Transactions on Industrial Electronics*, vol. 49, no. 2, pp. 486–499, Apr 2002.

[11] N. Boudjerda, A. Boudouda, M. Melit, B. Nekhoul, K. El Khamlichi Drissi, and K. Kerroum, "Optimized dual randomized pwm technique for reducing conducted emi in dc-ac converters," in *EMC Europe*, Sept 2011, pp. 701–706.

[12] A. Walker, M. Galea, C. Gerada, A. Mebarki, and D. Gerada, "A topology selection consideration of electrical machines for traction applications: towards the freedomcar 2020 targets," in *Tenth International Conference on Ecological Vehicles and Renewable Energies (EVER)*, March 2015, pp. 1–10.

[13] G. Pellegrino, A. Vagati, P. Guglielmi, and B. Boazzo, "Performance comparison between surface-mounted and interior pm motor drives for electric vehicle application," *IEEE Transactions on Industrial Electronics*, vol. 59, no. 2, pp. 803–811, Feb 2012.

[14] L. Harnefors, *Control of Variable-Speed Drives*. Department of electronics, Malardalen University, Vasteras, Sweden: Applied signal processing and control, 2002.

[15] J. Hendershot and T. Miller, *Design of Brushless Permanent-Magnet Machines*. Magna Physics Publishing And Oxford University Press, 1994.

[16] M. Cao and N. Hoshi, "Electrical loss minimization strategy for interior permanent magnet synchronous motor drives," in *IEEE Vehicle Power and Propulsion Conference (VPPC)*, Sept 2010, pp. 1–6.

[17] C. Cavallaro, A. Di Tommaso, R. Miceli, A. Raciti, G. Galluzzo, and M. Trapanese, "Efficiency enhancement of permanent-magnet synchronous motor drives by online loss minimization approaches," *IEEE Transactions on Industrial Electronics*, vol. 52, no. 4, pp. 1153–1160, Aug 2005.

[18] O. Josefsson, T. Thiringer, S. Lundmark, and H. Zelaya, "Evaluation and comparison of a two-level and a multilevel inverter for an ev using a modulized battery topology," in *38th Annual Conference on IEEE Industrial Electronics Society (IECON)*, Oct 2012, pp. 2949–2956.

[19] O. Josefsson, "Investigation of a multilevel inverter for electric vehicle applications," Ph.D. dissertation, Technical university of Chalmers, 2015.

[20] S. Brueske, R. Kuehne, and F. W. Fuchs, "Comparison of topologies for the main inverter of an electric vehicle," in *Proceedings of International Exhibition and Conference for Power Electronics, Intelligent Motion, Renewable Energy and Energy Management PCIM*, May 2014, pp. 1–8.

[21] Y. Wu, M. Shafi, A. Knight, and R. McMahon, "Comparison of the effects of continuous and discontinuous pwm schemes on power losses of voltage-sourced inverters for induction motor drives," *IEEE Transactions on Power Electronics*, vol. 26, no. 1, pp. 182–191, Jan 2011.

[22] T. Habetler and D. Divan, "Acoustic noise reduction in sinusoidal pwm drives using a randomly modulated carrier," in *20th Annual IEEE Power Electronics Specialists Conference (PESC)*, Jun 1989, pp. 665–671 vol.2.

[23] K. Cho, S. Yang, H. Kim, and J. Kim, "Improving sound quality of reciprocating compressor using random pwm," in *Eighth International Conference on Power Electronics and Variable Speed Drives. (IEE Conf. Publ. No. 475)*, 2000, pp. 431–436.

[24] I. Tsoumas and H. Tischmacher, "Influence of the inverter's modulation technique on the audible noise of electric motors," *IEEE Transactions on Industry Applications*, vol. 50, no. 1, pp. 269–278, Jan 2014.

[25] S. Capitaneanu, B. d. Fornel, M. Fadel, and F. Jadot, "On the acoustic noise radiated by pwm ac motor drives," *AUTOMATIKA*, vol. 44, no. 3-4, pp. 137–145, 2003.

[26] V. Lanfranchi, G. Friedrich, J. Le Besnerais, and M. Hecquet, "Spread spectrum strategies study for induction motor vibratory and acoustic bahevior," in *32nd Annual Conference on IEEE Industrial Electronics (IECON)*, Nov 2006, pp. 1423–1428.

[27] A. Beig, S. Kanukollu, K. AlHosani, and A. Dekka, "Space vector based synchronized three-level discontinuous pwm for medium voltage high power vsi," *IEEE Transactions on Industrial Electronics*, vol. PP, no. 99, pp. 1–1, 2013.

[28] M. E. Hadj, "Dsp based random discontinuous space vector pwm for variable speed electrical drives," in *15th European Conference on Power Electronics and Applications (EPE)*, 2013, pp. 1–10.

[29] T. Gillespie, *Fundamentals Of Vehicle Dynamics, 1st ed*. Society of Automotive Engineers, Inc., 1992.

[30] K. C. Maliti, *Modelling and Analysis of magnetic noise in squirrel-cage induction motors*. KTH Hogskoletryckeriet, 2000.

[31] B. Sutthiphornsombat, A. Khoobroo, and B. Fahimi, "Mitigation of acoustic noise and vibration in permanent magnet synchronous machines drive using field reconstruction method," *IEEE Vehicle Power and Propulsion Conference (VPPC)*, pp. 1–5, Sept 2010.

[32] S. Zuo, F. Lin, and X. Wu, "Noise analysis, calculation and reduction of external rotor permanent magnet synchronous motor," *IEEE Transactions on Industrial Electronics*, vol. PP, no. 99, pp. 1–1, 2015.

[33] L. Chang, A. Eastham, and G. Dawson, "Permanent magnet synchronous motor: finite element torque calculations," in *Conference Record of the 1989 IEEE Industry Applications Society Annual Meeting*, Oct 1989, pp. 69–73 vol.1.

[34] W. Zhu, B. Fahimi, and S. Pekarek, "Optimal excitation of permanent magnet synchronous machines via direct computation of electromagnetic force components," in *IEEE International Conference on Electric Machines and Drives*, May 2005, pp. 918–925.

[35] M. Islam, R. Islam, and T. Sebastian, "Noise and vibration characteristics of permanent magnet synchronous motors using electromagnetic and structural analyses," in *Energy Conversion Congress and Exposition (ECCE)*, Sept 2011, pp. 3399–3405.

[36] H. Yang and Y. Chen, "Influence of radial force harmonics with low mode number on electromagnetic vibration of pmsm," *IEEE Transactions on Energy Conversion*, vol. 29, no. 1, pp. 38–45, March 2014.

[37] D. Zarko, D. Ban, and T. Lipo, "Analytical calculation of magnetic field distribution in the slotted air gap of a surface permanent-magnet motor using complex relative air-gap permeance," *IEEE Transactions on Magnetics*, vol. 42, no. 7, pp. 1828–1837, July 2006.

[38] H. Yang and Y. Chen, "Influence of radial force harmonics with low mode number on electromagnetic vibration of pmsm," *IEEE Transactions on Energy Conversion*, vol. 29, no. 1, pp. 38–45, March 2014.

[39] U. Krishnamurthy, *Mitigation of Vibration in a Permanent Magnet Synchronous Machine Using Field Reconstruction*. The University of Texas at Arlington, 2008.

[40] J. Wang, Z. Xia, D. Howe, and S. Long, "Vibration characteristics of modular permanent magnet brushless ac machines," in *41st Industry Applications Conference (IAS)*, vol. 3, Oct 2006, pp. 1501–1506.

[41] J.-B. Dupont and P. Bouvet, "Multiphysics modelling to simulate the noise of an automotive electric motor," *SAE International*, June 2012.

[42] T. Rylander, A. Bondeson, and P. Ingelstrom, *Computational Electromagnetics*. Springer, 2013.

[43] "Maxwell online help. release 14.5 - sas ip, inc."

[44] N. Mohan, T. Undeland, and W. Robins, *Power electronics : converters, applications and design*. John Wiley and sons inc., 2003.

[45] J.-Y. Chai, Y.-H. Ho, Y.-C. Chang, and C.-M. Liaw, "On acoustic-noise-reduction control using random switching technique for switch-mode rectifiers in pmsm drive," *IEEE Transactions on Industrial Electronics*, vol. 55, no. 3, pp. 1295–1309, March 2008.

[46] D. Eggers, S. Steentjes, and K. Hameyer, "Advanced iron-loss estimation for nonlinear material behavior," *IEEE Transactions on Magnetics*, vol. 48, no. 11, pp. 3021–3024, Nov 2012.

[47] *Method for the subjective assessment of intermediate quality level of coding systems*, ITU-R BS Recommendation 1534-1, 2003.

[48] M. Lofdahl, A. Nykanen, and R. Johnsson, "Prominence of different directions of hub forces and moments in structure-borne tire noise," *SAE Int. J. Passeng. Cars - Mech. Syst.*, vol. 8, no. 1, pp. 346–353, 2015.

[49] T. Bassett, S. Tate, and M. Maunder, "Study of high frequency noise from electric machines in hybrid and electric vehicles," in *Proc. of InterNoise*, 2014.

[50] D. Lennstrom, T. Lindbom, and Nykanen., "Prominence of tones in electric vehicle interior noise," in *Proc. of InterNoise 2013*, 2013.

[51] S. Fingerhuth, "Tonalness and consonance of technical sounds," Ph.D. dissertation, Rhine-Westphalia Institute of Technology Aachen, 2009.